Public Reporting burden for this collection of information is estimated to average 1 hour per response, including the time for reviewing instructions, searching existing data sources, gathering and maintaining the data needed, and completing and reviewing the collection of information. Send comment regarding this burden estimates or any other aspect of this collection of information, including suggestions for reducing this burden, to Washington Headquarters Services, Directorate for information Operations and Reports, 1215 Jefferson Davis Highway, Suite 1204, Arlington, VA 22202-4302, and to the Office of Management and Budget, Paperwork Reduction Project (0704-0188,) Washington, DC 20503.

1. AGENCY USE ONLY (Leave Blank)	2. REPORT DATE 11/15/00	3. REPORT TYPE AND DATES COVERED FINAL PROGRESS 6/15/95–12/31/98

4. TITLE AND SUBTITLE Zirconia-alumina-ITO nanolaminates for transparent, conducting, transformation-toughening coatings	5. FUNDING NUMBERS DAAH04-95-1-0242

6. AUTHOR(S) Carolyn Rubin Aita

7. PERFORMING ORGANIZATION NAME(S) AND ADDRESS(ES) University of Wisconsin-Milwaukee PO Box 340 Milwaukee, WI 53201	8. PERFORMING ORGANIZATION REPORT NUMBER

9. SPONSORING / MONITORING AGENCY NAME(S) AND ADDRESS(ES) U. S. Army Research Office P.O. Box 12211 Research Triangle Park, NC 27709-2211	10. SPONSORING / MONITORING AGENCY REPORT NUMBER P-34208-MS-AAS

11. SUPPLEMENTARY NOTES
The views, opinions and/or findings contained in this report are those of the author(s) and should not be construed as an official Department of the Army position, policy or decision, unless so designated by other documentation.

12 a. DISTRIBUTION / AVAILABILITY STATEMENT Approved for public release; distribution unlimited.	12 b. DISTRIBUTION CODE

13. ABSTRACT (Maximum 200 words)

The revised objective of the proposed research was investigate room temperature interface alloy and compound formation in zirconia-bearing pseudobinary nanolaminate systems. Two model systems with the same nominal architecture but extremes in chemical reactivity between constituents were compared: zirconia-alumina (immiscible) and zirconia-yttria (completely miscible). The results showed that in zirconia-alumina nanolaminates, layers were separate entity and with incoherent interfaces. The phase present in the zirconia layers was governed by the finite crystal size effect. In zirconia-yttria nanolaminates, an interfacial reaction between constituents completely obliterated separate layers. The reaction product, yttria-stabilized cubic zirconia, grew in the form of needle-like crystallites. These results demonstrate that *coatings consisting entirely of interface reaction products can be fabricated if the bilayer spacing is small enough* in a system in which the bulk equilibrium phase diagram predicts reaction between oxide components. An important question concerns the properties of an interface in a nanolaminate in which there are chemical but not physical driving forces for reaction of bilayer components during deposition, i.e., no predisposition towards heteroepitaxy or pseudomorphism. A model for this behavior is provided by the ZrO_2-TiO_2 system. Study of zirconia-titania nanolaminates was initiated.

14. SUBJECT TERMS sputter deposition, ceramic, nanolaminate, zirconia-alumina, zirconia-yttria, interfacial reaction, finite crytal size, tetragonal zirconia, cubic zirconia, phase transition.	15. NUMBER OF PAGES 64
	16. PRICE CODE

17. SECURITY CLASSIFICATION OR REPORT UNCLASSIFIED	18. SECURITY CLASSIFICATION ON THIS PAGE UNCLASSIFIED	19. SECURITY CLASSIFICATION OF ABSTRACT UNCLASSIFIED	20. LIMITATION OF ABSTRACT UL

NSN 7540-01-280-5500

Standard Form 298 (Rev.2-89)
Prescribed by ANSI Std. 239-18
298-102

20010116 125

DTIC QUALITY INSPECTED 3

ZIRCONIA-ALUMINA-ITO NANOLAMINATES FOR TRANSPARENT, CONDUCTING, TRANSFORMATION-TOUGHENING COATINGS

FOREWORD

The following document is the Final Report of US Army Research Office AASERT Grant No. DAAH04-95-1-0242. The duration of the project was from 6/1/95 to 12/31/98. The AASERT grant was associated with US Army Research Office parent Grant No. DAAH04-93-G-0238, entitled "Nanoscale multilayer zirconia-alumina films for superior fracture toughness," that was active from 10/93 to 6/97. The objective of the parent grant was to develop a family of ceramic coatings with transformation-toughening behavior. The coatings were sputter-deposited zirconia-alumina multilayers with controlled nanoscale microstructures, grown at temperature below 300 °C. The desired structure consisted of bilayer stacks of polycrystalline tetragonal zirconia and amorphous alumina.

The AASERT grant extended and expanded that work to include construction of other laminate materials. The funding provided by the AASERT grant was entirely for student support. Based on results obtained very early in the project, we concluded (in discussion with our monitor, Dr. Robert Reeber) that the original goal of the project should be modified to include investigation of other nanolaminate systems bearing zirconia, not merely to produce a conducting film, but with the idea of interfacial alloy and compound formation at room temperature in mind. For this reason we investigated the zirconia-yttria and zirconia-titania systems. Aided in this investigation was the award of two consecutive instrumentation grants. An AFOSR-DURIP'95 Award supported the purchase of a completely automated reactor. We can now activate the deposition process from any telephone. An ARO-DURIP'96 award supported the upgrade of the reactor to accommodate three targets, enabling the fabrication of nanolaminates with trilayer building blocks.

Carolyn Rubin Aita
Milwaukee, Wisconsin

(1) TABLE OF CONTENTS

(3) LIST OF APPENDICES

A. 'Thermodynamics of tetragonal zirconia formation in a nanolaminate film.' C.R. Aita, M.D. Wiggins, R.Whig, C.M. Scanlan, and M. Gajdardziska-Josifovska, *Journal of Applied Physics* 79, 1176-1178 (1996).

B. 'The transformation structure of zirconia-alumina nanolaminates studied by high resolution electron microscopy.' M. Gajdardziska-Josifovska and C.R. Aita, *Journal of Applied Physics* 79, 1315-1319 (1996).

C. 'Transmission electron microscopy study of zirconia-alumina nanolaminates grown by reactive sputter deposition. Part I: zirconia nanocrystallite growth morphology.' M.A. Schofield, C.R. Aita, P.M. Rice, M. Gajdardziska-Josifovska, *Thin Solid Films* 326 106-116 (1998).

D. 'Transmission electron microscopy study of zirconia-alumina nanolaminates grown by reactive sputter deposition. Part II: transformation behavior of tetragonal zirconia crystallites.' M.A. Schofield, C.R. Aita, P.M. Rice, M. Gajdardziska-Josifovska, *Thin Solid Films* 326 117-125 (1998).

E. 'Reactive sputter deposition of ceramic oxide nanolaminates.' C.R. Aita, *Surface Engineering* 14, 421-426 (1998).

F. 'Thickness-dependent crystallinity of sputter deposited titania.' J.D. DeLoach and C.R. Aita, *Journal of Vacuum Science and Technology A* 16 1963-1968 (1998).

G. PLENARY PAPER: 'Nanostructured ceramic coatings-engineering on an atomic scale.' C.R. Aita, 12th Surface Modification Technologies XII; printed in *Surface Engineering* 15 195-204 (1999).

H. 'Correlation between titania film structure and near ultraviolet optical absorption.' J.D. DeLoach, G. Scarel, and C.R. Aita, *Journal of Applied Physics* 85, 2377-2384 (1999).

I. 'High refractive index <100>-textured cubic zirconia formed in nanolaminates using titania interruption layers.' J.D. DeLoach and C.R. Aita, *Journal of Material Science Letters* 19 1123-1125 (2000).

(4)   STATEMENT OF PROBLEM STUDIED

The revised objective of the proposed research was investigate room temperature interface alloy and compound formation in zirconia-bearing pseudobinary nanolaminate systems. As the thickness of each constituent layer in a nanolaminate decreases, the interface between layers plays an increasingly important role in determining the overall properties of the coating. In turn, chemical reactivity between constituents plays an important role in determining the properties of the interface, even at low growth temperature.

To illustrate this point, we compared two pseudobinary oxide systems that represent extremes in chemical reactivity between constituents: zirconia-alumina and zirconia-yttria. The pseudobinary equilibrium phase diagram of zirconia and alumina shows very limited mutual solid solubility and no compounds [1]. On the other hand, the pseudobinary phase diagram of zirconia and yttria shows a series of solid solutions (alloys) covering the entire composition range from pure zirconia to pure yttria, and compounds are also formed [2-6]. These two model systems allowed comparison of the effects of chemical reactivity between constituents at their interface in nanolaminates with the same nominal architecture.

(5)   SUMMARY OF MOST IMPORTANT RESULTS

The results showed that in zirconia-alumina nanolaminates, each constituent oxide layer was a separate entity and the interface between layers was incoherent. The phase present in the zirconia layers was governed by the finite crystal size effect [7-10]. In zirconia-yttria nanolaminates, an interfacial reaction between constituents completely obliterated yttria as a separate entity. The reaction product, yttria-stabilized cubic zirconia, grew in the form of needle-like crystallites [11]. These results demonstrate the ability to form interfacial oxide solid solutions at low temperature in a system in which the bulk equilibrium phase diagram predicts reaction between oxide components. *Coatings consisting entirely of interface reaction products can therefore be fabricated if the bilayer spacing is small enough.*

An important question concerns the properties of an interface in a ceramic system in which there are chemical but not physical driving forces for reaction of bilayer components during deposition. Furthermore, how would this system behave upon annealing in the absence of the physical constraint of heteroepitaxy holding the bilayer constituents in registry, as in the ZrO_2-Y_2O_3 system?

A model for this behavior is provided by the ZrO_2-TiO_2 system. The bulk pseudobinary ZrO_2-TiO_2 phase diagram is more complex than that for either ZrO_2-Al_2O_3 or ZrO_2-Y_2O_3, and is the subject of continuing investigation [12-14]. Two dissimilar phase diagrams appear in the literature. The differences between these diagrams that are of importance to the present study are a) the prediction of $ZrTiO_4$ versus $ZrTi_2O_6$ as the stable compound below ~1100 °C, and b) the extent in stoichiometry of the $Zr_xY_yO_{2(x+y)}$ (titanate) solid solution. The similarities between these two phase diagrams in comparison to the diagrams for ZrO_2-Y_2O_3 is that neither the titanate phases or any of the unalloyed polymorphs of ZrO_2 or TiO_2 share a common structure. ZrO_2-TiO_2 bilayers are therefore not predisposed to physical interfacial ordering leading to either heteroepitaxy or pseudomorphism. Study of zirconia-titania nanolaminates was initiated.

(6) PUBLICATIONS AND PRESENTATIONS

❑ **Book Chapters And Critical Reviews In Which The Supported Research Appears**

'Tailored ceramic film growth at low temperature by reactive sputter deposition.' C.R. Aita, CRC Critical Reviews in Solid State and Materials Sciences, 23 205-274 (1998).

'Sputter deposition of ceramic oxide and nitride films.' C.R. Aita, in Intermetallic and Ceramic Coatings, (edited by N.B. Dahotre and T.S. Sudarshan, Marcel Dekker, New York, NY, 1999) ch 5. .

❑ **Refereed Publications In Journals/Conference Proceedings**
(Asterisk indicates invited manuscript or manuscript associated with invited paper.)

1. *'Sputter deposited nanostructured ceramic coatings for corrosion wear and resistance." C.R. Aita, in Advances in Coatings Technology for Corrosion and Wear Control Coatings (edited by A.R. Srivatsa, C.R. Clayton, and J.K. Hirovnen, TMS, Warrendale, PA, 1995) pp. 235-254.

2. 'The transformation structure of zirconia-alumina nanolaminates studied by high resolution electron microscopy." M. Gajdardziska-Josifovska and C.R. Aita, J. Appl. Phys. 79, 1315-1319 (1996).

3. 'Thermodynamics of tetragonal zirconia formation in a nanolaminate film.' C.R. Aita, M.D. Wiggins, R.Whig, C.M. Scanlan, and M. Gajdardziska-Josifovska, J. Appl. Phys. 79, 1176-1178 (1996).

4. *'Zirconia-alumina transformation-toughening nanolaminate coatings.' C.R. Aita, M. Gajdardziska-Josifovska, and M.D. Wiggins, in Processing and Fabrication of Advanced Materials IV (edited by T.S. Srivatsan and J.J. Moore, TMS, Warrendale, PA, 1996) pp. 237-249.

5. 'High resolution electron microscopy of sputter-deposited zirconia-alumina nanolamiantes.' M.A. Schofield, R. Whig, C.R. Aita, and M. Gajdardziska-Josifovska, Proc. Mater. Res. Soc. 403, 297-301 (1996) .

6. 'Nanostructured ceramic coatings: Zirconia single layers and nanolaminates.' C.R. Aita in Processing and Fabrication of Advanced Materials V (edited by T.S. Srivatsan and J.J. Moore, TMS, Warrendale, PA, 1997) pp. 459-468.

7. 'Transmission electron microscopy study of zirconia-alumina nanolaminates grown by reactive sputter deposition I: Zirconia nanocrystallite growth morphology.' M.

Schofield, C.R. Aita, P.M. Rice, and M. Gajdardziska-Josifovska, Thin Solid Films 326, 106-116 (1998).

8.   'Transmission electron microscopy study of zirconia-alumina nanolaminates grown by reactive sputter deposition II: Transformation behavior of tetragonal zirconia nanocrystallites.' M. Schofield, C.R. Aita, P.M. Rice, and M. Gajdardziska-Josifovska, Thin Solid Films, 326, 117-125 (1998).

9.   *'Reactive sputter deposition of ceramic oxide nanolaminates: zirconia-alumina and zirconia-yttria model systems.' C.R. Aita, Surface Engineering 14 421-426 (1998).

also printed in: Surface Modification Technologies XI (edited by T.S. Sudarshan, M. Jeandin, and K.A. Khor, TMS, Warrendale PA, 1998) 468-479.

10.   *'*In situ* sputter deposition discharge diagnostics for tailoring ceramic film growth.' C.R. Aita, J. Vac. Sci. Technol. A 16, 1303-1310 (1998).

11.   *Plenary paper: 'Nanostructured ceramic coatings-engineering on an atomic scale.' C.R. Aita, 12th Surface Modification Technologies XII printed in Surface Engineering 15 204-195 (1999).

Extended Abstracts
1.   'Electron-beam induced transformations in zirconia alumina nanolaminates: an *in situ* high resolution electron microscopy study.' M.A. Schofield, M. Gajdardziska-Josifovska, R. Whig, and C.R. Aita, Proc. 54nd Ann. Mtg. Mircoscopy Society of America (edited by G.W. Bailey, J.M. Corbett, R.V. W. Dimlich, J.R. Michael, and N.J. Zaluzec (San Francisco Press, San Francisco, CA, 1996) pp. 690-691.

❏   **Invited And Contributed Papers At National/International Symposia**   [Presenting author underlined]

Invited Papers

1.   'Nanostructured ceramic and multilayer nanolaminate coatings for corrosion and wear resistance. C.R. Aita The Minerals, Metals, & Materials Society (TMS) Annual Meeting, Las Vegas, NV, 1995.
2.   'Transformation-toughening ceramic nanolaminate coatings.' C.R. Aita The Minerals, Metals, & Materials Society (TMS) Fall Meeting, Cleveland, OH, 1995.
3.   'Reactive physical vapor deposition processes.' C.R. Aita, International Materials Research Congress, Cancun, Mexico, 1996.
4.   'Nanostructured ceramic coatings' C.R. Aita The Minerals, Metals, & Materials Society (TMS) Fall Meeting, Cincinnati, OH, 1996.

5. 'Reactive sputter deposition of ceramic oxide nanolaminates: zirconia-alumina and zirconia-yttria model systems.' C.R. Aita, 11th International Conference on Surface Modification Technologies, Paris, France, 1997.

6. '*In situ* sputter deposition plasma characterization for tailoring ceramic film growth.' C.R. Aita, American Vacuum Society 44th National Symposium, San Jose, CA, 1997.

7. PLENARY TALK: 'Nanostructured ceramic coatings-engineering on an atomic scale.' C.R. Aita, 12th International Conference on Surface Modification Technologies, Rosemont, IL, 1998.

Contributed Papers

1. 'Martensitic transformation in zirconia-alumina nanolaminates.' M. Gajdardziska-Josifovska and C.R. Aita, 53nd Ann. Mtg. Microscopy Society of America, New Orleans, LA, 1995.

2. 'Phase development in sputter deposited titania.' M.D. Wiggins, M.C. Nelson, C.R. Aita, American Vacuum Society 42st National Symposium, Minneapolis, MN, 1995.

3. 'Crystallization kinetics of amorphous titania thin films.' M.D. Wiggins, M.C. Nelson, and C.R. Aita, Materials Research Society Fall Meeting, Boston, MA, 1995.

4. 'Transformation structure of zirconia-alumina nanolaminates studied by HREM.' M.A. Schofield, R. Whig, C.R. Aita, and M. Gajdardziska-Josifovska, Materials Research Society Fall Meeting, Boston, MA, 1995.

5. 'Zirconia-based transformation-toughening ceramic nanolaminate coatings.' C.R. Aita, M.D. Wiggins, R. Whig, M.A. Schofield, J. DeLoach, J. Kostuch and M. Gajdardziska-Josifovska, Materials Research Society Spring Meeting, San Fransisco, CA, 1996.

6. 'Electron-beam induced transformations in zirconia alumina nanolaminates: an *in situ* high resolution electron microscopy study.' M.A. Schofield, M. Gajdardziska-Josifovska, R. Whig, and C.R. Aita, Proc. 54nd Ann. Mtg. Mircoscopy Society of America, Minneapolis, MN, 1996.

7. 'High resolution transmission electron microscopy of electron beam induced transformations in zirconia-alumina nanolaminates.' M.A. Schofield, M. Gajdardziska-Josifovska, and C.R. Aita, American Vacuum Society 43rd National Symposium, Philadelpha, PA, 1996.

8. 'Thickness-dependent crystallinity of sputter deposited titania.' J.D. DeLoach and C.R. Aita, American Vacuum Society 44th National Symposium, San Jose, CA, 1997.

9. 'Transmission electron microscopy of the transformation behavior of tetragonal zirconia crystallites in zirconia-alumina nanolaminates.' M.A. Schofield, M. Gajdardziska-Josifovska, C.R. Aita, and P.M. Rice, Materials Research Society Fall Meeting, Boston, MA, 1997.

10. High refractive idex <100> textured cubic zirconia formed in nanolaminate coatings using titania interruption layers.' J.D. DeLoach and C.R. Aita, American Vacuum Society 46th National Symposium, Seattle, CA, 1999.

11. 'Correlation between phase constituency and near ultraviolet optical absorption in nanophase titania films.' J.D. DeLoach, G. Scarel, and C.R. Aita, American Vacuum

Society 46th National Symposium, Seattle, CA, 1999.

(7) PARTICIPATING SCIENTIFIC PERSONNEL

Student Graduated/Degree/Thesis Title:
PhD: Juanita DeLoach, PhD, EE, May 1998 (currently employed in Texas Instruments, Dallas, TX).
MS:
1. Renu Whig, MS-5/96, (currently employed in Motorola, Scottsdale, AZ).
2. Brian Blackmon, MS-5/97. (currently employed by Motorola, Scottsdale, AZ.)

Current Students Supported In Part By Project:
1. Giovanna Scarel, PhD, Materials, expected graduate date: May 2001.

(8) REPORT OF INVENTION

Patent issued: 'Multilayer nanolaminates containing polycrystalline zirconia.' C.R. Aita, US Patent No. 5472795, 12/5/95 (under parent grant).

(9) BIBLIOGRAPHY

1. D.F. Green, R.H.J. Hannink, and M.V. Swain, *Transformation Toughening Of Ceramics* (CRC Press, Boca Raton, 1989) pp. 1-15.
2. R. Ruh, R., K.S. Mazdiyasni, P.G. Valentine, and H.O. Bielstein, Phase Relations In The System ZrO_2-Y_2O_3 At Low Y_2O_3 Content, J. Amer. Ceram. Soc. **67**, C190-C192 (1984).
3. M.H. Tuilier, J. Dexpert-Ghys, H. Dexpert, and P. Lagarde, 'X-Ray Absorption Study Of The ZrO_2-Y_2O_3 System,' Journal of Solid State Chemistry **69**, C153-C161 (1987).
4. C. Pascaul, C. and P. Duran, 'Subsolidus Phase Equilibria And Ordering In The System ZrO_2-Y_2O_3,' Journal of the American Ceramic Society **66**, 23-27 (1982).
5. H.G. Scott, 'Phase Relationships In The Yttria-Rich Part Of The Yttria-Zirconia System,' Journal of Materials Science **12**, 311-316 (1977).
6. H.G. Scott, 'The Yttria-Zirconia δ Phase,' Acta Crystallographica **B33**, 281-282 (1977). C.R. Aita, 'Multilayer Nanolaminates Containing Polycrystalline Zirconia,' US Patent No. 5472795, 12/5/95.
7. C.M. Scanlan, M.Gajdardziska-Josifovska, and C.R. Aita, 'Tetragonal Zirconia Growth By Nanolaminate Formation,' Applied Physics Letters, **64**, 3548-3550 (1994).
8. C.R. Aita, M.D. Wiggins, R.Whig, C.M. Scanlan, and M. Gajdardziska-Josifovska, 'Thermodynamics Of Tetragonal Zirconia Formation In A Nanolaminate Film,' Journal of Applied Physics **79**, 1176-1178 (1996).
9. M. Gajdardziska-Josifovska and C.R. Aita, 'The Transformation Structure Of Zirconia-Alumina Nanolaminates Studied By High Resolution Electron Microscopy,' Journal of Applied Physics **79**, 1315-1319 (1996).

10. M. Schofield, C.R. Aita, P.M. Rice, and M. Gajdardziska-Josifovska, 'Transmission Electron Microscopy Study Of Zirconia-Alumina Nanolaminates Grown By Reactive Sputter Deposition I: Zirconia Nanocrystallite Growth Morphology,' Thin Solid Films **326**, 106-116 (1998).

11. C.R. Aita, 'Reactive Sputter Deposition Of Ceramic Oxide Nanolaminates: Zirconia-Alumina And Zirconia-Yttria Model Systems,' Surface Engineering **14**, 421-426 (1998).

12. R.W. Lynch and B. Morosin, 'Thermal Expansion, Compressibiliby, And Polymorphism In Hafnium And Zirconium Titanates,' Journal of the American Ceramics Society **55**, 409-413 (1972).

13. A.E. McHale and R.S. Roth, 'Low-Temperature Phase Relationships In The System ZrO_2-TiO_2,' Journal of the American Ceramics Society **69**, 827-832 (1986).

14. E.M. Levin and H.F. McMurdie Phase Diagrams For Ceramists Volume III (American Ceramic Society, Westerville, OH, 1975) p. 16.

Thermodynamics of tetragonal zirconia formation in a nanolaminate film

C. R. Aita,[a] M. D. Wiggins, R. Whig, and C. M. Scanlan[b]
Materials Department and The Laboratory for Surface Studies, University of Wisconsin-Milwaukee, P. O. Box 784, Milwaukee, Wisconsin 53201

M. Gajdardziska-Josifovska
Department of Physics and The Laboratory for Surface Studies, University of Wisconsin-Milwaukee, P. O. Box 413, Milwaukee, Wisconsin 53201

Zirconia–alumina transformation-toughening nanolaminates were fabricated by reactive sputter deposition. The average crystallite size and volume fraction of each zirconia polymorph were determined by x-ray diffraction. The volume fraction of tetragonal zirconia, the phase necessary for transformation toughening, was found to strongly depend upon the zirconia layer thickness. An end-point thermodynamics model involving hemispherical cap zirconia crystallites was developed to explain this phenomenon. In excellent agreement with experimental results, the model predicts that unity volume fraction of tetragonal zirconia is produced in the nanolaminate when the zirconia layer thickness is less than the radius at which a growing zirconia crystallite spontaneously transforms to the monoclinic phase. © *1996 American Institute of Physics.* [S0021-8979(96)00102-7]

The protective behavior of bulk zirconia-based transformation-toughening ceramics depends upon the presence of tetragonal zirconia, a high-temperature polymorph "retained" at room temperature. Retention of tetragonal zirconia is commonly achieved by reducing the crystallite size and adding a stabilizing dopant, such as yttria or ceria.[1] In response to a stress concentrator, these tetragonal zirconia crystallites transform locally to monoclinic zirconia (the STP equilibrium phase) via a martensitic transition involving an anisotropic lattice expansion.[2] A defect structure that toughens the material develops in both the daughter phase and at the parent/daughter interface at the site of the stress concentrator. For example, the material transformation toughens in the vicinity of a crack tip, which prevents the crack from spreading.

We recently applied zirconia transformation-toughening technology to thin films. A nanolaminate structure consisting of alternating layers of polycrystalline zirconia and amorphous alumina was fabricated.[3] The alumina layers served as growth termination and restart surfaces for the zirconia crystallites. A large volume fraction of tetragonal zirconia was produced in this structure,[4] independent of the kinetic parameters that control tetragonal zirconia growth in thick, single-layer zirconia films,[5] and without the addition of a stabilizing dopant. Since the zirconia crystallite dimension perpendicular to the substrate was limited by the individual layer thickness, the finite size effect was assumed to be involved in some manner in tetragonal zirconia stabilization. However, the question remains: Can a quantitative model be developed that relates the nanolaminate structure to tetragonal zirconia formation?

In this communication we demonstrate that unity volume fraction tetragonal zirconia is produced when the thickness of each zirconia layer is less than the radius at which an unconstrained, unstressed hemispherical tetragonal zirconia crystallite spontaneously transforms to monoclinic at the growth temperature.[2] As we show, this model can be used to predict the layer thickness at which unity volume fraction tetragonal zirconia is produced in any zirconia-based nanolaminate, independent of the material of the restart layer provided its interface with the growing zirconia crystallites is incoherent.

Nanolaminate growth and analysis: Nanolaminates were grown by reactive sputter deposition in a multiple-target rf diode system.[4] The substrates, fused Suprasil silica flats, were placed on a rotary table and moved sequentially under Zr and Al targets. The targets were sputtered using 10^{-2} Torr O_2 discharges operated at -1.4 kV (p-p) for Zr and -1.1 kV (p-p) for Al. The growth temperature was 290 °C. The zirconia layer growth rate was 1.5 nm/min and the alumina layer growth rate was 0.5 nm/min. The zirconia layer thickness ranged from 4.5 to 60 nm. The alumina layer thickness was 4 nm. The total nanolaminate thickness ranged from 100 to 200 nm. The number of bilayers ranged from 3 to 17. The zirconia layer phase composition was previously found to be independent of both the number of zirconia layers and the total film thickness for the range of these parameters used here.[6]

Films were analyzed by double-angle x-ray diffraction (XRD) using unresolved Cu $K\alpha$ x radiation ($\lambda=0.1542$ nm). Diffraction peak position, maximum intensity, and full width at half of the maximum intensity were measured. The average crystallite dimension perpendicular to the substrate plane $\langle r \rangle$ was calculated using the Scherrer relation.[7] The volume fraction of each zirconia phase was calculated from the integrated intensities using the polymorph method.[8] These data are tabulated, in part, in Refs. 4 and 6.

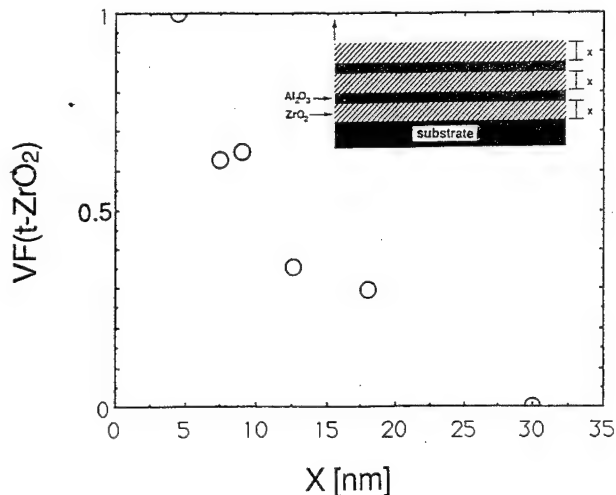Zirconia layer phase constitution: X-ray diffraction

---

FIG. 1. The volume fraction of tetragonal zirconia as a function of zirconia layer thickness X in zirconia–alumina nanolaminates grown on fused silica substrates.

showed that the phase constitution of the zirconia layers was either tetragonal (t), monoclinic (m), or a mixture of $t+m$ depending upon the zirconia layer thickness X. The tetragonal zirconia volume fraction decreased with increasing X, as shown in Fig. 1. Nanolaminates with thick zirconia layers ($X \geqslant 30$ nm) were entirely monoclinic.

The average monoclinic $\langle r(m) \rangle$ and tetragonal $\langle r(t) \rangle$ crystallite dimensions perpendicular to the substrate are shown as a function of zirconia layer thickness in Fig. 2. Monoclinic and tetragonal crystallites have different $\langle r \rangle$ vs X behavior. Specifically, $\langle r(m) \rangle$ increases over the entire range of X. At $X \geqslant 30$ nm, the value of $\langle r(m) \rangle$ is identical to that for thick (50–200 nm), single-layer monoclinic zirconia
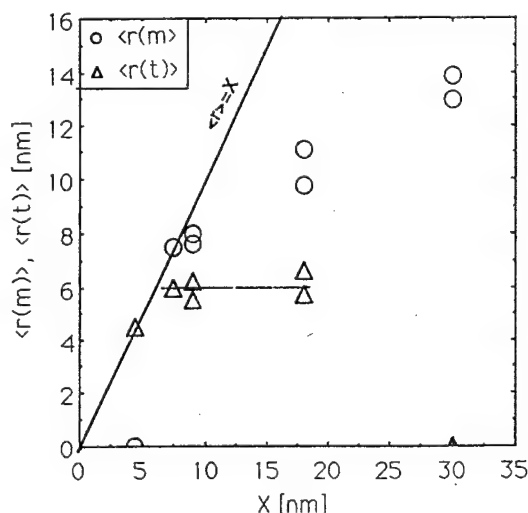

FIG. 2. The average monoclinic $\langle r(m) \rangle$ and tetragonal $\langle r(t) \rangle$ crystallite dimension perpendicular to the substrate as a function of zirconia layer thickness X. The saturation value of $\langle r(t) \rangle = 6.0 \pm 0.2$ nm (shown as a dotted line) is within experimental error of the critical radius for a spontaneous tetragonal-to-monoclinic zirconia phase transformation calculated from Eq. (1): $r_c = 6.2$ nm.
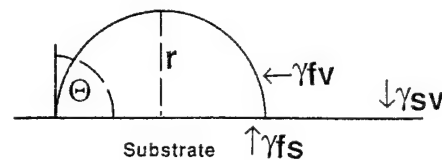

FIG. 3. The surface energy terms relevant to a hemispherical cap nucleus of radius r on a substrate. γ_{fv} is the surface energy of the film–vapor interface, γ_{fs} is the surface energy of the film–substrate interface, and γ_{sv} is the surface energy at the substrate–vapor interface. The contact angle Θ between the substrate and the cap is equal to $\pi/2$.

films grown under the same deposition conditions as the zirconia layers in the nanolaminates.[5] In contrast to the behavior of $\langle r(m) \rangle$, $\langle r(t) \rangle$ does not increase above 6.0 ± 0.2 nm even though X increases.

End-point thermodynamics calculation for tetragonal zirconia stabilization: To understand the $\langle r(t) \rangle$ vs X behavior seen in Fig. 2, consider the thermodynamics of the finite size effect. Tetragonal crystallites will spontaneously transform to monoclinic as they grow above a critical size at a given growth temperature. In the following analysis, the shape of the zirconia nanocrystallites is assumed to be approximately hemispherical both before and after the transformation. This assumption is supported by high-resolution transmission electron microscopy (HREM) data from a nanolaminate with nominal zirconia layer thickness equal to 4.5 nm.[9] These data show that the average crystallite size perpendicular to the substrate (i.e., in the film growth direction) is equal to 4.8 ± 0.8 nm, in close agreement with the nominal layer thickness and the XRD-measured value. The average crystallite size in the plane of the nanolaminate is equal to 9.9 ± 2.3 nm. These nanocrystallite dimensions indicate a radius-to-one diameter ratio of 1:2, consistent with a hemispherical cap shape.

The Gibbs free energy G of a hemispherical cap crystallite on a substrate is given by

$$G = (2\pi/3)r^3 g + 2\pi r^2 (\gamma_{fv} + \gamma_{fs} - \gamma_{sv}),$$

where g is the volume free energy associated with a particular phase. With reference to Fig. 3, γ_{fv} is the surface energy of the film–vapor interface and γ_{fs} is the surface energy of the film–substrate interface. γ_{sv} is the surface energy at the substrate–vapor interface and must be included in the energy balance as a deficit because substrate–vapor interfacial area is covered by the base of the crystallite. The surface energy terms are related through the contact angle Θ where $\cos \Theta = (\gamma_{sv} - \gamma_{fs})/\gamma_{fv}$. For a hemisphere, $\Theta = \pi/2$, therefore $\gamma_{sv} = \gamma_{fs}$. Consequently, the Gibbs free energy accompanying the tetragonal-to-monoclinic zirconia growth transformation is given by $\Delta G = (2\pi/3)r^3 \Delta g + 2\pi r^2 \Delta \gamma_{fv}$. At $\Delta G = 0$, the critical radius for a spontaneous tetragonal-to-monoclinic zirconia growth transformation is $r_c = -3\Delta \gamma_{fv}/\Delta g$.

Values for the energy terms are as follows:

$$\Delta g = -2.85 \times 10^9 [1 - (T/1448 \text{ K})] \text{ erg/cm}^3,$$

where T is the growth temperature,[2] and[10]

J. Appl. Phys., Vol. 79, No. 2, 15 January 1996

Aita *et al.* 1177

$$\Delta\gamma_{fv} = [\gamma_{fv}(m) - \gamma_{fv}(t)] = (1130 - 770) \ erg/cm^2$$

$$= 360 \ erg/cm^2.$$

The expression for the critical radius becomes

$$r_c = 3.79[1 - (T/1448 \ K)]^{-1} \ nm. \tag{1}$$

At the growth temperature used here, $r_c = 6.2$ nm. This result is in excellent agreement with the experimentally observed maximum value of $\langle r(t)\rangle \doteq 6.0\pm0.2$ nm obtained from Fig. 2.

In summary, it was found that an end-point thermodynamics analysis can be used to model the critical radius at which a tetragonal-to-monoclinic zirconia growth transformation occurs. This model is technologically important because it enables prediction of the maximum zirconia layer thickness yielding unity volume fraction tetragonal zirconia at a given film growth temperature. In addition, it can be seen from Eq. (1) that the critical radius size is very weakly dependent on growth temperature in the range commonly used for sputter deposition (<300 °C). Therefore, the only practical design parameter for zirconia-based transformation-toughening nanolaminates is the zirconia layer thickness.

[1] D. J. Green, R. H. J. Hannink, and M. V. Swain, *Transformation Toughening of Ceramics* (CRC, Boca Raton, FL, 1989).

[2] R. C. Garvie and M. V. Swain, J. Mater. Sci. **20**, 1193 (1985).

[3] C. R. Aita, Patent No. 5472795.

[4] C. M. Scanlan, M. Gajdardziska-Josifovska, and C. R. Aita, Appl. Phys. Lett. **64**, 3548 (1994).

[5] C. R. Aita, Nanostructured Mater. **4**, 257 (1994).

[6] C. M. Scanlan, M. D. Wiggins, M. Gajdardziska-Josifovska, and C. R. Aita, Proc. Mater. Res. Soc. **343**, 481 (1994).

[7] L. V. Azaroff, *Elements of X-ray Crystallography* (McGraw–Hill, New York, 1968), pp. 551–552.

[8] R. C. Garvie and P. S. Nicholson, J. Am. Ceram. Soc. **55**, 303 (1972).

[9] M. Gajdardziska-Josifovska and C. R. Aita, J. Appl. Phys. (in press).

[10] R. C. Garvie, J. Phys. Chem. **69**, 1239 (1965).

The transformation structure of zirconia-alumina nanolaminates studied by high resolution electron microscopy

M. Gajdardziska-Josifovska[a)] and C. R. Aita[b)]

The Laboratory for Surface Studies, University of Wisconsin-Milwaukee, Milwaukee, Wisconsin 53201

Quantitative high resolution electron microscopy (HREM) was employed to study the crystallography of a zirconia-alumina transformation-toughening nanolaminate. The nanolaminate consisted of alternating layers of polycrystalline zirconia and amorphous alumina. The zirconia layer thickness was scaled to insure unity volume fraction of the metastable tetragonal phase at the growth temperature, as predicted by an end-point thermodynamics model and verified by x-ray diffraction. In the microscopy sample, phase identification was achieved from precise measurements of lattice spacings using digital diffractograms of individual nanocrystallites. Of the nanocrystallites analyzed, $(22\pm6)\%$ were monoclinic in a distinct crystallographic relationship with their tetragonal neighbors. The following plane and direction relationships were identified: $m(100)//t(100)$ and $m[001]//t[001]$. The observed structure is the result of a stress-induced transformation from the tetragonal phase. This transformation was localized to nanosized regions within the individual zirconia layers. © *1996 American Institute of Physics.* [S0021-8979(96)08102-2]

I. INTRODUCTION

With an eye toward developing transformation-toughening ceramic coatings, we grew multilayers of polycrystalline zirconia and amorphous alumina in which the layer spacing was scaled to ensure nanosize zirconia crystallites.[1,2] In this manner, nanolaminates with a high volume fraction of tetragonal zirconia (t-ZrO_2) were produced without the use of dopants.

For a coating to be of practical use, not only must it contain a significant amount of t-ZrO_2, but this phase must also transform *locally* to the monoclinic phase (m-ZrO_2) in response to stress. In bulk zirconia-alumina composites, with dopant stabilized tetragonal zirconia, the martensitic $t\rightarrow m$ transition can be auto catalytic, resulting in widespread transformation of the parent phase.[3]

In this article, the $t\rightarrow m$-ZrO_2 transformation in a nanolaminate with very fine zirconia layer spacing is studied using quantitative high resolution electron microscopy (HREM). We demonstrate that the transformation is limited to within individual zirconia layers, and furthermore, it is localized in a nanosized region adjacent to the parent crystallite. We also identify the crystallographic correspondence between the parent and daughter phases.

II. EXPERIMENT

A. Nanolaminate growth

The nanolaminates were grown by reactive sputter deposition in a multiple target rf diode system, as described in detail in Ref. 1. To briefly summarize, Si(111) wafers, from which the nascent oxide was not removed, were used as substrates for the multilayers studied by microscopy. Along with other substrates, Si was placed on a rotary table and moved sequentially under Zr and Al targets. The targets were sputtered using 10^{-2} Torr O_2 discharges operated at -1.4 kV $(p-p)$ for Zr and -1.1 kV $(p-p)$ for Al. The growth temperature was 564 ± 10 K. The zirconia layer growth rate was 1.5 nm/min and the alumina layer growth rate was 0.5 nm/min. The nanolaminate consisted of 50 zirconia-alumina bilayers. The nominal thickness of each zirconia layer was 4.5 nm, and each alumina layer thickness was 3.7 nm. The total nanolaminate thickness was 0.4 μm.

To insure the growth of t-ZrO_2 rather than m-ZrO_2, we used the following reasoning to choose the zirconia layer thickness. Previous results[4] for single-layer zirconia films showed that an expanding hemispherical cap was a good model for individual crystallite growth. Assuming this model for zirconia crystallite growth in the nanolaminates, we used end-point thermodynamics[5] to determine the critical cap radius (r_c) below which t-ZrO_2, not m-ZrO_2, was the low energy phase at the growth temperature, 564 K.[6] We calculated $r_c=6.2$ nm, and chose the zirconia layer thickness to be less than this value. The phenomenon of a phase transformation at a critical surface/volume ratio is a manifestation of the finite size effect, and its analogy is widely reported in bulk zirconia ceramics.[3]

B. Nanolaminate characterization

HREM studies were performed with a 400 keV JEM 4000EX transmission electron microscope with a point-to-point resolution of 0.17 nm. The nanolaminates were viewed in cross-section, using a specimen prepared by mechanical dimpling and polishing, followed by 5 keV Ar^+ ion-milling at room temperature. The HREM images, captured on photographic plates, were digitized with an optical close coupled diffraction (CCD) camera. Numerical diffractograms (i.e., two dimensional Fourier transforms) were calculated to study the crystallography of individual nanocrystallites. Lattice spacings of zirconia were measured applying the novel

[a)]Department of Physics, University of Wisconsin-Milwaukee, P.O. Box 413, Milwaukee, WI 53201; Electronic mail: mgj@alpha2.csd.uwm.edu
[b)]Materials Department and Department of Electrical Engineering and Computer Science, University of Wisconsin-Milwaukee, P. O. Box 784, Milwaukee, WI 53201.
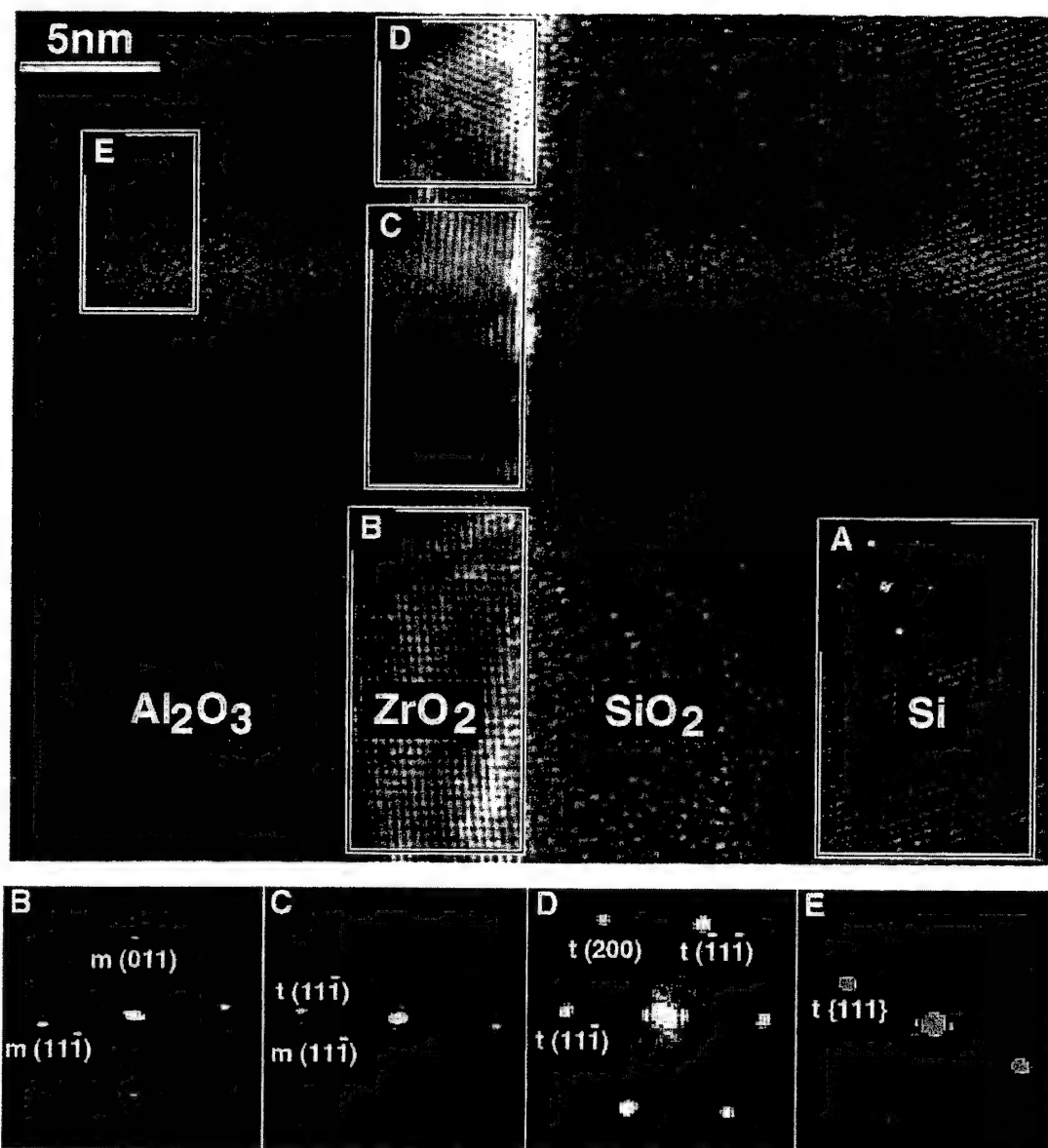
FIG. 1. Digitized high resolution electron micrograph of zirconia-alumina multilayer with numerical diffractograms used for accurate lattice spacing measurements. Boxes denote analyzed regions.

digital method due to de Ruijter *et al.*[7-9] The analysis was carried within the Digital Micrograph image acquisition and processing software platform by Gatan. The relative orientations of the nanocrystallites were obtained by measuring angles in the numerical diffractograms. The nanocrystallites sizes were measured from the digitized micrographs using an NIH image.

The digital lattice-fringe quantification method[7-9] is the key to obtaining zirconia phase-separated data. This method is particularly powerful for analysis of nanocrystallites because:

(a) it allows formation of diffractograms from nanocrystallites of arbitrary size;

(b) it removes diffraction effects due to image edges by applying a soft Hanning window; and

(c) it uses bi-linear interpolation in reciprocal space to find

the center of the broad diffraction spots typical for nanocrystallites.

Using this technique, the lattice spacings of the nanocrystallites studied here can be obtained to an accuracy better than ~0.5%.[9]

III. RESULTS AND DISCUSSION

Figure 1 shows a high resolution image of the first two zirconia layers adjacent to the Si substrate. The native silicon oxide layer and the deposited alumina layer show speckled random contrast typical for amorphous materials. Four distinct crystallites are visible in the zirconia layers. They are enclosed in rectangles *B-E* which mark the image areas that were Fourier transformed to obtain the corresponding diffractograms given at the bottom of Fig. 1. The Si{111} lattice

M. Gajdardziska-Josifovska and C. R. Aita

TABLE I. Indexing of the zirconia diffractograms shown in Figs. 1 and 2.

Area	d_{hkl} of film [nm]	Phase	d_{hkl} of bulk standard [nm][a]
B	0.318	$m(11\text{-}1)$	0.316
	0.369	$m(011)$	0.369
C	0.300	$m(11\text{-}1)$[b]	0.316
	0.296	$t(11\text{-}1)$	0.296
D	0.297	$t(11\text{-}1)$	0.296
	0.290	$t(-1,1,-1)$[b]	0.296
	0.253	$t(200)$	0.254
E	0.294	$t\{111\}$	0.296
F	0.310	$m(11\text{-}1)$[b]	0.316
	0.296	$t(11\text{-}1)$	0.296
	0.295	$t(-11\text{-}1)$	0.296
	0.254	$t,m(200)$	0.254

[a]See Ref. 10.
[b]Spacings in nanocrystallites which are smaller than the bulk standard by a value exceeding the experimental error.

fringes from area A were used for calibration. Data obtained from analysis of the diffractograms with reference to bulk standards[10] is recorded in Table I. The Miller indices of the crystal planes are also denoted on the diffractograms in Fig. 1. The same analysis was carried on ten other image regions, containing approximately 50 zirconia particles. Statistical analysis of the measured lattice spacings yielded a volume fraction of $72\pm6\%$ of t-ZrO_2 with the remainder identified as m-ZrO_2.[11]

X-ray diffraction (XRD) of the identical multilayer structure grown on a variety of substrate materials including Si, fused silica, Al, kapton, and laboratory glass slides shows no detectable first or higher order diffraction from the monoclinic phase. This experimental evidence, coupled with the aforementioned theoretical model, leads us to conclude that the monoclinic crystallites observed in the HREM study are produced by stress transformation during sample preparation.

Therefore, the structure observed by HREM simulates the structure of a functional nanolaminate that has undergone a stress-induced transformation-toughening.

In this work we have investigated each of the monoclinic crystallites to find them invariably adjacent to tetragonal crystallites in a definite orientation relationship. In contrast, many of the tetragonal crystallites were surrounded by tetragonal crystallites in random orientation. These observations provide clear supporting evidence for transformation as origin of the monoclinic nanocrystallites. For this reason, the figures shown in this work are not chosen as representative of the nanolaminate in general, but rather as representative of the transformation nanostructure.

The combined results from Table I and Fig. 1 show that area D is tetragonal with $t\{111\}$ planes oriented parallel to the substrate surface. This crystallite is representative of the parent phase in the nanolaminate. Area C is biphasic; the upper portion is tetragonal and the lower portion is monoclinic. $t(11\text{-}1)$ planes are oriented parallel to the substrate, while $m(11\text{-}1)$ planes are tilted at a ~9° angle with respect to the substrate surface. The relationship between $t(11\text{-}1)$ and $m(11\text{-}1)$ planes in area C is typical of adjacent parent/daughter regions throughout the nanolaminate. It shows clearly that the $t\rightarrow m$-ZrO_2 transformation involves an out-of-plane rotation of $t(11\text{-}1)$ by ~9° to form $m(11\text{-}1)$. Area B is a crystallite that has completely transformed to m-ZrO_2. It shows the tell-tale tilt of $m(11\text{-}1)$ with respect to the substrate plane, and hence to $t(11\text{-}1)$ of the parent crystallite from which it originated. This parent t-ZrO_2 crystallite is at the lower border of area B and is not included in Fig. 1. The upper border of area D is given in Fig. 2.

Figure 2(a) shows a biphasic area in the first zirconia layer. The corresponding numerical diffractogram is shown in Fig. 2(b). The lattice spacings obtained from this diffractogram indicate that the top part of the area is tetragonal while the bottom part is monoclinic. The (200) lattice fringes remain invariant in spacing and angle in both tetragonal and monoclinic regions of Fig. 2. The zone axis for each region,
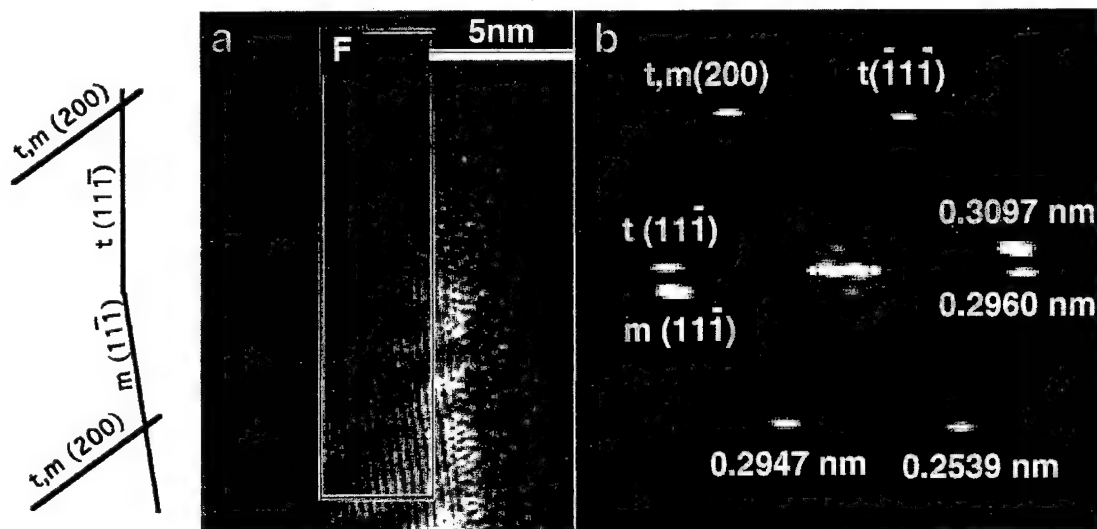

FIG. 2. (a) Digitized HREM image of a biphasic zirconia region with line drawing depicting the crystallographic orientation relationship between the parent tetragonal and daughter monoclinic phase. (b) Numerical diffractogram with indexed crystal planes and measured lattice spacings.
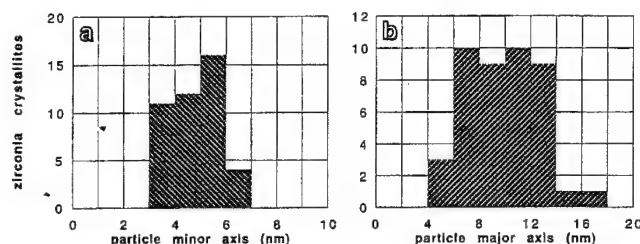
FIG. 3. Histograms showing zirconia crystallite dimensions measured from HREM images. The minor axis (a) is along the growth direction and the major axis (b) is along the growth interface.

calculated from the lines of intersection of $t(11\text{-}1)$ and $m(11\text{-}1)$ with $t,m(200)$, are $t[011]$ and $m[011]$, respectively. These zone axes are parallel to each other and they both make an angle of $44.4°$ with the c axis of each lattice.[12] Therefore, the c axes of the parent and daughter phases must be parallel to each other. From these calculations we can write the following plane and direction relationships:

$$m(100)//t(100) \quad \text{and} \quad m[001]//t[001].$$

The transformation-produced monoclinic nanocrystallite F has the following properties:

(a) the $m(11\text{-}1)$ interplanar spacing is $\sim 2\%$ smaller than the bulk standard;

(b) the $m(11\text{-}1)\text{-}(200)$ interplanar angle is distorted to $\sim 64°$ compared to a standard value of $58.4°$; and

(c) broad dark and light bands, with approximate periodicity of 2 nm, are superimposed on the $m(200)$ lattice fringes.

Further work is needed to distinguish between Moiré patterns, twinning, and/or strain as sources of the broad band contrast. Twinning has been observed frequently in dopant stabilized zirconia-alumina composites.[3,13,14] However, those composites have micron sized zirconia crystallites with twin structures that are much wider than the individual zirconia nanocrystallites studied here. The transformation structure found in this work is typical for the nanolaminate. This localized and constrained transformation is the likely source of toughness of this material.

Figure 3 shows the size distribution of the zirconia nanocrystallites in the zirconia/alumina multilayer. These sizes were measured from the digitized lattice images by outlining the edges of individual nanocrystallites and fitting the outlines with ellipses. The minor axis [Fig. 3(a)] measures the projected particle size in the direction perpendicular to the substrate (i.e., the film growth direction). The average dimension of (4.8 ± 0.8) nm is in close agreement with the nominal film thickness of 4.5 nm. This result is also in accordance with our previous measurements using double angle XRD.[1] The XRD study of nanolaminates grown on Si substrates was complicated by the proximity of the $Si\{111\}$ reflection to the zirconia $\{111\}$ reflections. However, for a nanolaminate grown under identical conditions on silica, analysis of the XRD peak broadening gave an average crystallite dimension of 4 nm.[1]

The major axis in Fig. 3(b) measures the projected particle size in the plane of the nanolaminate. An average value of (9.9 ± 2.3) nm was obtained from the HREM measurements. This particle size was inaccessible in the XRD studies as it is parallel to the substrate surface. It is important to note the 1:2 ratio of the particle sizes obtained from Fig. 3. This result supports the expanding hemispherical cap growth model for the zirconia nanocrystallites:[4] The particle size in the film growth direction corresponds to the radius of the hemisphere, while the particle size parallel to the substrate corresponds to the diameter of the hemisphere.

HREM does not contain direct information about crystallite sizes in the direction parallel to the electron beam. However, for the studied zirconia nanolaminates, it is reasonable to assume that this third particle dimension is identical to any direction which is parallel to the substrate. This gives that the average particle size in the beam direction should be ~ 10 nm. Knowledge of this average nanocrystallite thickness allows us to estimate the errors in lattice spacing measurements which arise from crystal tilt. For a 10 nm thick monoclinic crystallite, HREM would show the $m(11\text{-}1)$ lattice fringes as long as the $(11\text{-}1)$ crystal planes are tilted by less than $1.8°$ with respect to the incident electron beam. At this extreme tilt, the $m(11\text{-}1)$ lattice spacing would appear smaller than the bulk spacing by 0.05%, which is negligible compared to the $\sim 2\%$ spacing reduction measured from Fig. 2.

IV. SUMMARY

In conclusion, we found that most tetragonal crystallites grow with their $\{111\}$ planes parallel to the growth interface. The $t\{111\}$ planes are the most densely packed in tetragonal zirconia, and as such are thermodynamically favored to grow parallel to the amorphous substrate.[15] Quantification of zirconia nanocrystallite size indicates that they grow as expanding hemispherical cap nuclei with an average radius equal to the layer thickness. All monoclinic crystallites were found to be products of transformation from the tetragonal phase. The fingerprint of this transformation is a $\sim 9°$ tilt of $m(11\text{-}1)$ with respect to $t(11\text{-}1)$. Plane and direction relationships are: $m(100)//t(100)$ and $m[001]//t[001]$. This orientation relationship has frequently been observed in the transformation of bulk zirconia.[3] However, in contrast to bulk zirconia behavior, the martensitic transformation was localized to nanosized regions in the zirconia-alumina nanolaminates.

ACKNOWLEDGMENTS

M. Gajdardziska-Josifovska and C. R. Aita

[1] C. M. Scanlan, M. Gajdardziska-Josifovska, and C. R. Aita, Appl. Phys. Lett. **64**, 3548 (1994).

[2] C. M. Scanlan, M. D. Wiggins, M. Gajdardziska-Josifovska, and C. R. Aita, MRS, Proc. **343**, 481 (1994).

[3] See, for example, D. J. Green, R. H. J. Hannink, and M. V. Swain, *Transformation Toughening of Ceramics* (CRC, Boca Raton, FL, 1989).

[4] C. R. Aita, Nanostruct. Mater. **4**, 257 (1994).

[5] R. C. Garvie and M. V. Swain, J. Mater. Sci. **20**, 1193 (1985).

[6] C. R. Aita, US Patent Serial Number 5472795; C. R. Aita, M. D. Wiggins, R. Whig, C. M. Scanlan, and M. Gajdardziska-Josifovska, J. Appl. Phys. (in press).

[7] W. J. de Ruijter, M. Gajdardziska-Josifovska, M. R. McCartney, R. Sharma, D. J. Smith, and J. K. Weiss, Scanning Microsc. **6**, 347 (1992).

[8] W. J. de Ruijter, J. Comput. Assist. Microsc. **6**, 195 (1994).

[9] W. J. de Ruijter, R. Sharma, M. R. McCartney, and D. J. Smith, Ultramicroscopy **57**, 409 (1995).

[10] ASTM Joint Committee on Powder Diffraction Standards, 1974, File Nos. 13-307 and 17-923.

[11] M. Gajdardziska-Josifovska, M. R. McCartney, W. J. de Ruijter, C. M. Scanlan, and C. R. Aita, in *Proceedings of the 52nd Annual MSA Meeting*, edited by G. W. Bailey and A. J. Garratt-Reed (San Francisco Press, San Francisco, CA, 1994), pp. 754–755.

[12] A. G. Jackson, *Handbook of Crystallography for Electron Microscopists and Others* (Springer, New York, 1991), pp. 45, 54.

[13] A. H. Heuer, S. Kraus-Lanteri, P. A. Labun, V. Lanteri, and T. E. Mitchell, Ultramicroscopy **18**, 335 (1985).

[14] M. L. Mecartney and M. Rühle, Acta Metall. **37**, 1859 (1989).

[15] E. Bauer, in *Single Crystal Films*, edited by M. H. Francombe and H. Sato (MacMillan, New York, 1964), pp. 43–67.

J. Appl. Phys., Vol. 79, No. 3, 1 February 1996

M. Gajdardziska-Josifovska and C. R. Aita   1319

Transmission electron microscopy study of zirconia–alumina nanolaminates grown by reactive sputter deposition. Part I: zirconia nanocrystallite growth morphology

M.A. Schofield[a,b,*], C.R. Aita[a,c], P.M. Rice[d], M. Gajdardziska-Josifovska[a,b]

[a]University of Wisconsin-Milwaukee, Laboratory for Surface Studies, P.O. Box 413, Milwaukee, WI 53201, USA
[b]University of Wisconsin-Milwaukee, Department of Physics, P.O. Box 413, Milwaukee, WI 53201, USA
[c]University of Wisconsin-Milwaukee, Materials Department, P.O. Box 784, Milwaukee, WI 53201, USA
[d]Oak Ridge National Laboratory, Metals and Ceramics Division, P.O. Box 2008, Oak Ridge, TN 37831, USA

Abstract

Pure zirconia films and zirconia–alumina nanolaminate films grown by reactive sputter deposition are studied by high resolution transmission electron microscopy (HRTEM) and electron energy loss spectroscopy (EELS). The phase composition and morphology associated with zirconia crystallite growth are investigated by examining films containing zirconia layers of varying thickness. These studies, performed at room temperature, suggest that the zirconia crystallites initially grow in the tetragonal phase to a critical size of 6.0 ± 0.2 nm, in agreement with a value of 6.2 nm predicted by end-point thermodynamics. Past the critical size, incorporation of additional zirconia molecules into the zirconia layers is accomplished predominantly by transformation of the growing crystallites to the monoclinic phase, and less frequently by deposition of amorphous zirconia. Transformation to the monoclinic phase is accompanied by a highly faulted intermediary phase. The subsequent growth behavior of monoclinic crystallites is consistent with a three-dimensional interface-controlled, diffusion-limited growth process with a growth exponent between 3 and 4. Nanoindentation measurements of nanolaminates with 5-nm thick zirconia layers give a hardness of ~8 GPa for the upper strata where the morphology of the tetragonal zirconia layers contains an intrinsic roughness. The hardness increases to ~10 GPa closer to the substrate where the laminar morphology is more pronounced. Young's modulus is between 156 and 195 GPa for these same nanolaminates. © 1998 Elsevier Science S.A. All rights reserved

1. Introduction

Ceramic systems containing zirconia have commonly been used as transformation toughening materials [1]. The improved mechanical properties of these materials rely upon the room temperature stabilization of the high temperature (1150–2360°C) tetragonal phase of zirconia, which is commonly achieved by addition of a dopant material [2–4] (e.g. as in yttria stabilized zirconia) or by limiting the zirconia crystallite size [5–7]. Under application of stress, the metastable tetragonal zirconia undergoes a diffusionless, martensitic transformation to the stable room temperature

monoclinic phase. Furthermore, the transformation product in these systems exhibit a faulted structure that, for example, inhibits crack propagation through the material so as to improve the material's mechanical properties. From a technological standpoint, it is of considerable interest to develop a thin-film system that functions effectively as a transformation toughening system, for example, for use as a protective coating.

Recently, multilayer films consisting of alternating layers of polycrystalline zirconia and amorphous alumina have been grown by reactive sputter deposition [8,9]. X-ray diffraction (XRD) studies have shown the zirconia phase composition of the zirconia–alumina multilayer films to be strongly dependent upon the zirconia layer thickness [10]. Near-unity volume fraction of the tetragonal phase is pre-

* Corresponding author. Tel.: +31 414 2296440; fax: +31 414 2295589; e-mail: marvin@csd.uwm.edu

sent (compared with the monoclinic phase) when the zirco-nia layer thickness is less than about 6 nm. The room tem-perature stabilization of tetragonal zirconia is accomplished within these multilayer films independent of the kinetic parameters that control tetragonal zirconia growth in thick, single layer zirconia films [11], and without the addi-tion of a stabilizing dopant.

In part I of the present study, the phase composition and morphology of zirconia–alumina multilayer films as a func-tion of the zirconia layer thickness is examined using high resolution transmission electron microscopy (HRTEM). Electron energy loss spectroscopy (EELS) is used to inves-tigate the composition of pockets of weaker scattering mate-rial (compared with the surrounding polycrystalline zirconia) observed in thicker zirconia films, and nanoinden-tation experiments are performed to determine experimental values for the hardness and Young's modulus of zirconia–alumina multilayers consisting of size-stabilized tetragonal zirconia nanocrystallites. In part II [12] of this study, we perform in situ electron microscopy experiments, using electron beam irradiation and sample cooling, to investigate post-deposition stress-induced tetragonal to monoclinic transformation of zirconia crystallites.

2. Background

Previous XRD studies have been performed on a series of zirconia–alumina films with varying zirconia layer thick-ness from 5 to 30 nm [10]. The average tetragonal and monoclinic crystallite dimensions perpendicular to the sub-strate were determined from diffraction peak broadening [13]. Fig. 1 summarizes the results from the XRD data. The average dimension of monoclinic crystallites (▲) in-creases with zirconia layer thickness, while the tetragonal dimension (●) saturates at ~6 nm, independent of the phase composition of the zirconia layers.

To understand the dependence of the zirconia layer thickness upon the average tetragonal grain size perpendi-cular to the substrate, as seen in Fig. 1, we considered the thermodynamic effects of a finite crystallite size on the spontaneous transformation from the tetragonal to the monoclinic phase [5]. HRTEM imaging showed that the shape of the tetragonal zirconia nanocrystallites was ap-proximately rectangular, with the average crystallite size in the film growth direction half of their average size in the plane of the film [14]. This 1:2 size ratio supported the use of an unconstrained hemispherical cluster model as a first approximation for the initial stages of zirconia growth [10], the results of which gave a critical radius, r_c, for growth-induced tetragonal to monoclinic: transforma-tion:

$$r_c = -3 \, \Delta\gamma_{fv} / \Delta g \qquad (1)$$

where g is the volume free energy, and γ_{fv} is the surface energy of the film-vapor interface for a particular phase.

Eq. (1) is also obtained by considering a rectangular crys-tallite with a height r and base $2r \times 2r$, in closer agreement with crystallite shapes observed by HRTEM. Values for the energy terms in Eq. (1) are $\Delta g = -2.85 \times 10^8$ $(1 - (T/1448 \text{ K}))$ J/m^3, where T is the growth temperature [15], and $\Delta\gamma_{fv} = 0.360$ J/m^2 [5]. At the growth temperature of 564 K used here, $r_c = 6.2$ nm. This value is in excellent agreement with the experimentally observed saturation value of $<r_t> = 6.0 \pm 0.2$ nm (Fig. 1) which was mea-sured at room temperature.

The agreement between the thermodynamic predictions and the experimental observations suggest three regions of interest with respect to zirconia layer phase composition and morphology. For zirconia layer thickness much less than the critical dimension of 6.2 nm, the observed crystallites are expected to grow as tetragonal. At the opposite extreme of zirconia layer thickness (much larger than 6.2 nm) the zir-conia crystallites are expected to be monoclinic. Intermedi-ate zirconia layer thickness (near to, or somewhat larger than 6.2 nm) should display characteristics of the tetragonal to monoclinic transformation occurring during growth. The principal aim of the present study is to examine these var-ious regimes in order to explore the modes of tetragonal zirconia growth, the growth-induced tetragonal to monocli-nic transformation, and the subsequent growth of monocli-nic zirconia crystallites.

3. Experimental

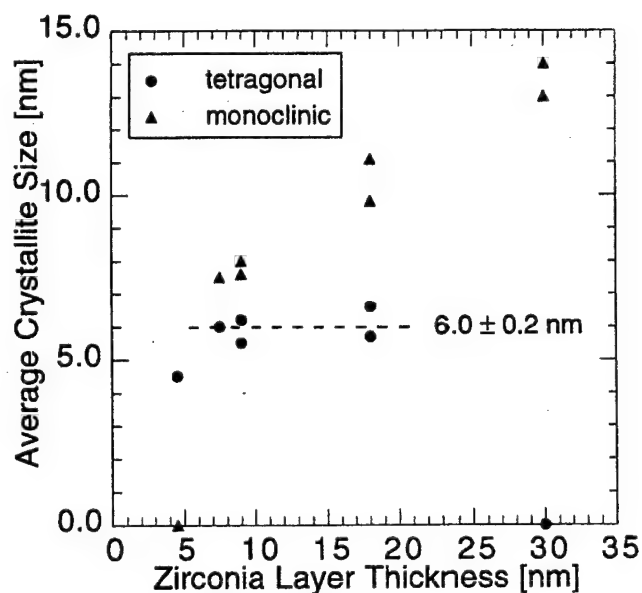Zirconia–alumina multilayer, and single layer zirconia

Fig. 1. Summary of XRD data from Ref. [10]. Average tetragonal and monoclinic zirconia crystallite sizes perpendicular to substrate are plotted vs. zirconia layer thickness. Monoclinic crystallite size (▲) increases with zirconia layer thickness, while tetragonal crystallite size (●) saturates at about 6 nm in agreement with the thermodynamically predicted size of 6.2 nm for tetragonal to monoclinic transformation.

Table 1

Summary of zirconia films prepared for HRTEM

Film	Type	Zirconia thickness (nm)	Alumina thickness (nm)	Number of zirconia layers
A[*]	Constant thickness multilayer	4.5	4	50
B[a]	Constant thickness multilayer	5	5	10
C	Variable thickness multilayer	6, 9, 12, 18, 23, 35	10	6
D	Variable thickness multilayer	35, 23, 18, 12, 9, 6	10	6
E	Single layer	110	NA	1

[a]For film B, the alumina layer was grown first. The rest of the films had zirconia as the first layer.

films were grown on various substrates by reactive sputter deposition in a multiple-target rf diode system. Si(111) wafers were used as substrates for HRTEM experiments, and sapphire, fused silica, and glass were used as substrates for nanoindentation experiments. A general description of the system geometry and the deposition parameters used to grow the films can be found in Refs. [9,10,14].

Table 1 summarizes the samples prepared for study by HRTEM. Films A and B are multilayers consisting of alternating zirconia and alumina layers, each of constant thickness. Films A and B were grown with very similar architectures, the principal difference being the initial ordering of the multilayer structure, i.e. zirconia first for film A and alumina first for film B, and only minor variation in the zirconia layer thickness between samples, i.e. 4.5 nm for film A and 5 nm for film B. In addition, we grew multilayer zirconia–alumina samples that consisted of variable zirconia layer thickness within a single sample. Films C and D contained six zirconia layers interlaced with alumina layers of constant thickness of ~10 nm. Film C comprised a thin to thick sequencing of zirconia layers of thickness 6, 9, 12, 18, 23, and 35 nm, while film D was grown with the reverse thick to thin sequencing of zirconia layers. Finally, single-layer pure zirconia films were also grown for study by HRTEM. Film E was produced by continuous zirconia deposition to a film thickness of 110 nm.

Samples A–E were prepared in cross-section for HRTEM study by sandwiching as-grown films together and preparing 3-mm disks with the film–substrate interface oriented parallel to the disk normal, i.e. parallel to the direction of the electron beam in the microscope. The 3-mm disks were mechanically thinned and polished in stages of increasingly finer abrasive to a thickness of about 100 μm with a 0.05-μm grain alumina polish as the final polishing step. The centers of the 3-mm disks were further thinned in stages to about 10 μm (while leaving the outer rim of the disks at about 80 μm) by mechanically polishing the disks with a rotating spherical polishing wheel. The final step of sample preparation was to use low-angle ion milling with 5 and 2.5 keV argon

ions to further thin and polish the centers of the samples just to perforation.

HRTEM work was performed with a Hitachi H-9000-NAR transmission electron microscope having a point resolution of 1.9 Å at an operating voltage of 300 kV. The microscope was equipped with a Gatan Multi-Scan CCD camera to record digital images from which quantitative analysis was performed. Phase identification was made from high resolution digital images by calculating numerical diffractograms of individual zirconia crystallite regions and measuring diffractogram spot positions corresponding to lattice fringe spacings in the original HRTEM digital image [16–18]. Film E was also studied by EELS using a Philips CM200 FEG electron microscope equipped with a Gatan 666 parallel EELS and external computer controlled spectral imaging system by EMiSPEC.

Table 2 summarizes the samples prepared for nanoindentation studies. The three films examined in this study were prepared identically on substrates of sapphire, fused silica, and glass. The zirconia and alumina layers were held to a constant thickness throughout the multilayer structure of the films: 4.5 nm for both the zirconia and alumina layers. The total film thickness for the samples was 1.5 μm. Nanoindentation measurements were made with a Nanoindenter II™, a fully automated ultra-low load microindentation hardness tester, with a Berkovitch diamond indenter tip. The indenter load and displacement were continuously monitored as the load was applied and removed, with a resolution of 0.3 μN (30 μg) and 0.16 nm, respectively. Hardness and elastic modulus measurements were obtained from an analysis of the load displacement curves in accordance with the methods described elsewhere [19].

4. Results and discussion

Three thermodynamic regimes are of interest based on the comparison of the zirconia layer thickness and the theoretically predicted critical crystallite size for tetragonal to monoclinic transformation. These regimes are identified below as sub-critical (zirconia layer thickness ≤5 nm), transitive (6–12 nm), and super-critical (>12 nm).

4.1. Sub-critical zirconia layer thickness

4.1.1. Morphology and crystallography

Fig. 2 shows a selected area diffraction (SAD) pattern

Table 2

Summary of zirconia–alumina multilayers prepared for nanoindentation

Film	Substrate	Zirconia thickness (nm)	Alumina thickness (nm)	Total film thickness (μm)
1	Sapphire	4.5	4.5	1.5
2	Fused silica	4.5	4.5	1.5
3	Glass	4.5	4.5	1.5

obtained from film B. and is representative of SAD patterns obtained from both films A and B containing zirconia layers ~5 nm in thickness. Using the silicon substrate as a calibration standard, the rings in Fig. 2 are indexed as tetragonal zirconia. No rings due to monoclinic zirconia or to crystalline alumina are observed. These results are consistent with previous XRD studies of similar films (see Fig. 1) and also with the thermodynamic predictions discussed above.

Fig. 3 shows a low magnification bright-field image of film B in cross-section, illustrating the overall nanolaminate structure. The silicon substrate and nascent silica layer are shown at the bottom of the micrograph. The alumina layers, appearing light in the image, clearly separate the polycrystalline zirconia layers, which appear dark. Fig. 3 shows that the laminar structure of the film loses definition away from the substrate compared with the region nearer the substrate. The effect of laminar structure deterioration on film hardness is discussed in Section 4.1.2.

HRTEM imaging of the zirconia layers of films A and B showed that the size of individual zirconia crystallites perpendicular to the substrate was invariably equal to the zirconia layer thickness. Zirconia crystallite dimensions parallel:perpendicular to the substrate were in an approximate 2:1 ratio consistent with the crystallite model discussed in the Section 2. Fig. 4 shows a typical HRTEM image of a zirconia crystallite in the as-grown film B. The lattice fringes, seen as horizontal lines in Fig. 4, are oriented parallel to the substrate, which is not shown in the image, and are an overwhelming feature of zirconia crystallites in films A and B. These lattice fringes correspond to the tetra-
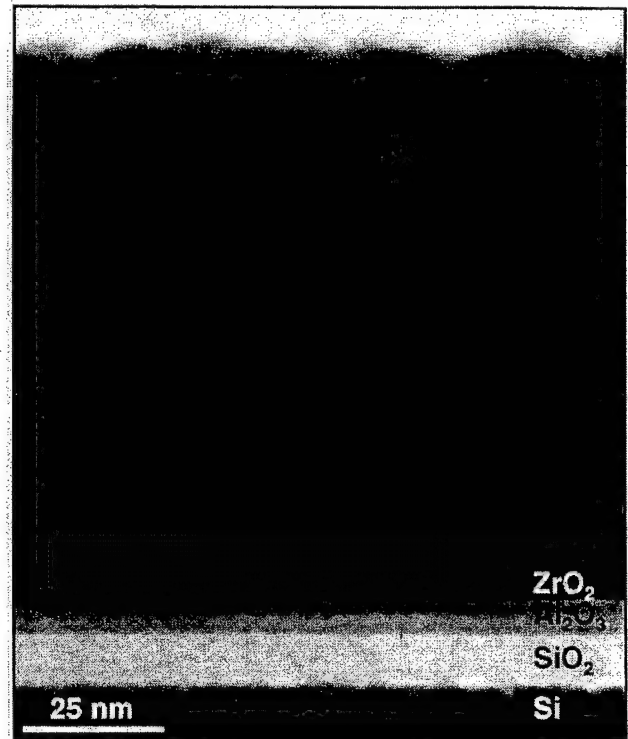

Fig. 3. Bright-field transmission electron micrograph illustrating overall nanolaminate structure of film B. Zirconia and alumina layers are each about 5 nm thick and silicon substrate is shown at bottom of image. Micrograph shows laminate structure of film looses definition away from substrate.

gonal (111) planes of zirconia. The (111) planes are the closest-packed planes in tetragonal zirconia, and crystallite growth with these planes oriented parallel to the substrate is expected from free energy considerations [20].

HRTEM imaging of the zirconia layers of films A and B also showed a small fraction of crystallites with lattice spacings and/or interplanar angles that differed from tabulated values for tetragonal or monoclinic zirconia [21] by more than the experimental error associated with the measured values. Fig. 5 shows an HRTEM image of one such crystal-

Fig. 2. SAD pattern from zirconia–alumina nanolaminate consisting of 5-nm thick zirconia layers. Pattern is indexed completely as polycrystalline zirconia in tetragonal phase. No evidence for crystalline alumina nor monoclinic phase of zirconia is present.
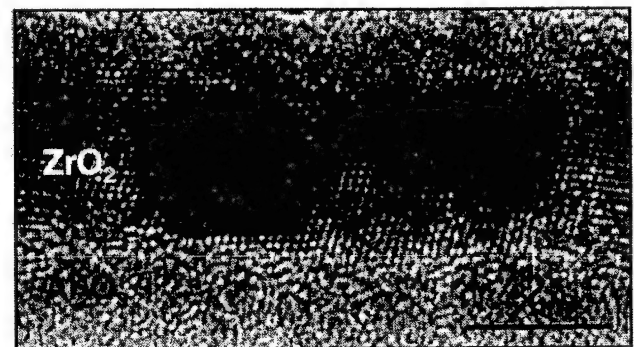

Fig. 4. HRTEM of a 5-nm thick zirconia layer showing a typical region containing zirconia crystallite. Lattice planes of crystallite imaged in micrograph are indexed as belonging to the tetragonal phase.
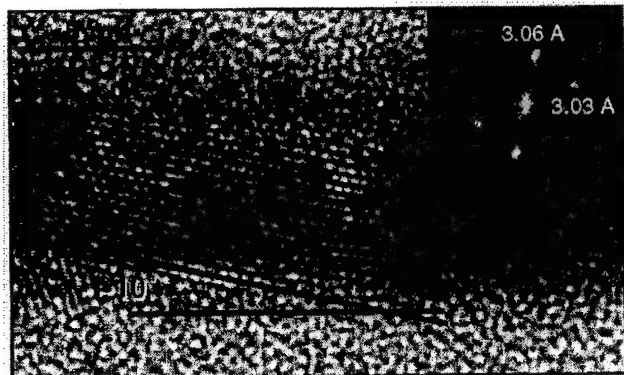
Fig. 5. HRTEM of a 5-nm thick zirconia layer showing crystallite with lattice spacings deviating from tabulated values for tetragonal zirconia, e.g. tetragonal (111) lattice spacing is 2.96 Å. Approximate 10° tilt of lattice fringes relative to substrate is characteristic of these crystallites.

lite. Characteristic features shown in Fig. 5 are the tilting of the lattice fringes parallel to the substrate by about 10°, and the distortion in spacing of these same lattice fringes to a value 2–4% larger than the bulk tetragonal (111) spacing, but 3–5% smaller than the bulk monoclinic (11$\bar{1}$) spacing. The faulted zirconia grains, as represented in Fig. 5, were previously interpreted as stress-induced monoclinic grains, stipulated to be produced by mechanical stress during HRTEM sample preparation [14]. However, it cannot be ruled out that the grains are produced during deposition, and represent characteristics of the initial stages of the growth-induced tetragonal to monoclinic transformation.

4.1.2. Mechanical properties

For purposes of testing the mechanical properties of multilayer films with sub-critical zirconia layer thickness, identical samples were prepared on three different substrates as summarized in Table 2. Substrates were chosen with largely varying mechanical properties so that effects of the substrate could be deconvolved from the nanoindentation results [22]. This is done by looking for a convergence of measurements made on the different samples. A series of indentations were made on each sample and a hardness value was calculated for each indentation as a function of the contact depth of the indenter.

Fig. 6a shows that the substrate contributions dominate the hardness measurements at large contact depths. For more shallow indentations, the effects of the substrate be-
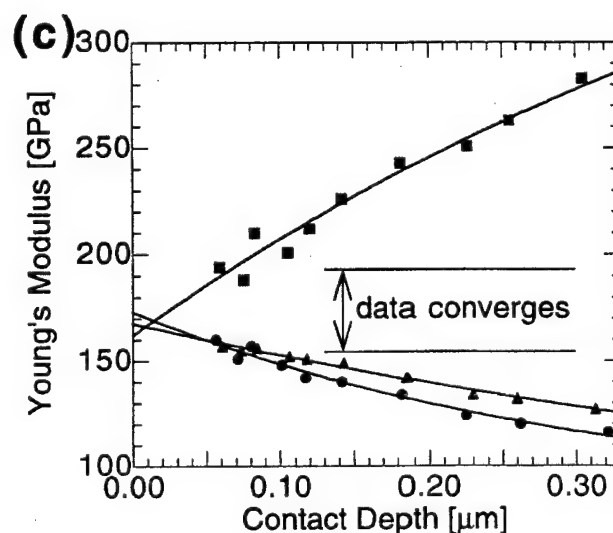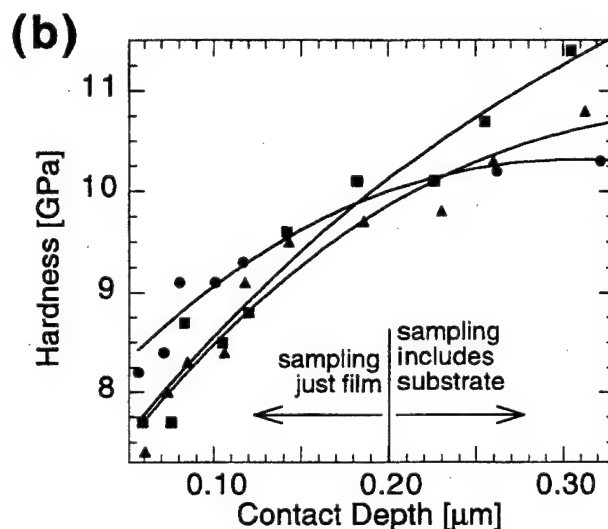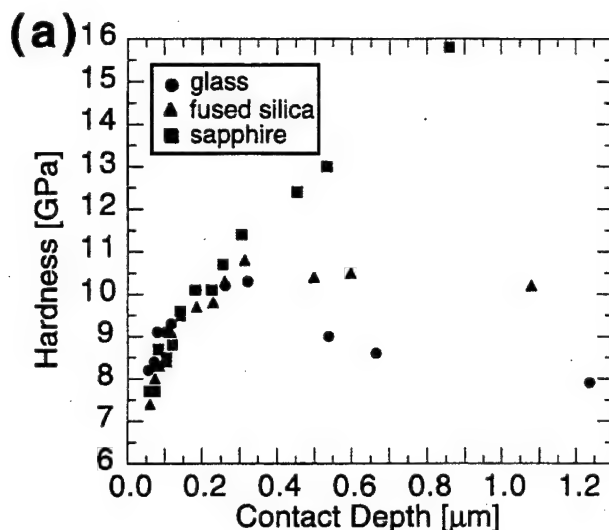

Fig. 6. Summary of results from nanoindentation experiments performed on identical samples with various substrates. (a) Hardness for each indentation is plotted vs. contact depth of indenter tip. Effects from substrate dominate results for large contact depths where hardness curves diverge. (b) Magnified convergence region of Fig. 6a showing for smaller contact depths hardness values obtained by sampling just film. Hardness decreases from ~10 GPa when sampling nearly the entire multilayer, to ~8 GPa when sampling just the top-most layers of laminate. (c) Young's modulus for each indentation is plotted vs. contact depth of indenter tip. Values obtained give upper and lower limit of 195 and 156 GPa for Young's modulus of films.

come negligible so that sampling includes just properties of the film. This is seen as a convergence of measured values obtained from the samples with different substrates. The convergence region of Fig. 6a is shown in greater detail in Fig. 6b where there is a convergence in the data at about 200 nm contact depth, corresponding to a hardness of the multi-layer film of about 10 GPa. The hardness of the film drops off to less than 8 GPa as the sampling depth is further decreased. This phenomena is an important consequence of the nanolaminate structure of the films. There is an intrinsic roughness to the laminate structure of the films that increases within layers the farther they are away from the substrate (see Fig. 3). For shallow indentations, sampling is primarily from regions of the film where the nanolaminate structure is irregular. In this case the hardness of the film is not representative of the nanolaminate structure, but rather representative of the hardness of polycrystalline tetragonal zirconia and amorphous alumina. A more reliable value for the hardness of the nanolaminate is obtained from values corresponding to the largest contact depths that sample only the film, i.e. a hardness of ~10 GPa. This value represents a lower limit to the hardness of similar multilayers with a smaller total thickness, and therefore a more regular laminar structure. This distinction is made since much thinner films would likely be used in practical applications of this nano-laminate system.

The Young's (elastic) modulus was determined from the analysis of the unloading curves of each of the indents for which the hardness was measured [22]. The Young's modulus is much more sensitive to the elastic properties of the substrates than the hardness, as is shown by the fact that the modulus curves in Fig. 6c did not completely converge. Thus the values measured represent an upper and lower limit of Young's modulus for the film of 195 and 156 GPa.

4.2. Transitive zirconia layer thickness

From the thermodynamic considerations discussed in Section 2, the 9-, 12-, 18-, 23-, and 35-nm thick zirconia layers of film C are thick enough to support tetragonal to monoclinic transformation during growth. A crystallite–by-crystallite analysis of HRTEM images of the zirconia layers of film C confirm the general results from XRD, presented in Fig. 1, that the volume fraction of monoclinic zirconia increases with zirconia layer thickness, and that, typically, no large tetragonal grains were present in the intermediate and thicker zirconia layers [23]. The crystallite shapes and sizes varied depending upon the zirconia layer thickness. In this section we will concentrate on the 6-, 9-, and 12-nm layers of film C which are close to and just above the critical size for transformation.

The first (6 nm) layer of film C showed characteristics very similar to the zirconia layers of films A and B discussed in Section 4.1.1. Within the 9-nm layer, crystallite sizes were again equal to the layer thickness in the film growth direction, i.e. perpendicular to the substrate. These particles

were block-like in shape, and their sizes ranged from one to two times the layer thickness in the plane of the film, i.e. parallel to the substrate. Fig. 7 shows a typical region of the 9-nm layer of film C. Phase analysis from HRTEM images of zirconia crystallites from this layer show a propensity for departure from the tabulated tetragonal and monoclinic values for lattice spacing and interplanar angles. Additionally, a mixture of both tetragonal and monoclinic spacings were sometimes found within an individual zirconia crystallite. This variation in spacings is evidenced by the complexity of the HRTEM images, which may also be exacerbated by a complex defect structure associated with the growth-induced transformation.

The 12-nm layer of film C also displayed a complex crystalline structure with a mixture of tetragonal, monoclinic and intermediary spacings and angles. Some crystallites were roundish in shape with a typical size parallel to the substrate slightly larger than the layer thickness. Other crystallites had sizes smaller than 12 nm in the film growth direction, and these acted as substrates for new zirconia crystallite growth [23]. Re-nucleation of zirconia crystallites was not observed in thinner zirconia layers. Fig. 8 shows an example of zirconia re-nucleation on zirconia, which is typical of the 12-nm layer, and also representative of re-nucleation within thicker zirconia layers. The re-nucleation behavior of the zirconia crystallites showed random orientation relationships to neighboring crystallites. Phase identification of re-nucleated grains gave results consistent with the thermodynamic arguments presented above for the critical size for spontaneous transformation from tetragonal to monoclinic zirconia and with the results regarding the phase composition of the transitive and super-critical zirconia layer thickness. That is, crystallites with a radius larger than about 6 nm were monoclinic, and smaller grains around 5–6 nm in size consisted of spacings
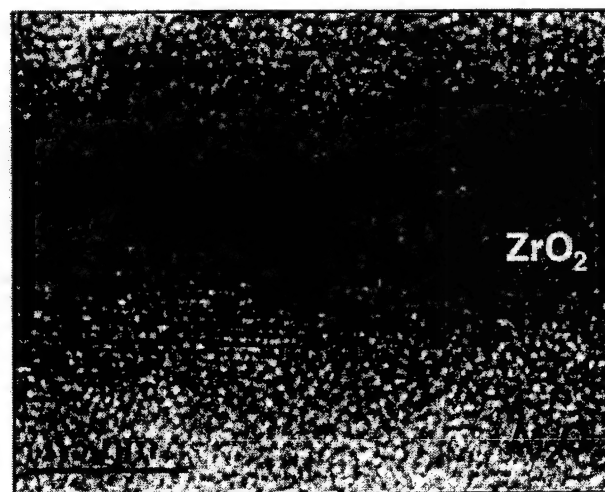

Fig. 7. HRTEM of a 9-nm thick zirconia layer. Crystallites shown in image show characteristic faulted nature of crystallites of this zirconia layer thickness. Measurements of lattice spacings give distribution of values from tetragonal to monoclinic.

Fig. 8. HRTEM of a 12-nm thick zirconia layer showing re-nucleation occurrence of zirconia crystallite. Measurements of lattice spacings present in image indicate re-nucleated crystallite is in monoclinic phase.

between that of tabulated tetragonal and monoclinic values. It should be noted though, that no re-nucleated grains with a radius less than ~5 nm were observed. Consequently, the initial phase composition of the growth nuclei is not known with certainty. However, the results presented here are suggestive and consistent with the zirconia re-nucleating in the tetragonal phase.

4.3. Super-critical zirconia layer thickness

4.3.1. Morphology and crystallography

HRTEM imaging of the thicker zirconia layers of films C and D (thickness larger than 12 nm) showed a complex crystalline structure associated with the characteristic re-nucleation and polycrystalline nature of the layers. Crystallite sizes varied somewhat within individual zirconia layers with a general increase in crystallite size as the layer thickness increased. Zirconia crystallites were typically roundish in shape, occasionally showing some small degree of faceting. Fig. 9 shows a representative larger crystallite from the 35-nm layer which can be indexed as a monoclinic zirconia crystallite. Careful analysis of large monoclinic crystallites similar to the one shown in Fig. 9 does not suggest any remnant tetragonal portion present within the large crystallite that might be left over from the tetragonal growth nucleus producing the larger grain. We conclude from this that the tetragonal to monoclinic transformation occurring during growth consumes the entire crystallite in the limit of large crystallite size.

As discussed in the Section 2, the XRD data shown in Fig. 1 is for the average crystallite size perpendicular to the substrate. Based on HRTEM imaging of zirconia layers with super-critical thickness, the crystallite size obtained by XRD is also representative of the average crystallite size parallel to the substrate. It can therefore be taken as

the average size of monoclinic grains for these zirconia layers, and will be used in Section 4.3.3 to model the monoclinic zirconia growth.

Bright-field and HRTEM imaging of the thickest (35 nm) zirconia layer of film D, and also of the single layer pure zirconia film E revealed pockets of a weaker scattering material near the substrate that were not observed in the thick zirconia layers of film C [23]. Fig. 10 is an HRTEM image of film E taken near the substrate, showing one such pocket which appears lighter than the surrounding zirconia crystallites. These pockets were present only in the lower regions of the zirconia layer at a location of about 5–7 nm from the substrate. Measurements on similar features as those shown in Fig. 10 give the lower edge of the pocket structures in films D and E to be an average distance of 6.3 nm from the film growth interface. The location of the pockets agrees well with the critical radius $r_c = 6.2$ nm for spontaneous tetragonal to monoclinic zirconia transformation predicted by end-point·thermodynamics calculations, and suggests their formation is associated with the growth-induced tetragonal to monoclinic transformation. Hence, these structures deserve further attention as discussed below.

4.3.2. Electron energy loss spectroscopy of pocket structures

Experiments were performed to determine the projected thickness of the sample in the region of the pocket structures using electron energy loss spectroscopy (EELS). If the pockets are empty, void-like structures, the thickness map is expected to show a significant decrease in thickness.
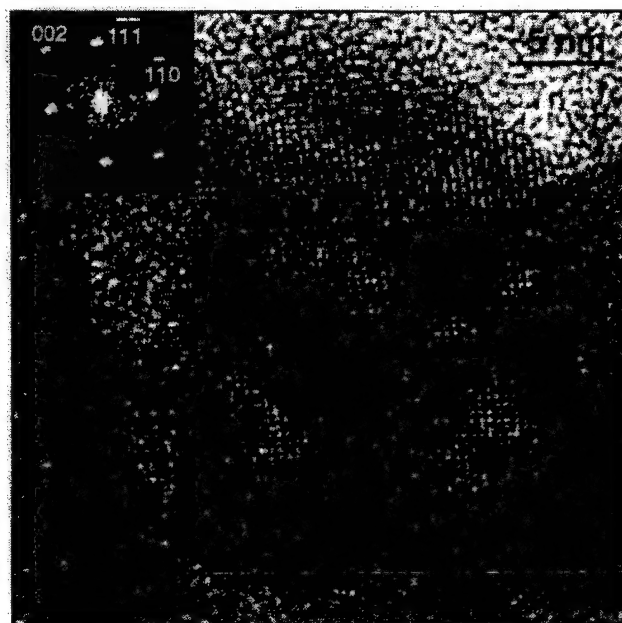

Fig. 9. HRTEM of typical monoclinic zirconia crystallite from a 35-nm thick zirconia layer. Crystallite shape is roughly circular in projection, with no departure of measured lattice spacings or interplanar angles from tabulated values for monoclinic zirconia.
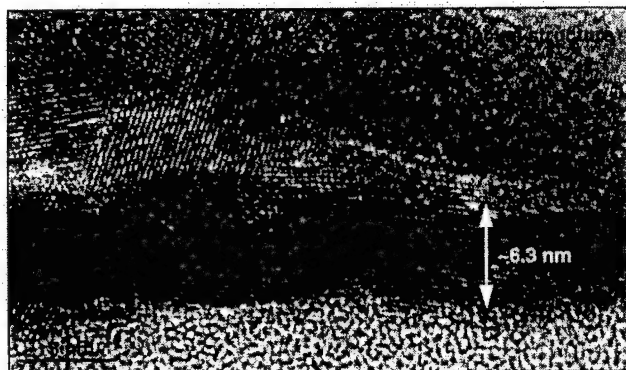
Fig. 10. HRTEM of a 110-nm thick zirconia layer (film E) showing example of pocket commonly observed in films D and E. Measurements of the pocket's distance from the substrate, on this and similar structures, give an average distance of 6.3 nm from the substrate. This value coincides with value of 6.2 nm for the critical size for spontaneous tetragonal to monoclinic transformation predicted by end-point thermodynamics calculations.

However, if the source of the lower contrast observed in HRTEM images is due to an amorphous structure, then the change in thickness is expected to be small. Previous studies have found that amorphous zirconia can be deposited by reactive sputtering of zirconium [24]. Therefore, we performed an order of magnitude EELS analysis, as described below, to distinguish between voids and amorphous zirconia as the two most likely options for the pockets.

Fig. 11a is a dark-field scanning transmission electron microscopy (STEM) image of film E (110 nm zirconia film produced by continuous deposition) with the silicon substrate shown at the bottom of the micrograph. The region of the zirconia film that contains the pocket structures appears as a dark band in Fig. 11a. EELS spectra, recorded at 0.3 eV/channel with 25 ms dwell time, were acquired at each position in a 90×60 nm array corresponding to the boxed region of Fig. 11a. A dark-current spectrum was recorded and subtracted from the data. The integrated

zero-loss peak intensity, I_0, was calculated for each EELS spectrum by integrating over a 10-eV window centered about the zero-loss peak. The total integrated intensity, I_t, was calculated for a 290-eV window from −5 to 285 eV, where the zero-loss peak position corresponds to 0 eV.

The integrated zero-loss peak intensity depends upon the sample thickness, t, as $I_0 = I_t \times e^{-t/\lambda}$, where λ is the effective mean free path for inelastic scattering, e.g. [25]. Fig. 11b shows the calculated t/λ map based on $t/\lambda = \ln I_t/I_0$ of the boxed region from Fig. 11a. Intensity profiles across regions of the map are given in Fig. 12 showing that there is a general decrease in the values for t/λ away from the substrate, corresponding to the thinner regions of the sample. In addition, there is a variation in t/λ due to a local roughness in the sample thickness. The line profile taken across one of the pockets (dashed line in Fig. 12) shows a variation in t/λ about two to three times larger than the variation in the sample thickness (solid line in Fig. 12). The pocket shown in Fig. 11b is representative in both size and shape of other structures observed in the thick zirconia films, so is taken as a basis for an order of magnitude analysis as follows.

For an incident electron energy of 200 keV, the mean free path for inelastic scattering, λ (nm), can be calculated from [25]:

$$1/\lambda = 7.6 \times 10^{-5}\, E\, In\, 400\, \beta/E \qquad (2)$$

where E is the mean energy loss of incident electrons which depends upon the chemical composition of the scattering material, and β is the spectrometer collection semi-angle. The mean energy loss for zirconia is estimated to be $E \approx 23$ eV [25]. The collection semi-angle is taken to be $\beta \approx 15$ mrad, appropriate for data collected without an angle-limiting aperture [25]. From Eq. (2) the mean free path for polycrystalline zirconia is approximately $\lambda \approx 103$ nm.

If we denote the mean free path of the unknown material contained within the pocket as λ', and assume its thickness in the direction of the electron beam is t', the ratio of the
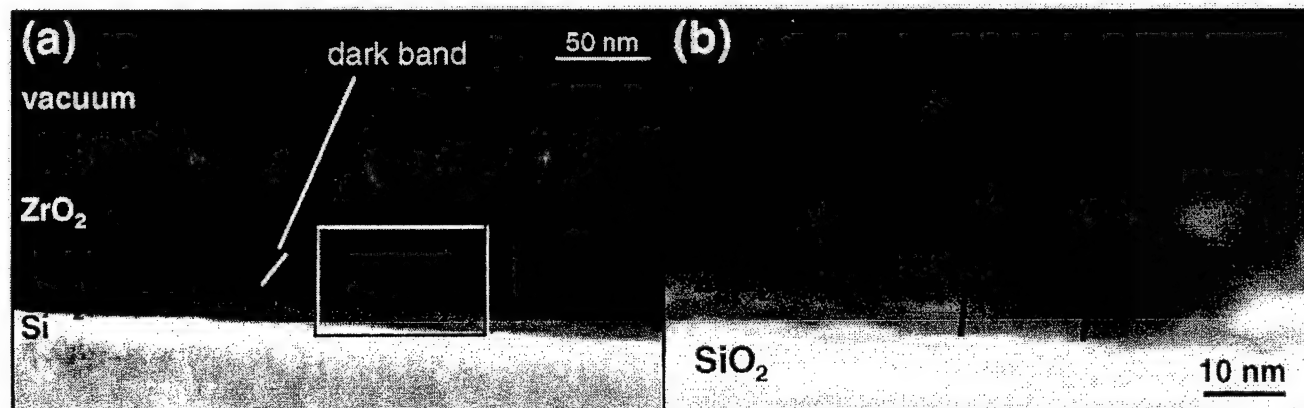

Fig. 11. (a) Dark-field scanning TEM image of a 110-nm thick zirconia layer (film E) showing region of film E (dark band) near substrate containing pocket structures. (b) Calculated t/λ map obtained from EELS data collected at each pixel location corresponding to boxed region of (a). Intensity profiles along lines A and B are shown in Fig. 12.

total vs. the zero-loss intensity in the area containing the pocket structure becomes:

$$(t - t')/\lambda + t'/\lambda' = (\ln I_t/I_0)_{inside} \tag{3}$$

where t is the total sample thickness in the direction of the beam. A region just outside of the pocket can be assumed to have the same total sample thickness, t, with a mean free path, λ, for polycrystalline zirconia so that:

$$t/\lambda = (\ln I_t/I_0)_{outside} \tag{4}$$

Values for the right-hand-side of Eqs. (3) and (4) were obtained from experimental data depicted in Fig. 11b by averaging two 10×10 pixel regions located the same distance from the substrate, but situated inside and just outside of the pocket: $(\ln I_t/I_0)_{inside} = 0.184$ and $(\ln I_t/I_0)_{outside} = 0194$. Combining Eqs. (3) and (4), t' is expressed in terms of the known mean free path of the surrounding polycrystalline zirconia, $\lambda = 103$ nm, and the unknown mean free path of the pocket's material, λ':

$$t' = 0.01 (1/\lambda - 1/\lambda')^{-1} \tag{5}$$

We consider, specifically, the two cases for the likely composition of the pockets: (1) vacuum ($\lambda' \to \infty$) and (2) amorphous zirconia ($\lambda' = \lambda + \delta\lambda$).

If the pockets were empty, void-like structures, the thickness obtained from Eq. (5) would be $t' = 0.01 \lambda \approx 1.0$ nm. Since the zirconia crystallites in these films do not show any preferential orientation in directions parallel to the substrate, it is expected that t' would be comparable with the observed lateral size of the pockets, i.e. t' would be expected to be of the order of 10 nm from Fig. 11b. Hence, the calculated thickness of a pocket-containing vacuum is an order of magnitude smaller than that expected on physical grounds.

If, however, the pocket structures were to consist of amorphous zirconia, we obtain from Eq. (5) the thickness of the structures $t' = 0.01 \times \lambda \times (1 + \lambda/\delta\lambda)$. An 11% increase in the inelastic mean free path of amorphous zirconia compared with that of polycrystalline zirconia (i.e. $\delta\lambda = 0.11\lambda$) would result in the correct order of magnitude for the thickness ($t' \approx 10$ nm) of the pocket structure. Such an increase in the inelastic mean free path is quite reasonable on the basis of the reduced density of an amorphous material compared with its crystalline counterpart, e.g. see Ref. [25]. Therefore we conclude that the pockets are most likely amorphous zirconia.

The coincidence of the location of the pockets with the critical dimension for spontaneous transformation from tetragonal to monoclinic zirconia is highly suggestive that their formation is associated with an energy barrier that must be overcome for the growth transformation from tetragonal to monoclinic zirconia to occur. This result implies it is energetically more favorable for a zirconia crystallite to remain in the tetragonal phase at its critical size than to incorporate additional growth nutrients and transform to the monoclinic phase.

4.3.3. Monoclinic crystallite growth

We attempted to model monoclinic crystallite growth with a classical power-law dependence of the average crystallite size on the total growth time [26]. The XRD data for monoclinic crystallites, shown in Fig. 1, was used for this purpose. The deposition rate used was constant, so the crystallite growth time is proportional to the zirconia layer thickness. The functional dependence of the monoclinic crystallite size, r, upon the deposition time, t, can be expressed as [26]:

$$r^n - r_O^n = K (t - t_0) \tag{6}$$

where t_0 is the deposition time required to produce an initial monoclinic crystallite nucleus of size r_0. The constant K is related to the deposition rate and the growth exponent, n, depends upon the growth-limiting processes present during deposition.

The value of r_0 in Eq. (6) was taken to be $r_0 = 6.2$ nm based on the thermodynamic prediction for the critical size for transformation from tetragonal to monoclinic zirconia, appropriate for the growth temperature of 564 K; $t_0 \approx 250$ s is estimated from the known deposition rate, $R = 0.025$ nm/ s, as the time required to deposit a zirconia layer thickness $r_0 = 6.2$ nm. The constant K is approximated by considering the crystallite size $r = r_0 + \delta r$ at time $t = t_0 + \delta t$, where the quantities δr and δt are small. From Eq. (6) it can be shown that:

$$K \approx n \, r_0^{n-1} \, (\delta r/\delta t) \tag{7}$$

In the limit that $\delta t \to 0$, $\delta r/\delta t$ approaches the deposition rate, R. so that:
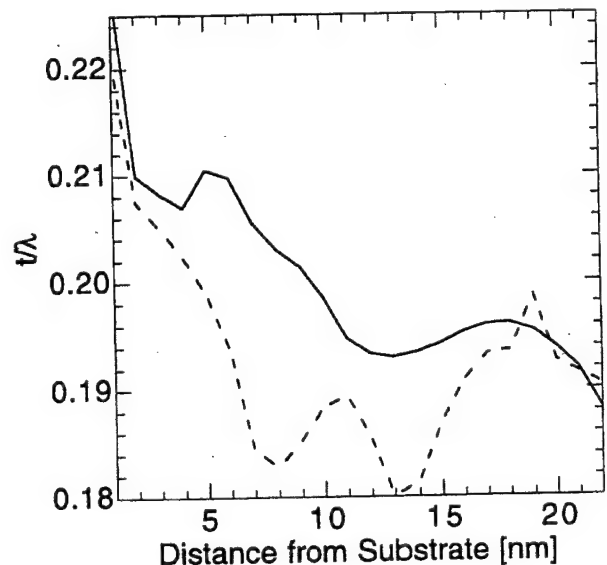

Fig. 12. Intensity profile (solid curve) along line A in Fig. 11 just outside pocket structure showing variations in t/λ due to local roughness in sample thickness. Dashed curve shows intensity profile along line B in Fig. 11, across pocket structure, where variations in t/λ are about two to three times larger than variations due to sample roughness.
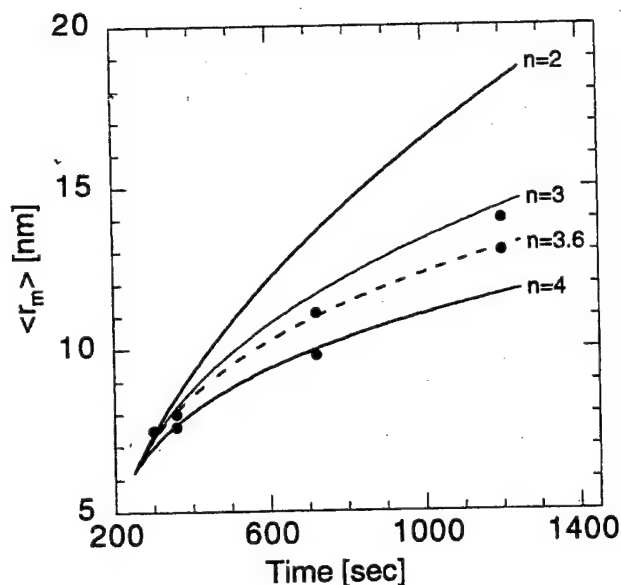
Fig. 13. XRD data for average monoclinic crystallite size, $<r_m>$, as a function of deposition time, t, (see also Fig. 1) along with power-law growth curves for growth exponents of 2, 3, and 4. Best fit curve is also plotted and corresponds to growth exponent of 3.6.

$$K \approx n\, r_0^{n-1}\, R \qquad (8)$$

Eq. (6) is plotted for growth exponents $n = 2$, 3, and 4 and compared with the experimental XRD data for the average monoclinic crystallite size as a function of deposition time. The results are shown in Fig. 13. General agreement is found for a growth exponent between 3 and 4. The best fit to the data of the power-law equation is obtained for $n = 3.6$. The results presented here are in agreement with previously reported growth exponents of $n = 3$–4 for sintered zirconia–alumina composite systems exhibiting normal grain growth behavior (see Ref. [27] and references therein).

To interpret the physical meaning of the growth exponent we have obtained, we consider the limiting process to incorporation of growth nutrients to growing crystallites. For example, we consider diffusion-limited growth and interface-controlled growth behaviors. In the case of three-dimensional particle growth, interface-controlled growth behavior predicts a growth exponent of $n = 3$, while diffusion-limited growth predicts an exponent of $n = 4$ [26]. HRTEM imaging of monoclinic zirconia crystallites from thick zirconia layers supports the assumption of three-dimensional crystallite growth occurring during deposition. Additionally, competing growth processes exist in a complex system so that integer values for the growth exponent are not necessarily expected. Hence, the best fit value for the growth exponent of $n = 3.6$ is consistent with the very reasonable interpretation of the growth behavior of the monoclinic crystallites being that of a three-dimensional interface-controlled, diffusion-limited growth process. This is the same interpretation given by Alexander et al. [27] for a sintered zirconia–alumina system consisting of ceria-doped zirconia grains in an alumina matrix where an average growth exponent of 3.45 was obtained for the zirconia grains.

5. Conclusions

An examination into the structure and morphology of zirconia crystallites growth by reactive sputter deposition has been made by HRTEM studies of pure zirconia and zirconia–alumina multilayer films of varying zirconia layer thickness. The phase composition of the zirconia layers is highly dependent upon the zirconia layer thickness and the average zirconia crystallite size. The initial nucleation and growth of zirconia is in the tetragonal phase with the (111) planes oriented parallel to the amorphous substrate. At a critical size of 6.2 nm predicted by end-point thermodynamics, transformation to a highly faulted intermediary tetragonal–monoclinic phase can occur. In some instances, the zirconia grains remain in the tetragonal phase and disordered amorphous growth of zirconia occurs over the tetragonal grains. For zirconia layer thickness between 9 and 12 nm, re-nucleation of zirconia crystallites occurs with a phase composition consistent with that predicted by thermodynamic calculations. At zirconia layer thickness about 20 nm, the phase composition is essentially unit volume fraction monoclinic zirconia. The monoclinic crystallites exhibit normal grain growth behavior (consistent with a three-dimensional interface-controlled, diffusion-limited growth process) over the range of monoclinic crystallite sizes studied, i.e. from the critical size for tetragonal to monoclinic transformation to about 14 nm.

Values for the hardness and Young's modulus are reported for zirconia–alumina nanolaminates consisting of 5-nm thick zirconia layers. The nanolaminate morphology was found to affect the hardness of the multilayer films studied here. When hardness measurements primarily involved sampling from just the upper zirconia layers of thick films, where the laminate morphology is irregular, the hardness is ~8 GPa. A lower bound of ~10 GPa is obtained for the hardness of nanolaminates when sampling includes deeper layers with more regular laminate morphology. Young's modulus for zirconia–alumina nanolaminates is found to be between 156 and 195 GPa.

References

[1] D.J. Green, R.H.J. Hannink, M.V. Swain, Transformation Toughening Ceramics, CRC Press, Boca Raton, FL, 1989.

[2] C.F. Grain, J. Am. Ceram. Soc. 50 (1967) 288.

[3] H.G. Scott, J. Mater. Sci. 10 (1975) 1527.

[4] V.S. Stubican, S.P. Ray. J. Am. Ceram. Soc. 60 (1977) 534.

[5] R.C. Garvie, J. Phys. Chem. 69 (1965) 1239.

[6] F.F. Lange, D.J. Green, in A. H. Heuer, L. W. Hobbs (eds.), Science and Technology of Zirconia I, The American Ceramic Society, Columbus, OH, 1981, p. 217.

[7] A.G. Evans, N. Burlingame, M. Drory, W.M. Kriven, Acta Metall. 29 (1981) 447.

[8] C.R. Aita, US Patent 5,472,795 (1995).

[9] C.M. Scanlan, M. Gajdardziska-Josifovska, C.R. Aita, Appl. Phys. Lett. 64 (1994) 3548.

[10] C.R. Aita, M.D. Wiggins, R. Whig, C.M. Scanlan, M. Gajdardziska-Josifovska, J. Appl. Phys. 79 (1996) 1176.

[11] C.R. Aita, Nanostruct. Mater. 4 (1994) 257.

[12] M.A. Schofield, C.R. Aita, P.M. Rice, M. Gajdardziska-Josifovska, Thin Solid Films 326 (1998) 117.

[13] L.V. Azaroff, Elements of X-ray Crystallography, McGraw–Hill, New York, 1968, pp. 551–552.

[14] M. Gajdardziska-Josifovska, C.R. Aita, J. Appl. Phys. 79 (1996) 1315.

[15] R.C. Garvie, P.S. Nicholson, J. Am. Ceram. Soc. 55 (1972) 303.

[16] W.J. de Ruijter, M. Gajdardziska-Josifovska, M.R. McCartney, R. Sharma, D.J. Smith, J.K. Weiss, Scanning Microsc. 6 (1992) 347.

[17] W.J. de Ruijter, J. Comput. Assit. Microsc. 6 (1994) 195.

[18] W.J. de Ruijter, R. Sharma, M.R. McCartney, D.J. Smith, Ultramicroscopy 57 (1995) 409.

[19] W.C. Oliver, G.M. Pharr, J. Mater. Res. 7 (1992) 1564.

[20] E. Bauer, in M.H. Francombe, H. Sato (eds.), Single Crystal Films, MacMillan, New York, 1964, pp. 43–67.

[21] ASTM Joint Committee on Powder Diffraction Standards, 1974.

[22] S.M. Gorbatkin, R.L. Rhoades, T.Y. Tsui, W.C. Oliver, Appl. Phys. Lett. 65 (1994) 2672.

[23] M.A. Schofield, R. Whig, C.R. Aita, M. Gajdardziska-Josifovska, Mater. Res. Soc. Symp. Proc. 403 (1996) 297.

[24] C.-K. Kwok, C.R. Aita, J. Vac. Sci. Technol. A 7 (1989) 1235.

[25] R.F. Egerton, Electron Energy-Loss Spectroscopy in the Electron Microscope, Plenum Press, New York, 1996.

[26] M. Hillert, Acta Metall. 13 (1965) 227.

[27] K.B. Alexander, P.F. Becher, S.B. Waters, A. Bleier, J. Am. Ceram. Soc. 77 (1994) 939.

Transmission electron microscopy study of zirconia–alumina nanolaminates grown by reactive sputter deposition. Part II: transformation behavior of tetragonal zirconia nanocrystallites

M.A. Schofield[a,b,*], C.R. Aita[a,c], P.M. Rice[d], M. Gajdardziska-Josifovska[a,b]

[a]*Laboratory for Surface Studies, University of Wisconsin at Milwaukee, P.O. Box 413, Milwaukee, WI 53201, USA*
[b]*Department of Physics, University of Wisconsin at Milwaukee, P.O. Box 413, Milwaukee, WI 53201, USA*
[c]*Materials Department, University of Wisconsin at Milwaukee, P.O. Box 784, Milwaukee, WI 53201, USA*
[d]*Metals and Ceramics Division, Oak Ridge National Laboratory, P.O. Box 2008, Oak Ridge, TN 37831, USA*

Abstract

Zirconia–alumina multilayer films consisting of polycrystalline tetragonal zirconia and amorphous alumina were grown by reactive sputter deposition to study the transformation behavior of tetragonal zirconia nanocrystallites during in-situ electron beam irradiation and cooling experiments in a transmission electron microscope. It was found that the constraint provided by the alumina layers in the nanolaminate was important in the stabilization of the tetragonal phase of the zirconia during irradiation and cooling, and overrides the thermodynamic prediction based on an unconstrained crystallite model which governs the phase composition of zirconia crystallites during growth. A partial transformation of the tetragonal zirconia crystallites to the monoclinic phase was observed in cases where the alumina constraint is greatly relaxed due to knock-on damage to the alumina layers by the electron beam of the microscope. In extreme cases of alumina loss, re-crystallization of the zirconia occurred producing larger monoclinic zirconia crystallites. Fundamentally, the nano-sized zirconia crystallites present in the films under investigation were found to have a different transformation behavior compared to micron-sized dopant-stabilized tetragonal zirconia crystallites. © 1998 Elsevier Science S.A. All rights reserved

1. Introduction

It is of much current interest to develop new nano-materials and to understand how their properties differ from those of materials with larger micro-structures. In this work we examine the transformation behavior of nano-sized tetragonal zirconia crystallites in the novel zirconia–alumina nanolaminate thin-film system using electron irradiation and cooling as stress triggers. The goal is to compare the observed behavior with prior transformation studies of zirconia–alumina composites containing micron-sized dopant-stabilized zirconia crystallites. Understanding the transformation behavior of the tetragonal zirconia nanocrystallites within the zirconia–alumina nanolaminate films

is important towards understanding the potential functionality of the films as a transformation toughening system, and more fundamentally towards understanding the basic difference between dopant-stabilized microcrystals and size-stabilized nanocrystallites.

Recently, zirconia–alumina multilayer films consisting of alternating layers of polycrystalline zirconia and amorphous alumina have been produced by reactive sputter deposition [1,2]. It was shown that the tetragonal phase is the stable phase of zirconia in these films when the zirconia layer thickness is less than about 6 nm [3], compared to the monoclinic phase which is the stable room-temperature phase of bulk zirconia. The stabilization of the tetragonal phase in the nanolaminates was an effect of the crystallite size [3,4] and was not provided by addition of a dopant material.

The effect of crystallite size on the phase composition of

---

* Corresponding author.

zirconia crystallites in the as-grown multilayer films was predicted by end-point thermodynamics calculations [3]. Using an unconstrained hemispherical island to model the initial stages of zirconia growth, the critical radius, r_c, for spontaneous transformation from tetragonal to monoclinic zirconia during growth was obtained [3]. The same results were obtained for a rectangular shaped crystallite with a square base of length twice the crystallite height, where r_c is now the height of the rectangle [5]. For both geometries the temperature dependence of r_c is given by:

$$r_c = \frac{3.79 \text{ nm}}{(1 - T/1448)} \tag{1}$$

where the growth temperature, T, is in Kelvin. At the growth temperature of 564 K, the value of $r_c = 6.2$ nm is in excellent agreement with experimental observation of the phase composition of nanolaminates grown with differing zirconia layer thickness, i.e. differing average crystallite size [3].

In composite systems with micron-sized tetragonal zirconia grains [6–8], such as yttria stabilized zirconia, the room-temperature stabilization of the tetragonal phase of zirconia by doping provides the starting condition for the system to function as a transformation toughening material [9]. Under applied mechanical stress the metastable tetragonal zirconia in these types of systems undergoes a martensitic transformation to the monoclinic phase, which exhibits a faulted structure that acts to toughen the material.

McCartney and Rühle [10] have shown that tetragonal-to-monoclinic martensitic transformation of micron-sized grains of yttria stabilized tetragonal zirconia can be induced in a transmission electron microscope by irradiation of the sample with the electron beam of the microscope. In their experiments, local stresses produced by the electron beam are assumed to be the major mechanism initiating the transformation behavior. Indeed, local heating of the sample by the focused electron beam is assumed to cause anisotropic expansion of the sample in the region of the focused beam, generating mechanical stresses simulating externally applied stresses. The present paper reports on equivalent irradiation experiments performed on zirconia–alumina multilayer films containing nano-sized grains of undoped tetragonal zirconia.

In addition to electron beam irradiation studies, experiments were performed by cooling the sample to near liquid nitrogen temperatures within the electron microscope. The non-uniform expansion of the individual zirconia and alumina layers of the nanolaminates were expected to generate interlayer shear stresses during cooling of the sample, providing a possible mechanism to initiate the tetragonal-to-monoclinic transformation in zirconia nanocrystallites. Moreover, based on Eq. (1), the stability of the tetragonal zirconia crystallites in the nanolaminate films is expected to depend upon the temperature of the sample upon achieving a thermodynamic equilibrium. Fig. 1 shows a plot of the critical crystallite size, r_c, versus temperature, T, from Eq.

(1) over the range of temperatures from zero Kelvin to above the growth temperature of the films produced for this study. Near liquid nitrogen temperatures, the phase composition of 5–6 nm sized zirconia crystallites (the size range studied here) lies well within the monoclinic region in Fig. 1. Consequently, it is expected that, in addition to the thermal stress provided during cooling of the sample, the temperature dependence of the thermodynamic stability of the crystallites will also affect the transformation behavior of the zirconia.

2. Experimental

Zirconia–alumina multilayer films were grown on Si(111) wafers by reactive sputter deposition. A general description of the system geometry and the deposition parameters used to grow the films can be found in Refs. [2,3,11]. Two types of nanolaminate films were grown for this study (denoted as films B and C in Table I of [5]) consisting of alternating zirconia and alumina layers. Film B consisted of ten 5-nm thick zirconia layers interlaced with alumina layers also of 5 nm thickness. The sequencing of zirconia and alumina layers was initiated with an alumina layer for film B. Film C contained six zirconia layers of increasing individual layer thickness and separated by alumina layers each of about 10 nm thickness. Only the first (6 nm thick) zirconia layer of film C was considered in this part of the study and it was the first layer deposited in the growth of the film.

Sample preparation for transmission electron microscopy involved producing samples with an electron transparent cross-sectional view of the nanolaminate. Three-millimeter diameter disks were prepared with the film–substrate interface oriented normal to the disk, and consequently, parallel
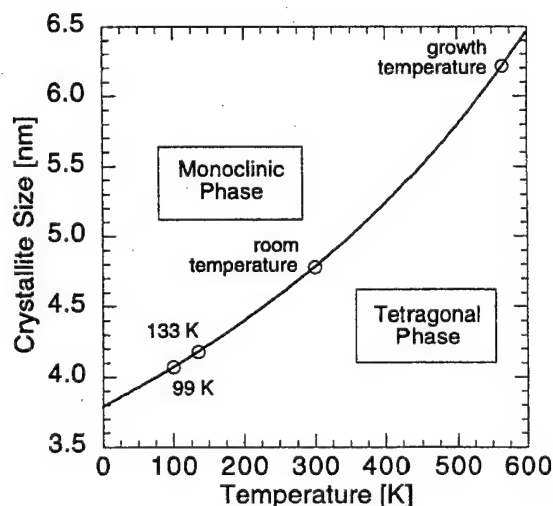

Fig. 1. Zirconia crystallite phase dependence upon crystallite size and temperature as predicted by end-point thermodynamics for unconstrained crystallites. Curve represents thermodynamic equilibrium between tetragonal and monoclinic phases.

to the electron beam of the microscope. The disks were mechanically thinned and polished with successively finer abrasives to about 10 μm thickness at the center of the disks while maintaining about an 80–100 μm thickness at the rim of the samples. Further thinning of the centers of the disks to perforation and final polishing was done by argon ion bombardment at 5 and 2.5 keV incident energies.

The polishing and ion-milling steps outlined above are standard techniques for preparation of cross-sectional transmission electron microscope samples. Sample preparation in this manner has been found to cause transformation of zirconia to the monoclinic phase in other studies of samples containing doped tetragonal zirconia microcrystals [9]. This transformation effect is much less pronounced in the tetragonal zirconia nanocrystals present in the films under investigation here [11].

Electron microscopy experiments performed at the University of Wisconsin–Milwaukee were done in a Hitachi H-9000NAR transmission electron microscope operated at 300 kV, and equipped with a Gatan multi-scan CCD camera. Additional electron microscopy experiments were performed at Oak Ridge National Laboratory using a Philips CM 200 FEG transmission electron microscope operated at 200 kV and equipped with a liquid nitrogen cooled sample holder.

For purposes of performing in-situ irradiation experiments, the digital quantum efficiency of the CCD camera was determined to be about one electron per count [12,13]. Table 1 summarizes the irradiation conditions used in this study. Normal imaging conditions for high resolution transmission electron microscopy (HRTEM), denoted as mild irradiation of the sample in Table 1, corresponded to an electron flux of about 1.3×10^{-4} nA/nm^2. By adjusting the illumination system of the microscope, moderate and extreme irradiation conditions were produced corresponding to electron fluxes of 4.8×10^{-3} nA/nm^2 and 0.13 nA/nm^2, respectively. Irradiation times from 10 s to 2 min were considered for each of the mild, moderate, and extreme irradiation conditions described above.

3. Results and discussion

3.1. In-situ electron beam irradiation

3.1.1. Gross morphology and average crystallinity

Results of many irradiation experiments varied depending in large part upon the local thickness of the sample in the

direction of the electron beam, and to a lesser extent upon the total electron dose.

In general, tetragonal-to-monoclinic transformation was observed only in cases where knock-on damage to the alumina was significant. The electron threshold energy for knock-on damage to alumina is about 187 keV [14], so that knock-on damage was expected to occur within the alumina layers at the 200 and 300 kV operating voltages used in this study. In addition, however, to the electron energy, the amount of knock-on damage depends also on the electron flux and is cumulative, i.e. increases with exposure time. Furthermore, loss of material due to knock-on damage is most prevalent at the exit face of the sample. Because of this the knock-on sputtering of alumina was observed to be most efficient and prevalent in the very thin regions of the sample. This loss of alumina, along with the observed tendency towards crystallization of the remaining amorphous alumina, had an important effect since the alumina layers act to constrain the zirconia crystallites within individual zirconia layers. When significant sputtering of the alumina occurred, the integrity of the laminate structure was compromised, and the transformation behavior of the tetragonal zirconia was no longer representative of the bulk film properties.

As mentioned in the Section 2, the sample preparation procedure produces samples with a thickness in the direction of the electron beam ranging from zero to approximately 100 μm. In very thin regions of samples, with an estimated thickness ranging from 0 to ~20 nm, the alumina sputtering was observed to occur most quickly and the transformation behavior of the tetragonal zirconia crystallites was most striking. The bright-field TEM image in Fig. 2 is a dramatic illustration of the drastic transformation behavior that occurred under extreme irradiation conditions within a few seconds of irradiating a very thin region of film B. The laminate structure of the film, present at the left side of Fig. 2, extended completely to the tip of the sample before irradiation. After a total electron dose of about 0.16 nC/nm^2, the sputtering of the alumina was such that zirconia re-crystallization between distinct zirconia layers could occur, as visible at the right side of Fig. 2. Indexing the selected area diffraction (SAD) pattern obtained from the tip of the sample (see inset of Fig. 2) after irradiation shows it to be a ~0.5 μm large monoclinic zirconia crystallite in a <011> zone axis orientation. SAD from the intact nanolaminate region of Fig. 2 shows that region of the sample to remain polycrystalline tetragonal zirconia. The intermediate regions show complex SAD pat-

Table 1

Irradiation conditions

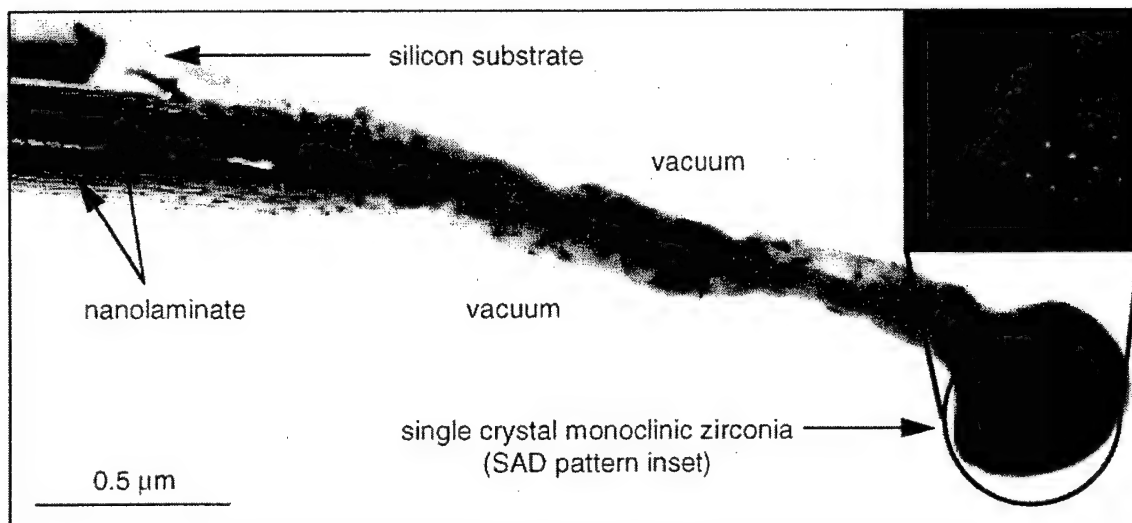|	Condenser aperture	First condenser lens	Second condenser lens	Electron flux (nA/nm^2)
Mild (imaging)	50 μm	0.1 μm spot size	Over focused	1.3×10^{-4}
Moderate	50 μm	0.3 μm spot size	Focused	4.8×10^{-3}
Extreme	None	0.1 μm spot size	Focused	0.13

Fig. 2. Bright-field TEM image from very thin region of zirconia–alumina 'nanolaminate B after total electron dose of about 0.16 nC/nm². Unirradiated portion of sample, at left of image, shows the intact film structure. Tip of sample, at right of image, is monoclinic zirconia crystallite that re-crystallized during irradiation. Inset shows SAD pattern taken from tip of sample, and is indexed as monoclinic zirconia in $\langle 011 \rangle$ zone axis orientation.

terns dominated by diffraction from large monoclinic crystallites.

In direct contrast to the irradiation results discussed above, Fig. 3 shows bright-field TEM images from a much thicker region of film B, with an estimated thickness ranging between ~50 nm and ~100 nm. The total irradiation time between the images in Fig. 3 was 8 min which corresponds to a total electron dose of about 64 nC/nm², i.e. two orders of magnitude larger than the total electron dose producing the results shown in Fig. 2. As shown in Fig. 3, a slight bending to the film is produced by irradiating the sample, but the laminar structure of the film is clearly intact. Fig. 4 shows SAD patterns corresponding to the images of Fig. 3. The diffraction rings for both the before irradiation (a) and after irradiation (b) SAD patterns of Fig. 4 are indexed completely as tetragonal zirconia. Additional SAD patterns, not shown here, recorded after each 1- and 2-min irradiation intervals comprising the entire 8 min irradiation sequence are also indexed as tetragonal zirconia, with no observable contribution from monoclinic zirconia.

Experiments conducted on regions of the sample with a moderate thickness in the direction of the electron beam (i.e. in the ~20 nm to ~50 nm range) gave results where both the tetragonal and monoclinic phases were present after irradiation with large total electron dosage. Fig. 5 is a bright-field TEM image of film B after a total electron dose of 6.5 nC/nm². The region of the sample shown in the circle was irradiated for 50 seconds under extreme irradiation conditions. Compared to the undamaged regions of the film nearby (left-part of Fig. 5) the irradiated part of the sample shows larger particles, a bending in the film, and a loss of the laminate structure, especially towards the center of the damaged region.

Fig. 6a and b are SAD patterns taken from only the circled region shown in Fig. 5 before and after the irradiation, respectively. Fig. 6a shows a ring pattern characteristic of diffraction from a polycrystalline sample, and has been indexed completely as tetragonal zirconia. Fig. 6b contains two features of interest. Firstly, there is a ring pattern similar to that shown in Fig. 6a. The rings are indexed as belonging
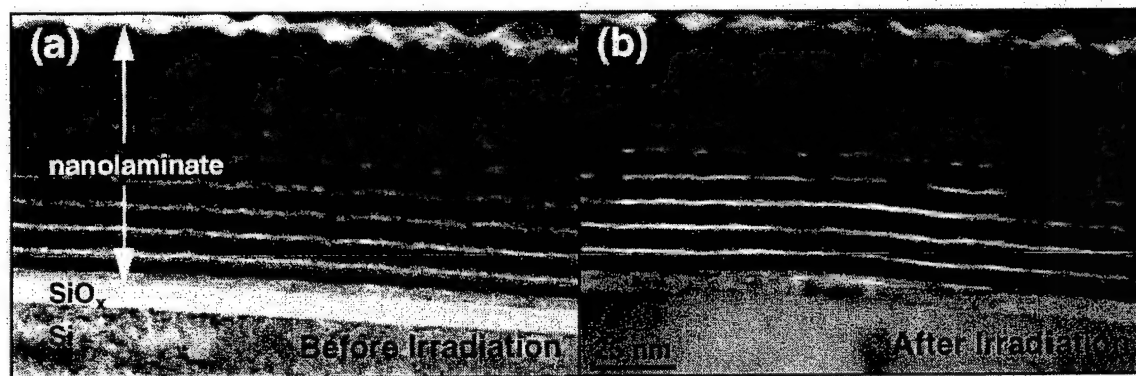

Fig. 3. Bright-field TEM image from thick region of film B (a) before and (b) after irradiation of the sample by a total electron dose of about 64 nC/nm². The laminar structure of the film remained intact after irradiation by the electron beam; however, the film suffered a slight bending due to the irradiation.
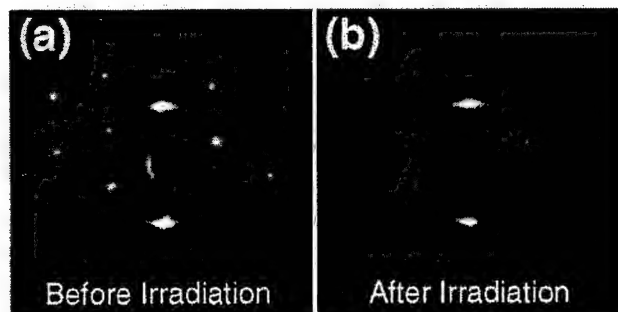
Fig. 4. SAD patterns from thick region of film B (a) before and (b) after irradiation of sample corresponding to bright-field images shown in Fig. 3a and b, respectively. Ring patterns in both a and b are indexed completely as tetragonal zirconia. Diffraction spots, especially evident in a, are due to silicon substrate of film.

to tetragonal zirconia. Secondly, there appear in Fig. 6b many distinct diffraction spots unlike any features shown in Fig. 6a. These spots are due to the larger (and relatively fewer) particles shown in the damaged region of Fig. 5. Careful analysis of Fig. 6b and its rotational average in Fig. 6c show that the spot features are due to monoclinic zirconia crystallites. Notable in Fig. 6c are the shifts in the expected tetragonal (111) and monoclinic (11-1) peak positions. The shifted peaks correspond to contribution to the diffraction pattern from zirconia crystallites with spacings that are distorted from the tabulated bulk tetragonal and monoclinic spacings. These distorted spacings are discussed in greater detail in the next section involving HRTEM imaging of individual zirconia crystallites.

The results presented above indicate that the sample thickness in the direction of the electron beam plays an important role in the transformation behavior of the tetragonal zirconia nanocrystallites. In thicker regions of the sample, where the alumina layers remain essentially intact even after prolonged exposures to extreme irradiation conditions, the zirconia crystallites remain in the tetragonal phase. In thinner regions of the sample, the transformation behavior of the zirconia depends upon the removal of mate-
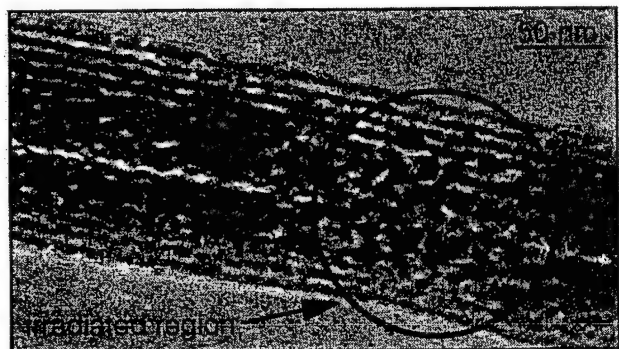

Fig. 5. Bright-field TEM image from moderately thick region of a sample B. Circled region shows effect of irradiation by total electron dose of about 6.5 nC/nm². Compared to unaffected region of sample, shown at left of image, there is a slight bending of film and somewhat larger particles appearing in irradiated region.
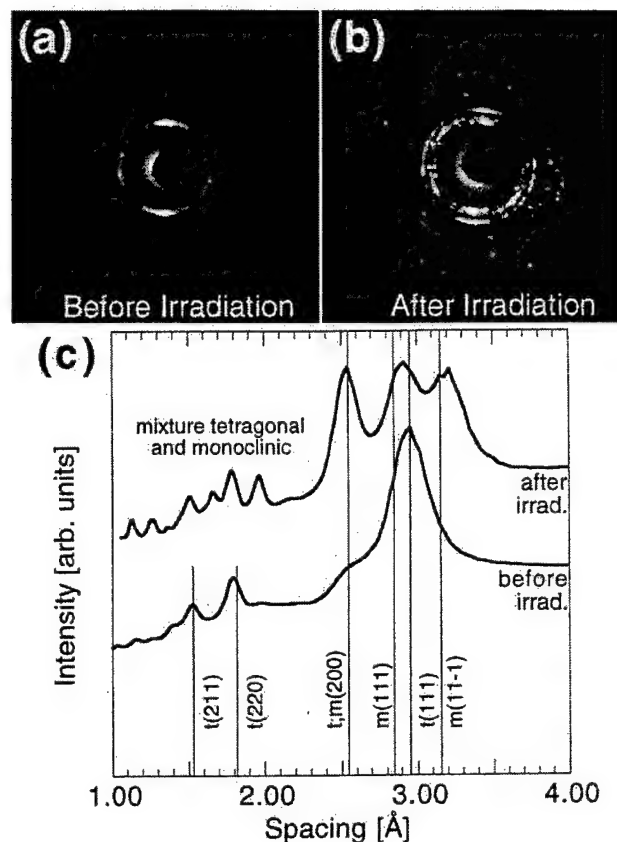

Fig. 6. SAD patterns taken (a) before and (b) after irradiation from circled region in Fig. 5. Rotational averages of SAD patterns are shown in c and are plotted vs. real space distances. Before pattern is indexed completely as tetragonal zirconia, while the after pattern consists of rings due to tetragonal zirconia, and spots due to diffraction from comparatively larger and fewer monoclinic zirconia crystallites. For sake of clarity, indexing of smaller spacings present in c for after pattern are not shown, but are due to mixture of many tetragonal and monoclinic zirconia spacings.

rial from the intervening alumina layers. In these cases, the zirconia re-crystallizes into larger sized monoclinic grains.

3.1.2. High-resolution imaging of individual crystallites

Experiments involving the high-resolution imaging of individual zirconia crystallites were performed with the goal of obtaining images before and after irradiation of a single zirconia nanocrystallite. After short exposures to the extreme irradiation conditions or long exposures to the moderate irradiation conditions; however, it was quite uncertain that the crystallite being imaged before the irradiation was indeed the same crystallite being imaged after the irradiation. The uncertainty arose due to comparatively large changes incurred by the sample in the region of the focused electron beam during irradiation.

Under these higher total dosage experiments, however, certain characteristic features were consistently produced within many zirconia crystallites in the irradiated region of the sample. These characteristic features are identified as a relative tilting of the lattice fringes, which prior to irradiation were oriented approximately parallel to the sub-
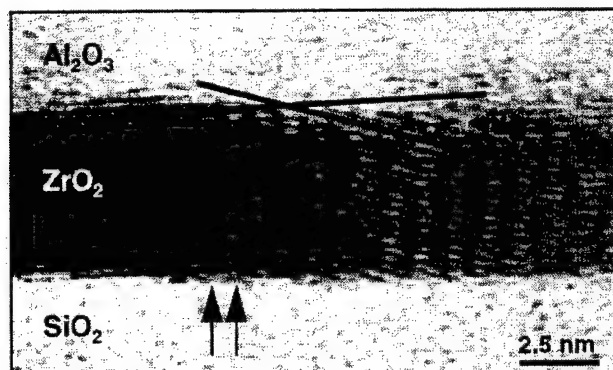
Fig. 7. HRTEM image showing typical features produced in some zirconia crystallites after exposure to extreme irradiation conditions. Characteristic features are tilting of lattice fringes by about 10° relative to substrate, and Moiré pattern shown in arrowed region of image.

strate, and the development of a Moiré fringe pattern imposed across the crystallite in the HRTEM images. Fig. 7 is an HRTEM image of one such crystallite showing the characteristic lattice fringe tilting and the Moiré pattern produced after extreme irradiation of the crystallite's vicinity. Phase identification of the crystallite imaged in Fig. 7 (from measurements of lattice spacings and interplanar angles) and of similar images obtained from other crystallites showing similar features to those shown in Fig. 7 indicate that these crystallites are neither truly tetragonal nor truly monoclinic. Within a single crystallite, some lattice spacings and interplanar angles match that of tetragonal

zirconia, while other spacings and angles match that of monoclinic zirconia. In many instances, lattice spacings and interplanar angles are obtained that are somewhere between the tabulated tetragonal and monoclinic values, as was reported previously for the as-grown nanolaminates [11].

In order to follow the development of an individual zirconia crystallite under the stresses produced by the electron beam irradiation, it is necessary to consider shorter exposures to the more moderate irradiation conditions. Experiments of this type were performed and are discussed next.

An HRTEM image of a selected as-grown zirconia crystallite was recorded using mild irradiation. The region containing the crystallite was irradiated under moderate conditions for a short time (10–20 s) and another HRTEM image was recorded of the same crystallite. The process of irradiating the sample and recording an HRTEM image was repeated to obtain a sequence of images. Lattice spacings and interplanar angles of the studied crystallite were measured from each HRTEM image in the series using numerical diffractograms [15–17].

Fig. 8a–c shows the first three images from such a sequence with 10 s of moderate irradiation of the crystallite between each image. The HRTEM images show a continuous change in the Moiré fringe pattern at the left edge of the images due to a small change in the lattice spacing of the crystallite. All of the changes observed in the zirconia layers and also the surrounding alumina layers during the entire sequence were of a continuous nature for this sequence and
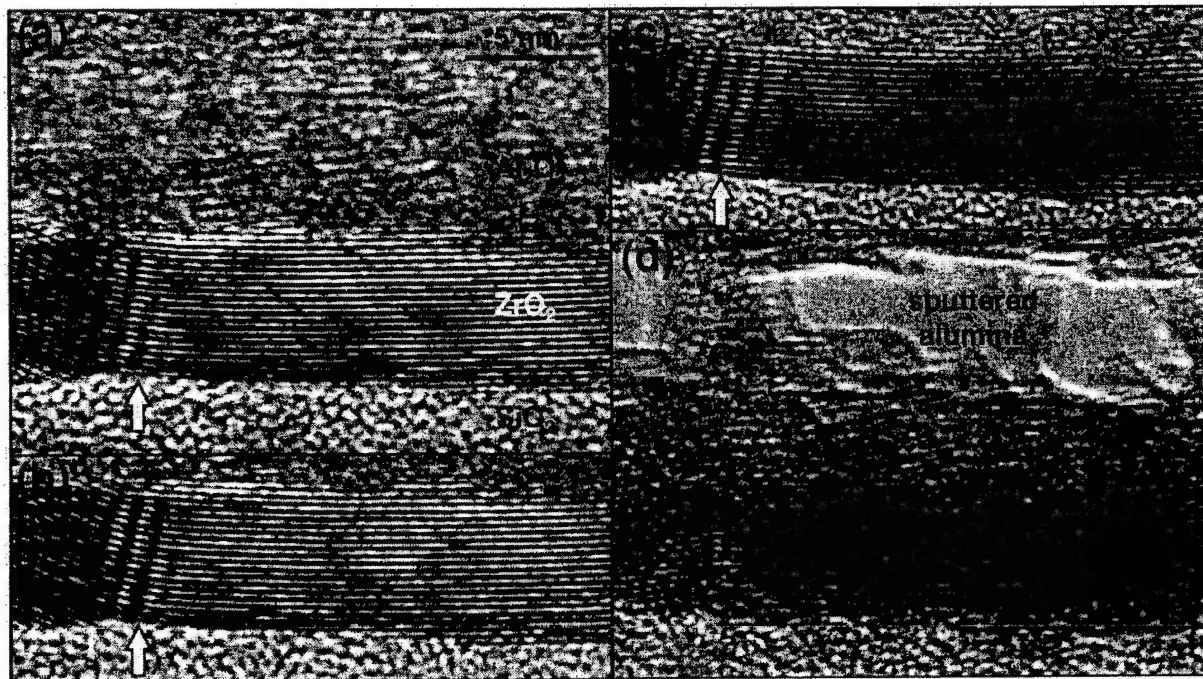

Fig. 8. Selected HRTEM images from irradiation sequence obtained from film C showing same region of zirconia layer throughout. Images a–c are first three images from sequence, and show development of Moiré fringe pattern in arrowed region. Image d is the last image from series after total electron dose of about 1.86 nC/nm² compared to a. Holes in alumina layer in d are due to sputtering of alumina by the 300 keV electron beam. Lattice spacing measurements for fringes shown at right of Moiré pattern (and for rest of series) are plotted as function of total electron dose in Fig. 9.

similar sequences recorded from different regions of the sample. Fig. 8d is the last image from the sequence and shows the same region as shown in Fig. 8a–c after a total electron dose of 1.86 nC/nm^2 from the initial image. Fig. 8d clearly shows holes in the alumina layer which were not present at the beginning of the sequence shown in Fig. 8a. Apart from the general decrease in the quality of the HRTEM images obtained, which is typical for these experiments, the changes in the crystal structure are too subtle to be evident in the image sequence without lattice spacing measurements.

Quantitative analysis of the lattice spacing shown in Fig. 8a–d and those in the complete image sequence show a small change in the spacing. Fig. 9 is a plot of the measured lattice spacing for the entire image sequence plotted as a function of total electron dose. For low total dosage the lattice spacing agrees well with the tabulated tetragonal (111) zirconia spacing [18]. With increasing total dosage there is a general increase in the lattice spacing toward the tabulated monoclinic (11-1) spacing [18]. The experimentally measured spacing in Fig. 9 towards the end of the irradiation sequence, however, is about 2–4% larger than the tabulated tetragonal (111) spacing and about 2–4% smaller than the monoclinic (11-1) [19]. This intermediate spacing was commonly observed in similar irradiation experiments, and also on occasion in some crystallites in the as-grown films [5].

Thermal expansion of the tetragonal zirconia crystallite due to electron beam heating is discounted as an explanation for the observed intermediate spacings. Even the most extreme estimates for the temperature change of the sample (~500 K) due to the irradiation conditions used would yield thermal expansion of less than 1%. Furthermore, the tabu-

lated tetragonal zirconia spacings, being used here to compare the experimentally observed lattice spacings, were obtained from X-ray diffraction from tetragonal zirconia samples at 1020°C [18]. Hence the thermal expansion of the zirconia was assumed to have a relatively minor affect on the lattice spacing measurements in these experiments. Additionally, in some of the HRTEM experiments a general decrease in the tetragonal (111) spacing towards the smaller monoclinic (111) spacing was observed which can not be attributed to thermal effects induced by electron beam heating.

The results presented above are typical for the HRTEM sequences obtained in additional similar experiments. The general features of the experiments are that the alumina layers develop holes concomitant with a distortion of the tetragonal zirconia crystallite lattice spacings and interplanar angles. The resultant crystallite phase is intermediate to the tetragonal and monoclinic phases. Although the alumina is significantly sputtered away in these experiments, enough of the alumina remains so that inter-layer re-crystallization of the zirconia does not occur. Under these conditions, the constraint provided by the alumina layers is relaxed, and it is reasonable to assume that the distortion of the tetragonal zirconia spacings towards monoclinic spacings is due to the crystallites having a size very near the critical size for spontaneous transformation to the monoclinic phase as predicted by thermodynamics calculations for an unconstrained zirconia crystallite. From Eq. (1) the critical size for spontaneous transformation at room temperature is 4.8 nm compared to the crystallite size of about 5 nm in these experiments.

Irradiation experiments involving high resolution imaging of individual zirconia crystallites were also performed with a nano-sized probe from a field emission source providing focused electron irradiation of an individual crystallite. In these experiments the irradiation flux was focused to a probe diameter of about 5 nm and only the zirconia crystallite was irradiated between acquisition of HRTEM images. In this way the loss of the surrounding alumina was practically eliminated and the effect of the electron beam irradiation on the zirconia crystallites was examined without the complications due to the sputtering of the alumina. Under a range of irradiation conditions, moderate to extreme, and exposure times from 30 s to 2 min, we did not observe transformation of the tetragonal zirconia crystallites to the monoclinic phase. Under extreme conditions, however, sputtering of the zirconia created a nano-sized hole in the irradiated region, accompanied by a detectable reduction of the zirconium oxide to zirconium metal in the sputtered region.

The examples discussed above clearly indicate the transformation behavior of the tetragonal zirconia in the zirconia–alumina nanolaminates is strongly dependent upon the laminar structure of the film. In cases where the alumina layers remain intact, the tetragonal phase is stable even under extreme electron fluxes and long exposure times. In
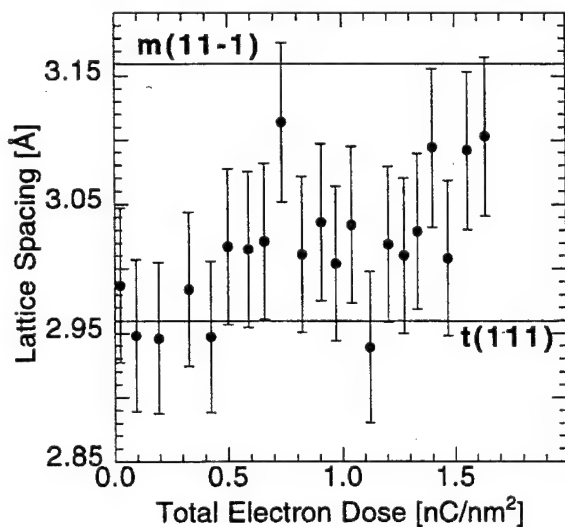

Fig. 9. Plot of measured spacings for lattice fringes oriented parallel to substrate in Fig. 8 for entire irradiation sequence. For low total electron dosage spacing agrees with tabulated tetragonal (111) zirconia spacing. For higher total electron dosage spacing is about 2–4% larger than tetragonal (111) spacing and about 2–4% smaller than tabulated monoclinic (11-1) spacing for zirconia.

cases where the alumina is significantly sputtered away by the electron beam, an intermediate tetragonal–monoclinic phase develops, or in extreme cases, the zirconia re-crystallizes in comparatively large monoclinic grains.

3.2. In-situ cooling

Experiments were performed on film B in which the sample was cooled in two stages, initially to a temperature of 133 K and ultimately to a temperature of 99 K. Four regions of the sample were identified where the sample thickness in the direction of the electron beam varied from very thin to very thick. Bright-field images and SAD patterns from all four regions were recorded before initiating the sample cooling, and also after reaching equilibrium at the 133 K and 99 K temperatures. Knock-on damage of alumina layers was minimized by using a 200 kV operating voltage under mild irradiation conditions, and by moving the sample away from the beam path during the cooling cycles. Shown in Fig. 10 are circular averages of the SAD patterns obtained from a moderately thick region of film B recorded at room temperature, 133 K and 99 K. All these patterns are indexed completely as tetragonal zirconia. Additional SAD patterns obtained from the other regions considered in this experiment show precisely the same results: the thermally-induced stresses produced in the nanolaminates by the in-situ cooling do not induce transformation in the tetragonal zirconia layers.

As discussed in Section 1, the predicted phase of a 5-nm sized zirconia particle at 99 K is the monoclinic phase (see Eq. (1) and Fig. 1). The thermodynamics calculations leading to the phase prediction illustrated in Fig. 1 are based on an unconstrained isolated zirconia crystallite as a model for the calculation. This model is appropriate in predicting the

critical zirconia layer thickness at which transformation occurs during growth. In the growth process the top-most alumina layer acts as a cap of the underlying zirconia layer and provides a substrate for the following zirconia layer. As such the alumina layer does not control the transformation because the growth occurs at the zirconia-vapor interface. However, in a completed zirconia–alumina multilayer which is subsequently exposed to stress during functioning, the individual zirconia crystallites are constrained both by neighboring zirconia crystallites within the zirconia layer as well as the alumina layers above and below the zirconia layers. These constraints override the thermodynamics predictions based on an unconstrained zirconia crystallite model.

The results presented here for the in-situ cooling experiments are consistent with the results presented for the electron beam irradiation experiments. In both cases the alumina layers play an important role in preserving the zirconia in the tetragonal phase.

4. Conclusions

The results of our study show that there is a substantial difference between the transformation behavior of dopant-stabilized microcrystals and that of undoped nanocrystals of tetragonal zirconia. In the former, the metastable tetragonal phase had been shown to transform to the monoclinic phase under application of stress, be it introduced by mechanical polishing, ion-bombardment, or electron beam irradiation. In contrast, no such transformation was observed under similar stress conditions in tetragonal zirconia nanocrystallites when the alumina layers were preserved. Therefore, the tetragonal zirconia nanocrystallites in zirconia–alumina nanolaminates are less likely to undergo transformation than the dopant-stabilized zirconia microcrystallites in zirconia–alumina composites.

Partial transformation to an intermediate phase was observed in our high resolution transmission electron microscopy studies of individual zirconia nanocrystallites in cases when the alumina constraint was reduced by partial sputtering of the alumina layers. Complete transformation was found in very thin areas of the samples, and also in intermediate thickness areas with higher irradiation doses when the alumina constraint was substantially removed. In these cases the transformation to the monoclinic phase was associated with enlargement of the zirconia nanocrystallites via re-crystallization between neighboring layers.

The thermodynamics calculations for the critical size for spontaneous transformation from the tetragonal to the monoclinic phase in zirconia predicts the phase composition of zirconia nanocrystallites occurring during growth of the multilayer films. The same calculations can be used to understand the partial transformation of the tetragonal crystallites to the monoclinic phase in the case where the alumina constraint is relaxed, as in the HRTEM experiments.
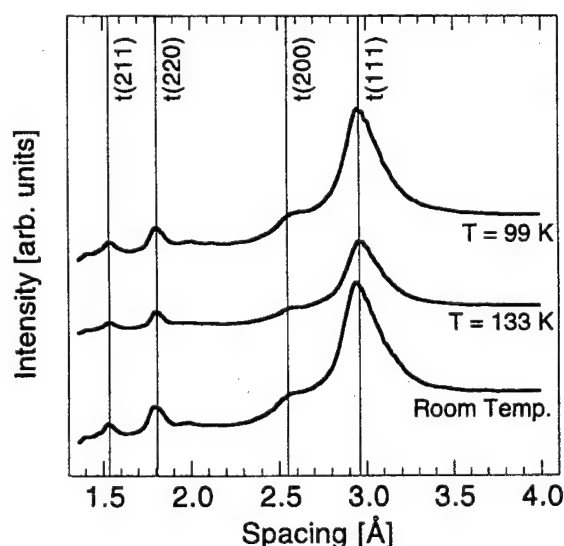

Fig. 10. Circular average of SAD patterns taken from a moderately thick region of sample B. Patterns were obtained at temperatures of 99 K, 133 K, and at room temperature. In each case patterns were indexed completely as tetragonal zirconia.

In the case of the cooling experiments, the thermodynamics arguments for an unconstrained crystallite do not apply because the intact alumina constraint aids in the preservation of.the tetragonal zirconia, i.e. it acts to fix the zirconia phase established during growth of the films. Removal of the alumina constraint then allows for the phase composition of the zirconia crystallites to be governed by the thermodynamic predictions for an isolated crystallite. This contention is further supported by the results of irradiation experiments where the alumina was removed from the sample by the electron beam to the point where zirconia re-crystallization could occur. In these situations the larger re-crystallized grains were monoclinic zirconia crystallites.

Acknowledgements

References

[1] C.R. Aita, U.S. Patent No. 5472795 (5 Dec 1995).
[2] C.M. Scanlan, M. Gajdardziska-Josifovska, C.R. Aita, Appl. Phys. Lett. 64 (1994) 3548.
[3] C.R. Aita, M.D. Wiggins, R. Whig, C.M. Scanlan, M. Gajdardziska-Josifovska, J. Appl. Phys. 79 (1996) 1176.
[4] R.C. Garvie, J. Phys. Chem. 69 (1965) 1239.
[5] M.A. Schofield, C.R. Aita, P.M. Rice, M. Gajdardziska-Josifovska, Thin Solid Films 326 (1998) 106.
[6] C.F. Grain, J. Am. Ceram. Soc. 50 (1967) 288.
[7] H.G. Scott, J. Mater. Sci. 10 (1975) 1527.
[8] V.S. Stubican, S.P. Ray, J. Am. Ceram. Soc. 60 (1977) 534.
[9] D.J. Green, R.H.J. Hannink, M.V. Swain, Transformation Toughening Ceramics, CRC, Boca Raton, FL, 1989.
[10] M.R. McCartney, M. Rühle, Acta Metall. 37 (7) (1989) 1859.
[11] M. Gajdardziska-Josifovska, C.R. Aita, J Appl. Phys. 79 (1996) 1315.
[12] W.J. de Ruijter, J.K. Weiss, Rev. Sci. Instr. 63 (10) (1992) 1.
[13] W.J. de Ruijter, Micron 26 (3) (1995) 247.
[14] D.J. Smith, J.C. Barry, in: P. Busek, J. Cowley, L. Eyring (Eds.), High-Resolution Electron Microscopy and Associated Techniques, Oxford University Press, New York, 1992, p. 507.
[15] W.J. de Ruijter, M. Gajdardziska-Josifovska, M.R. McCartney, R. Sharma, D.J. Smith, J.K. Weiss, Scanning Microsc. 6 (1992) 347.
[16] W.J. de Ruijter, J. Comput. Assist. Microsc. 6 (1994) 195.
[17] W.J. de Ruijter, R. Sharma, M.R. McCartney, D.J. Smith, Ultramicroscopy 57 (1995) 409.
[18] ASTM Joint Committee on Powder Diffraction Standards, 1974, File Nos. 13-307 and 17-923.
[19] M.A. Schofield, M. Gajdardziska-Josifovska, R. Whig, C.R. Aita, in: G.W. Bailey, J.M. Corbett, R.V.W. Dimlich, J.R. Michael, N.J. Zaluzec (Eds.), Proceedings of Microscopy and Microanalysis 1996, San Francisco Press, San Francisco, CA, 1996, p. 690.

REACTIVE SPUTTER DEPOSITION OF CERAMIC OXIDE NANOLAMINATES: ZrO_2–Al_2O_3 AND ZrO_2–Y_2O_3 MODEL SYSTEMS

C. R. Aita

The growth of ceramic nanolaminate films by reactive sputter deposition is reviewed. Phase formation in nanolaminates with the same nominal architecture but with different chemical constituents is investigated. Two model systems, zirconia–alumina and zirconia–yttria, allow comparison of the effects of chemical reactivity between constituents at the interface. In zirconia–alumina nanolaminates, each component is a separate entity and the interface is incoherent. Phase evolution in zirconia layers of decreasing thickness is predicted by the finite crystal size effect. Tetragonal zirconia is produced in layers whose thickness is less than the critical thickness for stabilisation of monoclinic zirconia (the STP phase). The amorphous structure of alumina is a consequence of its structural flexibility. Overall morphological roughness of the film arises from the polycrystalline nature of the zirconia layers. In zirconia–yttria nanolaminates, an interfacial reaction between components completely obliterates yttria as a separate entity. The reaction product, cubic zirconia–yttria, forms needlelike crystallites and accentuates the overall morphological roughness resulting from the polycrystalline nature of the deposit. As zirconia layer thickness increases, monoclinic zirconia is produced along with interfacial cubic zirconia–yttria. This research clearly demonstrates the ability to form interfacial oxide solid solutions at low temperature in a system in which the bulk equilibrium phase diagram predicts reaction between oxide components. Thus, thin films consisting entirely of interface reaction products can be fabricated if the bilayer spacing is small enough.

The author is in the Materials Department and the Laboratory for Surface Studies, University of Wisconsin–Milwaukee, PO Box 784, Milwaukee, WI 53201, USA.

INTRODUCTION

A nanostructured crystalline material is defined by Gleiter[1] as one in which spacings between lattice defects approach interatomic distances. Extending the term 'defect' to include a network of crystallite boundaries, nanomorphology gives rise to two important features: a large internal interfacial area, which has both physical and chemical consequences; and the possibility of stabilising unusual phases in nanocrystallites owing to the finite crystal size effect, i.e. a large surface energy contribution to the total Gibbs free energy of formation when the crystallite size is small. These features can be exploited to produce ceramics with unusual but useful behaviour.[2]

This paper addresses a specific type of nanostructured material, the ceramic nanolaminate coating. These materials are produced by the sequential deposition of ceramic layers. The resulting structure consists of different ceramics that are laminated together on a nanoscale. As the thickness of each component in the laminate decreases, the interface between components plays an increasingly important role in determining the overall properties of the coating. In turn, chemical reactivity between components may play an important role in determining the properties of the interface.
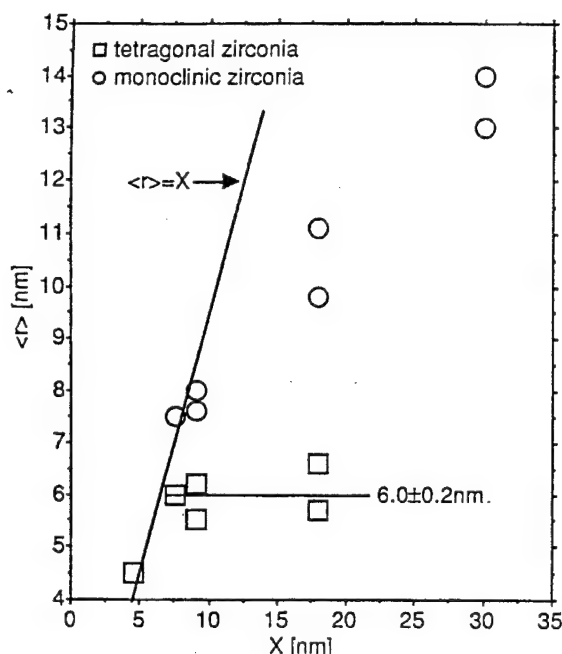
To illustrate this point, two binary oxide model systems that represent extremes in chemical reactivity between the constituents will be used. The model systems are zirconia–alumina and zirconia–yttria. The equilibrium phase diagram of zirconia and alumina shows a simple binary system in which the constituents have very limited mutual solid solubility and form no compounds.[3] On the other hand, the phase diagram of zirconia and yttria shows a series of solid solutions (alloys) covering the entire composition range from pure zirconia to pure yttria and, in addition, compounds are formed.[3–8]

In addition to being models for diversity in chemical reactivity, these two systems are technologically important by virtue of containing zirconia, the essential component of all functional bulk transformation toughening ceramics.[3] The thermodynamic phase evolution of bulk zirconia as it is cooled from the liquidus (2680°C at atmospheric pressure) is as follows: cubic (2360°C) → tetragonal (at around 1075°C) → monoclinic (STP phase). The protective behaviour of zirconia depends upon retention of the tetragonal phase at room temperature and the ability of this phase to transform locally to monoclinic in response to stress. The defect structure established within the daughter monoclinic phase and at the monoclinic/tetragonal phase boundary toughens the material.

With respect to the present author's work on thin films, the finite crystal size effect[9] (see below) has previously been used to design and produce tetragonal zirconia in zirconia–alumina nanolaminates simply by scaling the nanolaminate architecture.[10–12] Using high resolution transmission electron microscopy,[13] crystallographic changes that occur within the tetragonal zirconia layers in response to mechanical stress have been identified, and these atomic level changes have been related to the macroscopic phenomenon of transformation toughening.

This paper presents previously reported data for the growth of zirconia–alumina nanolaminates and new data for zirconia–yttria nanolaminates and then compares phase formation in the two systems, including metastable phase formation and interfacial

2 *Average tetragonal and monoclinic crystallite dimensions perpendicular to substrate* ($\langle r(t)\rangle$, $\langle r(m)\rangle$) *as function of zirconia layer thickness* X *for zirconia–alumina nanolaminates on fused silica*

Previously reported HREM of zirconia–alumina nanolaminates with $X = 4.5$ nm showed that zirconia crystallites have an approximately hemispherical shape with the diameter aligned along the substrate plane.[13] For a hemispherical crystallite

$$\Delta G = (2\pi/3)r^3\Delta g + 2\pi r^2 \Delta\gamma_{fv}$$

where $\Delta\gamma_{fv}$ is the change in surface energy of the film/vapour interface accompanying the transformation. At $\Delta G = 0$, the critical radius r_c for a spontaneous tetragonal to monoclinic growth transformation is $-3\Delta\gamma_{fv}/\Delta g$. Values for the energy terms are as follows

$$\Delta g = -2.85 \times 10^8(1 - T/1448)\ \mathrm{J\ m^{-3}}$$

where T is the growth temperature (in kelvin),[9] and[16]

$$\Delta\gamma_{fv} = \gamma_{fv}(m) - \gamma_{fv}(t) = (1.13 - 0.77) = 0.36\ \mathrm{J\ m^{-2}}$$

The expression for the critical radius (in nanometres) becomes

$$r_c = 3.79(1 - T/1448)^{-1} \qquad \ldots \ldots \ldots \quad (1)$$

Equation (1) is next applied to the experimental data. The zirconia crystallite size perpendicular to the substrate was determined from the Scherrer equation.[17] (It should be noted that the Scherrer equation gives the limiting case of broadening owing to size effects with no contribution from random lattice strain or a distribution of interplanar spacing owing to alloying, i.e. it is the minimum possible value of the average crystallite size.)

Figure 2 shows the average tetragonal ($\langle r(t)\rangle$) and monoclinic ($\langle r(m)\rangle$) crystallite dimensions perpendicular to the substrate as a function of X. Tetragonal and monoclinic phases have different $\langle r\rangle$ versus X behaviour: $\langle r(t)\rangle$ saturates at 6.0 ± 0.2 nm. The theoretical value obtained from equation (1) for the growth temperature ($T = 564$ K) is $r_c = 6.2$ nm. Based

on the excellent agreement between the experimental data and theoretical calculations, it can be concluded that nanolaminates with zirconia layer thickness less than r_c will contain zirconia solely in the tetragonal phase.

In contrast to tetragonal zirconia crystallite growth, Fig. 2 shows that $\langle r(m)\rangle$ increases linearly with zirconia layer thickness within the range $X = 7.5$–30 nm. Hence, $\langle r(m)\rangle$ is a linear function of the time t to grow a layer of thickness X, and $\mathrm{d}r\langle r(m)\rangle/\mathrm{d}t$ is constant. The Avrami equation[18] was therefore used to model the overall tetragonal to monoclinic zirconia growth transformation kinetics.[19] An Avrami exponent of 1.4 was obtained, consistent with a physical picture of the creation and subsequent growth of monoclinic crystallites from transformed tetragonal zirconia seeds of appreciable size.

With respect to orientation, monoclinic zirconia crystallites grow solely with $(11-1)$ planes parallel to the substrate and tetragonal zirconia crystallites grow solely with (111) planes parallel to the substrate in all films. These orientations represent closest packed planes aligned parallel to the substrate, and are expected to occur when there is weak adsorbate–substrate interaction compared to the interaction among adsorbed species.[20]
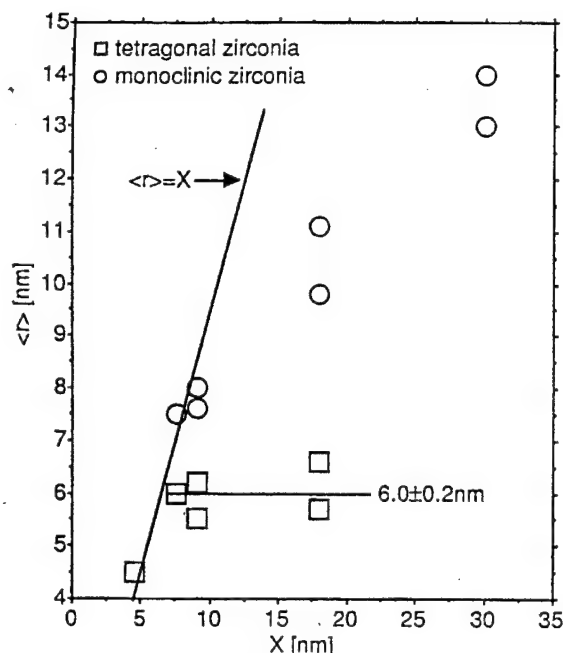
High resolution transmission electron microscopy of nanolaminates with type B architecture on an oxidised Si $\langle 111\rangle$ surface shows that the loss of layer integrity (roughening) is a result of the polycrystalline nature of zirconia, including renucleation as the zirconia layer thickness increases.[21] The HREM evidence of renucleation is consistent with Fig. 2, which shows that $\langle r(m)\rangle$ for thicker layers is less than the zirconia layer thickness.

Zirconia–yttria nanolaminates

X-ray diffraction data for nanolaminates with type A architecture grown on fused silica are shown in Fig. 3. The patterns in the range $2\Theta = 27$–$32°$ show a single peak (I) at low values of X and an additional peak (II) as X is increased. The interplanar spacings of these peaks were determined from high resolution scans (Fig. 4, for example, is a high resolution scan for $X = 4$ nm). Interplanar spacing for peaks I and II determined from the maximum peak intensity is shown in Fig. 5 as a function of X.

Peak I is identified with a series of cubic zirconia–yttria solid solutions with yttria mole fraction ranging from 0.26 to 0.81 (0.40 to 0.90 $YO_{1.5}$ mole fraction).[7] Specifically, peak I is assigned to the (111) planes of the fluorite structure for yttria mole fraction less than 0.48 (0.65 $YO_{1.5}$ mole fraction) and to the (222) planes of the bixbyite structure for yttria mole fraction greater than 0.48. The expected 2Θ range of these cubic peaks is shown in Fig. 4 and the resulting interplanar spacing is shown in Fig. 5. The positions of the (111) peak of tetragonal zirconia[22] and the (222) peak of cubic yttria[23] are also indicated on Figs. 4 and 5, to show why these assignments have been ruled out as primary causes of diffraction peak I. However, the large width of peak I (Fig. 4) precludes ruling out small contributions from tetragonal zirconia and cubic yttria.

Peak II is assigned to the $(11-1)$ planes of monoclinic zirconia.[24] A peak at $2\Theta = 49.1$–$49.4°$ (*see* Fig. 3) is assigned to the (220) or (440) planes

2 *Average tetragonal and monoclinic crystallite dimensions perpendicular to substrate ($\langle r(t) \rangle$, $\langle r(m) \rangle$) as function of zirconia layer thickness X for zirconia–alumina nanolaminates on fused silica*

Previously reported HREM of zirconia–alumina nanolaminates with $X = 4.5$ nm showed that zirconia crystallites have an approximately hemispherical shape with the diameter aligned along the substrate plane.[13] For a hemispherical crystallite

$$\Delta G = (2\pi/3)r^3 \Delta g + 2\pi r^2 \Delta \gamma_{fv}$$

where $\Delta \gamma_{fv}$ is the change in surface energy of the film/vapour interface accompanying the transformation. At $\Delta G = 0$, the critical radius r_c for a spontaneous tetragonal to monoclinic growth transformation is $-3\Delta \gamma_{fv}/\Delta g$. Values for the energy terms are as follows

$$\Delta g = -2.85 \times 10^8 (1 - T/1448) \text{ J m}^{-3}$$

where T is the growth temperature (in kelvin),[9] and[16]

$$\Delta \gamma_{fv} = \gamma_{fv}(m) - \gamma_{fv}(t) = (1.13 - 0.77) = 0.36 \text{ J m}^{-2}$$

The expression for the critical radius (in nanometres) becomes

$$r_c = 3.79(1 - T/1448)^{-1} \quad \ldots \ldots \ldots \quad (1)$$

Equation (1) is next applied to the experimental data. The zirconia crystallite size perpendicular to the substrate was determined from the Scherrer equation.[17] (It should be noted that the Scherrer equation gives the limiting case of broadening owing to size effects with no contribution from random lattice strain or a distribution of interplanar spacing owing to alloying, i.e. it is the minimum possible value of the average crystallite size.)

Figure 2 shows the average tetragonal ($\langle r(t) \rangle$) and monoclinic ($\langle r(m) \rangle$) crystallite dimensions perpendicular to the substrate as a function of X. Tetragonal and monoclinic phases have different $\langle r \rangle$ versus X behaviour: $\langle r(t) \rangle$ saturates at 6.0 ± 0.2 nm. The theoretical value obtained from equation (1) for the growth temperature ($T = 564$ K) is $r_c = 6.2$ nm. Based

on the excellent agreement between the experimental data and theoretical calculations, it can be concluded that nanolaminates with zirconia layer thickness less than r_c will contain zirconia solely in the tetragonal phase.

In contrast to tetragonal zirconia crystallite growth, Fig. 2 shows that $\langle r(m) \rangle$ increases linearly with zirconia layer thickness within the range $X = 7.5$–30 nm. Hence, $\langle r(m) \rangle$ is a linear function of the time t to grow a layer of thickness X, and $\text{d}r\langle r(m) \rangle/\text{d}t$ is constant. The Avrami equation[18] was therefore used to model the overall tetragonal to monoclinic zirconia growth transformation kinetics.[19] An Avrami exponent of 1.4 was obtained, consistent with a physical picture of the creation and subsequent growth of monoclinic crystallites from transformed tetragonal zirconia seeds of appreciable size.

With respect to orientation, monoclinic zirconia crystallites grow solely with $(11-1)$ planes parallel to the substrate and tetragonal zirconia crystallites grow solely with (111) planes parallel to the substrate in all films. These orientations represent closest packed planes aligned parallel to the substrate, and are expected to occur when there is weak adsorbate–substrate interaction compared to the interaction among adsorbed species.[20]
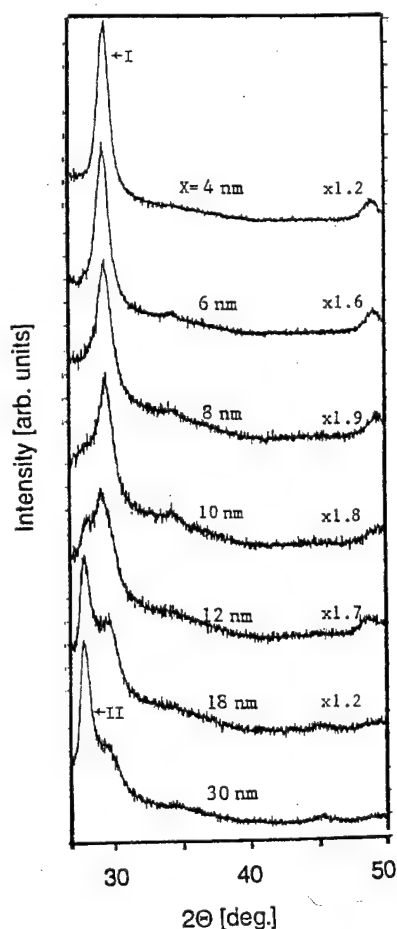
High resolution transmission electron microscopy of nanolaminates with type B architecture on an oxidised Si $\langle 111 \rangle$ surface shows that the loss of layer integrity (roughening) is a result of the polycrystalline nature of zirconia, including renucleation as the zirconia layer thickness increases.[21] The HREM evidence of renucleation is consistent with Fig. 2, which shows that $\langle r(m) \rangle$ for thicker layers is less than the zirconia layer thickness.

Zirconia–yttria nanolaminates

X-ray diffraction data for nanolaminates with type A architecture grown on fused silica are shown in Fig. 3. The patterns in the range $2\Theta = 27$–$32°$ show a single peak (I) at low values of X and an additional peak (II) as X is increased. The interplanar spacings of these peaks were determined from high resolution scans (Fig. 4, for example, is a high resolution scan for $X = 4$ nm). Interplanar spacing for peaks I and II determined from the maximum peak intensity is shown in Fig. 5 as a function of X.

Peak I is identified with a series of cubic zirconia–yttria solid solutions with yttria mole fraction ranging from 0.26 to 0.81 (0.40 to 0.90 $YO_{1.5}$ mole fraction).[7] Specifically, peak I is assigned to the (111) planes of the fluorite structure for yttria mole fraction less than 0.48 (0.65 $YO_{1.5}$ mole fraction) and to the (222) planes of the bixbyite structure for yttria mole fraction greater than 0.48. The expected 2Θ range of these cubic peaks is shown in Fig. 4 and the resulting interplanar spacing is shown in Fig. 5. The positions of the (111) peak of tetragonal zirconia[22] and the (222) peak of cubic yttria[23] are also indicated on Figs. 4 and 5, to show why these assignments have been ruled out as primary causes of diffraction peak I. However, the large width of peak I (Fig. 4) precludes ruling out small contributions from tetragonal zirconia and cubic yttria.

Peak II is assigned to the $(11-1)$ planes of monoclinic zirconia.[24] A peak at $2\Theta = 49.1$–$49.4°$ (*see* Fig. 3) is assigned to the (220) or (440) planes

3   X-ray diffraction patterns for zirconia–alumina nano-laminates on fused silica

of the abovementioned cubic zirconia–yttria alloy structures.[7]

Figure 6 shows the average cubic ($\langle r(c) \rangle$) and monoclinic ($\langle r(m) \rangle$) crystallite dimensions perpendicular to the substrate as a function of X. The most striking feature about these data is that $\langle r(c) \rangle$ is greater than the nominal zirconia layer thickness for $X = 4$–8 nm. (The Scherrer equation assumes that only a single value of interplanar spacing is responsible for peak broadening; the average value obtained from the diffraction peak maximum has been used in the calculation. Since the cubic phase most likely contains a range of interplanar spacings corresponding to a range of yttria concentrations, the values obtained here for $\langle r(c) \rangle$ are most likely smaller than the actual physical size of the crystallites.) The result that $\langle r(c) \rangle$ is greater than X is consistent with atomic mixing of zirconia and yttria in a single bilayer to
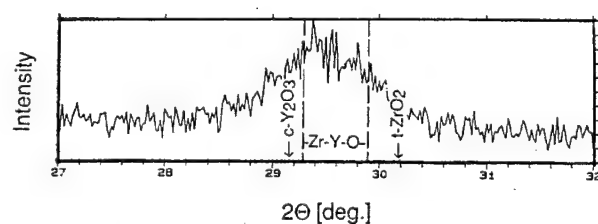
4   High resolution X-ray diffraction pattern for zirconia–yttria nanolaminate with 4 nm nominal zirconia and yttria layer thicknesses
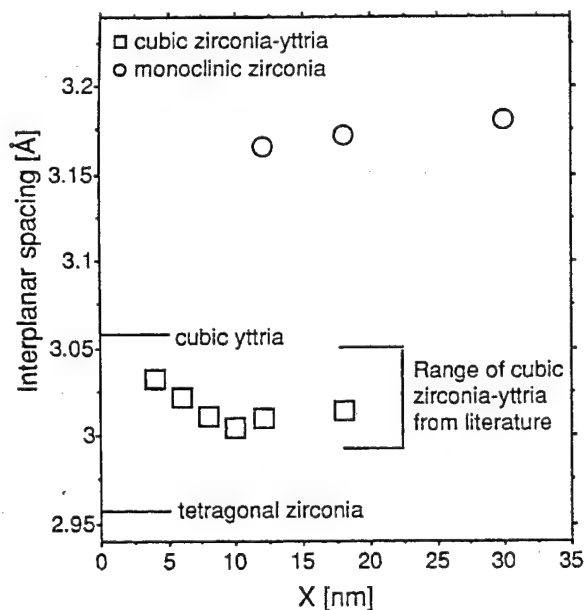

5   Interplanar spacing as function of nominal zirconia layer thickness X for zirconia–yttria nanolaminates on fused silica

form the alloys described above. It can therefore be concluded that these alloys are characteristic of the zirconia/yttria interface, even for nanolaminates with thick zirconia layers.

It can also be seen in Fig. 6 that $\langle r(m) \rangle$ is never smaller than about 9 nm, and increases with increasing X. This result is consistent with the result for zirconia–alumina nanolaminates, i.e. the monoclinic zirconia phase is not thermodynamically favoured in small crystallites.

With respect to crystallite orientation, monoclinic zirconia crystallites grow predominantly with $(11-1)$ planes parallel to the substrate and cubic zirconia
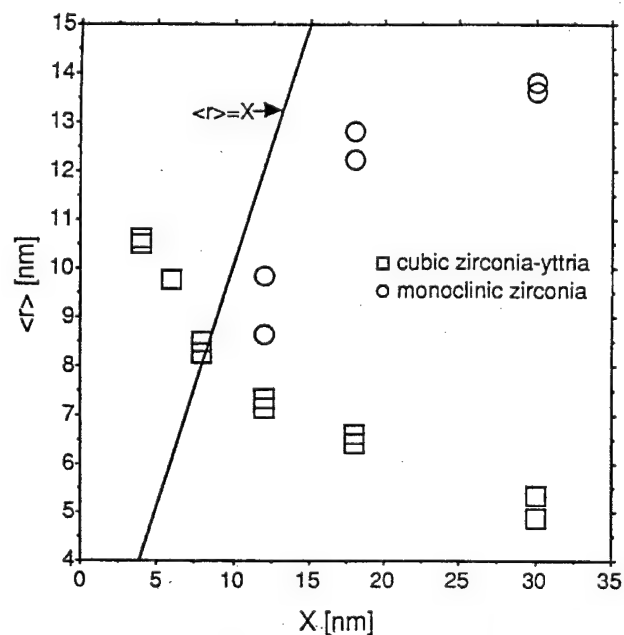
6   Average cubic and monoclinic crystallite dimensions perpendicular to substrate ($\langle r(c) \rangle$, $\langle r(m) \rangle$) as function of nominal zirconia layer thickness X for zirconia–yttria nanolaminates on fused silica

crystallites grow predominantly with (111) or (222) planes parallel to the substrate. As in the case of zirconia–alumina nanolaminates, these preferred orientations are the closest packing structures parallel to the substrate. However, unlike the case of zirconia–alumina, additional orientations in both the monoclinic zirconia and cubic zirconia–yttria alloy phases are present.

Transmission electron microscopy of nanolaminates with type B architecture on an oxidised Si $\langle 111 \rangle$ surface shows that the first zirconia layer ($X = 4$ nm) has a sharp interface with the substrate. However, the interface between this layer and the first yttria layer is virtually obliterated, as are all successive interfaces. Columnar crystallites extending tens of nanometres in the growth direction are the prevailing structures in the regions in which X is nominally between 4 and 8 nm. This morphology is qualitatively consistent with XRD measurements of cubic zirconia–yttria alloy crystallite size shown in Fig. 6. Furthermore, HREM lattice constant measurements on these extended crystallites are within the range of cubic zirconia–yttria alloy lattice constants[7] indicated in Figs. 4 and 5.

From these data, it is concluded that zirconia–yttria nanolaminate morphology is roughened by an interfacial chemical reaction between zirconia and yttria during deposition. In addition, physical roughening also occurs in thicker zirconia layers owing to their polycrystalline nature, as in the case of zirconia–alumina nanolaminates.

SUMMARY
Phase formation has been studied in ceramic nanolaminates with the same nominal architecture but with different chemical constituents. In particular, two model systems, zirconia–alumina and zirconia–yttria, have allowed comparison of the effects of chemical reactivity between constituents at their interface.

In zirconia–alumina nanolaminates, each ceramic component is a separate entity and the interface is incoherent. Phase evolution in zirconia layers of decreasing thickness is predicted by the finite crystal size effect. Namely, solely tetragonal zirconia is produced in layers whose thickness is less than the critical thickness for stabilisation of monoclinic zirconia (the STP phase). The amorphous structure of the alumina is a consequence of its structural flexibility.[25] Overall morphological roughness is a consequence of the polycrystalline nature of the zirconia.

In zirconia–yttria nanolaminates, an interfacial reaction between components has completely obliterated yttria as a separate entity. The reaction product, cubic zirconia–yttria, forms needlelike crystallites and accentuates the overall morphological roughness owing to the polycrystalline nature of the deposit. As zirconia layer thickness increases, monoclinic zirconia is produced along with interfacial cubic zirconia–yttria.

Understanding the mechanism for interfacial reactions between oxide overlayers during deposition is an important factor for producing tailored ceramic nanolaminates. Yet this area has received virtually no attention. Looking into the literature of related areas, hints may be discerned of what may prove to be important considerations. For example, studies of as deposited and post-deposition annealed intermetallic diffusion couple films show that phase formation is governed by the kinetics of the dominant migrating species rather than by thermodynamic driving forces.[26,27] In the case of the films grown here, diffusion may be assisted by athermal means, namely the low energy ion bombardment that is an integral part of sputter deposition.[28] (Ion implantation, however, is eliminated as being the chief method of delivery to the subsurface because no evidence of implantation damage[29] is found in the zirconia–alumina system.) In addition, compositional inhomogeneity at or near the growth interface may cause elastic stress that affects diffusion.[30]

These considerations have only to be applied to the zirconia–yttria system to see the complexity of the problem at hand. For example, consider compound formation at the interface in the first bilayer adjacent to the substrate. Gaseous Y, YO,[31,32] and oxygen (many forms[33]) species arrive at the solid zirconia overlayer and are adsorbed. They must undergo surface and subsurface diffusion to arrive at a reaction site. The location of the site and the manner by which adsorbed species migrate to it are unknown and must be determined. Producing a quantitative model from this elementary starting point remains the subject of future research.

In closing, it is emphasised that this research demonstrates the ability to form interfacial oxide solid solutions at low temperature in a system in which the bulk equilibrium phase diagram predicts reaction between oxide components. Thin films consisting entirely of interface reaction products can be fabricated if the bilayer spacing is small enough.

REFERENCES
1. H. GLEITER: *Nanostructured Mater.*, 1992, **1**, 1–19.
2. H. HAHN: *Nanostructured Mater.*, 1993, **2**, 251–265.
3. D. J. GREEN, R. H. J. HANNINK, and M. V. SWAIN: 'Transformation toughening of ceramics'; 1989, Boca Raton, FL, CRC Press.
4. R. RUH, K. S. MAZDIYASNI, P. G. VALENTINE, and H. O. BIELSTEIN: *J. Am. Ceram. Soc.*, 1984, **67**, C190–C192.
5. M. H. TUILIER, J. DEXPERT-GHYS, H. DEXPERT, and P. LAGARDE: *J. Solid State Chem.*, 1987, **69**, C153–C161.
6. C. PASCAUL and P. DURAN: *J. Am. Ceram. Soc.*, 1982, **66**, 23–27.
7. H. G. SCOTT: *J. Mater. Sci.*, 1977, **12**, 311–316.
8. H. G. SCOTT: *Acta Crystallogr. B*, 1977, **33**, 281–282.
9. R. C. GARVIE and M. V. SWAIN: *J. Mater. Sci.*, 1985, **20**, 1193–1200.
10. C. R. AITA: US Patent 5472795, 1995.
11. C. M. SCANLAN, M. GAJDARDZISKA-JOSIFOVSKA, and C. R. AITA: *Appl. Phys. Lett.*, 1994, **64**, 3548–3550.
12. C. R. AITA, M. D. WIGGINS, R. WHIG, C. M. SCANLAN, and M. GAJDARDZISKA-JOSIFOVSKA: *J. Appl. Phys.*, 1996, **79**, 1176–1178.
13. M. GAJDARDZISKA-JOSIFOVSKA and C. R. AITA: *J. Appl. Phys.*, 1996, **79**, 1315–1319.
14. C. R. AITA: *J. Vac. Sci. Technol. A*, 1993, **11**, 1540–1547.
15. R. C. GARVIE and P. S. NICHOLSON: *J. Am. Ceram. Soc.*, 1972, **55**, 303–305.

16. R. C. GARVIE: *J. Phys. Chem.*, 1965, **69**, 1239–1243.
17. L. V. AZAROFF: 'Elements of X-ray crystallography'; 1968, New York, NY, McGraw-Hill.
18. J. W. CHRISTIAN: 'The theory of transformations in metals and alloys'; 1975, Oxford, Pergamon.
19. C. R. AITA: in 'Processing and fabrication of advanced materials V', (ed. T. S. Srivatsan and J. J. Moore), 459–468; 1997, Warrendale, PA, TMS.
20. E. BAUER: in 'Single crystal films', (ed. M. H. Francombe and H. Sato); 1964, New York, NY, Macmillan.
21. M. A. SCHOFIELD, M. GAJDARDZISKA-JOSIFOVSKA, C. R. AITA, and P. M. RICE: to be published.
22. ASTM Joint Commission on Powder Diffraction Standards, File 17–923.
23. ASTM Joint Commission on Powder Diffraction Standards, File 05–574.
24. ASTM Joint Commission on Powder Diffraction Standards, File 13–307.
25. F. F. FELNER: 'Low temperature oxidation'; 1981, New York, NY, Wiley-Interscience.
26. A. S. EDELSTEIN, R. K. EVERETT, G. Y. RICHARDSON, S. B. QADRI, E. I. ALTMAN, J. C. FOLEY, and J. J. PEREPEZKO: *J. Appl. Phys.*, 1994, **76**, 7850–7859.
27. K. BARMAK, C. MICHAELSEN, and G. LUCADAMO: *J. Mater. Res.*, 1997, **12**, 133–146.
28. C. R. AITA: *J. Vac. Sci. Technol. A*, 1985, **3**, 625–630.
29. N. HERBOTS, O. C. HELLMAN, P. YEH, Z. WANG, and O. VAN CAUWENBERGHE: in 'Low energy surface interactions'; 1993, Cambridge, Wiley.
30. W. C. JOHNSON and G. MARTIN: *J. Appl. Phys.*, 1990, **68**, 1252–1264.
31. C.-K. KWOK and C. R. AITA: *J. Vac. Sci. Technol. A*, 1990, **8**, 1330–1334.
32. C.-K. KWOK, C. R. AITA, and E. KOLAWA: *J. Appl. Phys.* 1990, **68**, 2945–2951.
33. C. R. AITA and M. E. MARHIC: *Vacuum*, 1988, **38**, 37–38.

Thickness-dependent crystallinity of sputter-deposited titania

J. D. DeLoach[a)] and C. R. Aita

Department of Electrical Engineering and Computer Science, Department of Materials, and Laboratory for Surface Studies, University of Wisconsin-Milwaukee, P.O. Box 784, Milwaukee, Wisconsin 53201

In this study, we sputter deposited titania films of thickness ranging from 256 to 705 nm on unheated substrates and studied changes in phase constituency as a function of film thickness. X-ray diffraction, and infrared spectroscopy were used for post-deposition analysis. The results show that the thinnest films consisted of anatase, rutile, and an amorphous structure. As film thickness increased, anatase formed at the expense of the amorphous constituent, whereas the amount of rutile per unit film volume remained constant. We hypothesized that if the thickness-related crystallographic changes were caused by bulk annealing effects due to *in situ* plasma heating during deposition, then it should be possible to reproduce these changes, *ex situ*, by furnace annealing. The thinnest films were annealed at three temperatures: 300, 500, and 700 °C. There was no change in phase composition at 300 °C. Metallurgical recovery of both crystalline phases occurred at 500 °C. At 700 °C, rutile grew at the expense of anatase, which completely disappeared. The results showed that post-deposition annealing caused crystallographic changes that were inconsistent with the thickness-dependent crystallographic changes in the as-grown films. We suggested that the latter was caused by enhanced surface, not bulk diffusion, possibly due to an increase in substrate temperature during deposition. © *1998 American Vacuum Society.* [S0734-2101(98)53903-6]

I. INTRODUCTION

Bulk titania (TiO_2) exists in three polymorphic phases at atmospheric pressure, rutile, anatase, and brookite.[1–3] Titanium is in octahedral coordination with oxygen as TiO_6 units in all polymorphs, but in different arrangements, giving rise to differences in physical and chemical properties. It is precisely this structural flexibility that allows an amorphous structure to form so readily in titania thin films.[4] Rutile is the stable phase at all temperatures. Below ~800 °C, anatase and brookite (which requires alkali dopants to form) exist as metastable phases.

Thin film titania has technologically important electrical and optical properties. For example, there is current interest in titania as a chemically stable, high dielectric constant capacitor material for dynamic random access memory devices,[5,6] as a transparent high refractive index material for use in single-layer films, and as a component of both reflective and antireflective multilayers.[7–13]

The literature shows that reactive sputter deposition is a viable method for producing titania.[4,5,14–26] However, it is widely acknowledged that an important issue for film reproducibility is to understand how film structure is related to deposition parameters. Therefore, much of the literature deals with specific elements of this issue.

In the present work, we examine the dependence of phase formation on film thickness. The experimental program included x-ray diffraction for phase determination and infrared spectroscopy for Ti–O bonding information. Since differences in crystallinity were observed in films of different thickness, we tested the hypothesis that *in situ* plasma heating during deposition caused annealing of the film volume.

Ex situ post-deposition annealing was carried out in an attempt to simulate *in situ* effects. The results are discussed in terms of surface and bulk diffusion as the controlling factor for thickness-dependent crystallization.

II. EXPERIMENT

Film Growth: Titania films were grown in a diffusion-pumped, planar diode, radio frequency-excited sputtering system. The target was a 13 cm diameter, 99.995% pure Ti disc bonded to a Cu backing plate that was attached to the cathode. Substrates were placed on a Cu pallet covering the anode. The pallet was unheated, although a temperature rise due to plasma heating is expected.[27] The cathode-to-anode spacing was 9 cm. The chamber was evacuated to a base pressure of $<7 \times 10^{-7}$ Torr and backfilled with 1 $\times 10^{-2}$ Torr O_2 at a flow rate of 10 sccm. A plasma was established at a voltage of -1.2 ± 0.1 kV (peak-to-peak) corresponding to 300 W forward power. The target was presputtered for 15 min before the movable shutter which covered the substrates was opened and a film was deposited.

Fused silica, high resistivity infrared-transparent $\langle 111 \rangle$ Si, and low resistivity $\langle 111 \rangle$ Si substrates were used. A portion of the low resistivity $\langle 111 \rangle$ Si substrate was masked to produce a step for post-deposition thickness measurement using profilometry. The film thickness and growth rate, determined by dividing thickness by deposition time, are recorded in Table I.

Film Characterization: Films on fused silica substrates were studied by double-angle x-ray diffraction (XRD) using 0.15418 nm unresolved Cu $K\alpha$ radiation. The machine was calibrated using an unstressed Si standard with a {111} peak at 28.44 ± 0.01 and a half width of 0.2°. Data was acquired over the $2\theta = 20°-70°$ range because reference diffraction

TABLE I. Thickness and growth rate of titania films.

Film	Growth time (min)	Thickness (nm)	Growth rate (nm/min)
A	135	256	1.9
B	270	506±67	1.9±0.3
C	360	705±30	1.9±0.2

patterns[28–30] for the titania polymorphs show that all first order peaks occur within this interval. Peak position (2θ), maximum intensity, and full width at half maximum intensity (FWHM) were measured from high-resolution scans of individual peaks. Phase identification and preferred orientation were determined from these data.

The integrated intensity, e.g., the area under an individual XRD peak, was determined from the product of the maximum intensity and FWHM. The integrated intensity, not maximum intensity, is proportional to the number of crystallographic planes of a particular phase and orientation. FWHM is a convolution of machine and materials parameters. A real crystal, especially one in a thin film grown at low temperature, has random lattice strain and finite size. In the following text, we will use FWHM as an indicator of crystallite "perfection," e.g., an infinitely large, unstrained crystal is perfect. The broader the FWHM, the more imperfect the crystallite. (Uniform strain for both the as-deposited and annealed samples was very small, therefore, it was neglected.)

Fast-Fourier transform infrared spectroscopy (FTIR) in transmission mode over the 400–1000 cm^{-1} range was used to determine the vibrational spectra of films grown on IR-transparent Si. These data allow comparison of short-range Ti–O bonding in films of different thickness.

Annealing: Isothermal cyclic annealing was carried out on films grown for 135 min on fused silica (film A). Films were annealed for sequential times of 0.5, 1, 2, 4, 8, and 24 h at 300 and 500 °C and cooled in air. In addition, films were annealed for two 0.5 h intervals at 700 °C.

III. AS-DEPOSITED FILMS

Figure 1 shows XRD spectra of films of each thickness. The rise in the background at low angle is due to diffraction from the nanocrystalline fused silica substrate. For reference, line charts of the standard powder peak position and intensity for anatase and rutile are included in this figure. Table II records the peak position, assignment, maximum intensity, and width of the major diffraction peaks shown in Fig. 1.

The spectra shown in Fig. 1 have the following common features: (a) both rutile and anatase phases are present; (b) the dominant phase is anatase, with a strong reflection from {101} planes, however other anatase orientations are present; (c) rutile is present with a reflection solely from {110} planes; (d) in all cases, the peaks are broad, indicating small crystallite size and/or random lattice strain and of low intensity, suggesting that amorphous titania coexists along with the crystalline phases.
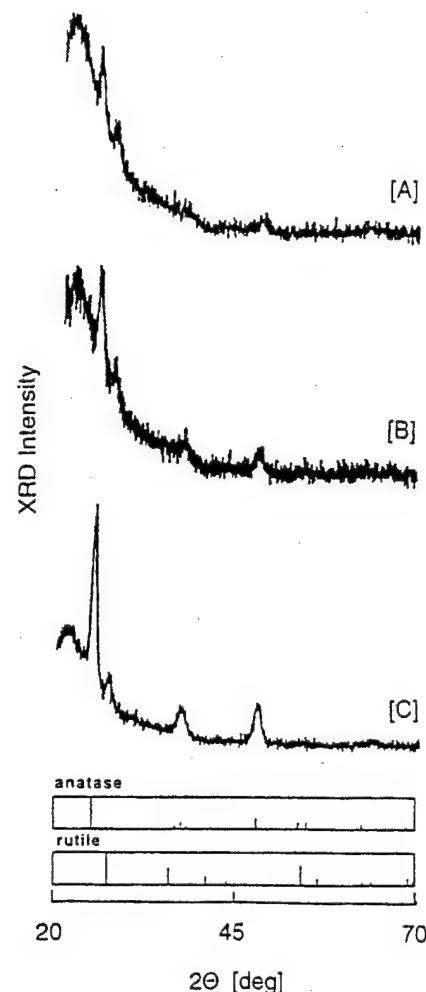
FIG. 1. XRD spectra of titania films of each thickness (film A, 256 nm; film B, 506 nm; film C, 705 nm). Line spectra of bulk anatase and rutile phases are also shown (Refs. 28 and 29).

To determine whether anatase has grown with a preferred orientation, e.g., a single set of planes preferentially oriented parallel to the substrate (crystallographic texture), we compared the relative intensities of different anatase planes within each film to those of a powder standard.[28] The data, recorded in Table III, show that anatase has a {101} preferred orientation in all films.

The amount of rutile relative to anatase in each film, estimated from the ratio of the rutile {110} integrated intensity to the sum of the integrated intensity of all anatase peaks is

TABLE II. Crystallographic parameters for the major diffraction peaks of titania films on fused silica.

Film	2θ (deg)	Assignment[a]	Intensity (cps)	FWHM (deg)
A	25.18±0.06	a {101}	187±38	0.71±0.08
	27.38±0.11	r {110}	108±15	0.86±0.06
B	25.11±0.06	a {101}	254±13	0.82±0.02
	27.32±0.05	r {110}	103±19	0.92±0.16
C	25.22±0.03	a {101}	986±4	0.75±0.02
	27.40±0.06	r {110}	134±3	1.03±0.37

[a]a = anatase, r = rutile.

TABLE III. Relative intensity of anatase reflections in as-grown titania films of different thickness.

Film	Thickness (nm)	Intensity (101)/(200)/(004)
A	256	$100/22.7 \pm 1.0/18.34 \pm 1.1$
B	506	$100/24.5 \pm 0.6/14.7 \pm 0.2$
C	705	$100/24.9 \pm 2.0/19.4 \pm 6.01$
ASTM standard (Ref. 28)		100/33/22

shown as a function of film thickness in Fig. 2(a). It can be seen that the amount of rutile relative to anatase decreases with increasing film thickness. The question of whether anatase grows at the expense of rutile or at the expense of an amorphous structure such that there is overall increase in crystallinity with increasing film thickness is addressed next.

A correction[31] for differences in x-ray absorption was applied to the data in order to compare phase composition in films of different thickness (Appendix). Figure 2(b) shows the maximum intensity and integrated intensity of the rutile {110} and anatase {101} reflections relative to the anatase {101} reflection in film A as a function of film thickness. It can be seen that both the maximum and integrated intensity of the rutile {110} reflection remain constant within experimental error whereas these quantities increase for the anatase {101} reflection as the film thickness increases. The FWHM remains broad and unchanged for these reflections as film thickness increases (Table II). Therefore, these data show that the amount of anatase per unit film volume increases
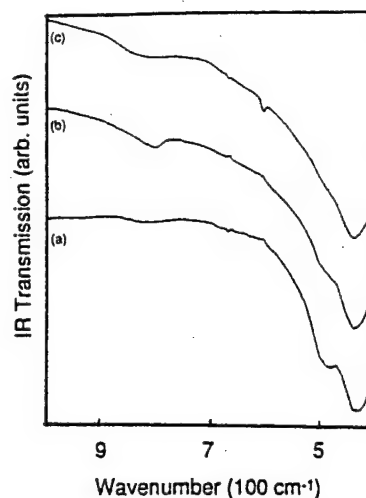
FIG. 3. FTIR transmission spectra of films of different thickness as a function of wave number.

with increasing film thickness, but that the anatase crystallite perfection does not increase. Furthermore, anatase forms at the expense of the amorphous phase, since the amount of rutile per unit film volume remains constant.

Figure 3 shows the FTIR transmission spectra as a function of wavenumber. All spectra show a minimum in intensity at 439 ± 2 cm^{-1}. This minimum is featureless in film C. However, a shoulder develops at 493 ± 9 cm^{-1} as the film thickness decreases.

A comparison of the literature for bulk[32] and thin film titania[33-36] shows that, to date, the polymorphs have not been distinguished in film samples on the basis of FTIR data. This is a consequence of the similar nearest-neighbor coordination in the polymorphs, combined with FTIR peak broadening due to crystallite imperfection characteristics of thin films. However, it can be seen from Fig. 3 that the amorphous component in our films is "fingerprinted" by the presence of a developing shoulder on the transmission minimum.

IV. ANNEALED FILMS

Annealing film A at 300 °C produces no change in maximum or integrated intensity of XRD reflections from either phase, and therefore these data are not shown here. Figure 4 shows the maximum intensity, FWHM, and integrated intensity of the anatase {101}, and rutile {110} peaks as a function of cumulative annealing time at 500 °C. There is an approximately two-fold increase in the maximum intensity in both phases after 0.5 h at temperature. Additional time at 500 °C does not produce a further change in the maximum intensity for the rutile {110} reflection. However, the maximum intensity for the anatase {101} reflection continues to increase for 8 h cumulative time and then saturates. The FWHM of both anatase {101} and rutile {110} peaks decreases after a 0.5 h anneal. The integrated intensity is unchanged by annealing (for comparison's sake shown on the same scale as the maximum intensity). Since the integrated intensity is the product of the maximum intensity and FWHM, the physical interpretation of the data in Fig. 4 is that the number of crystallo-
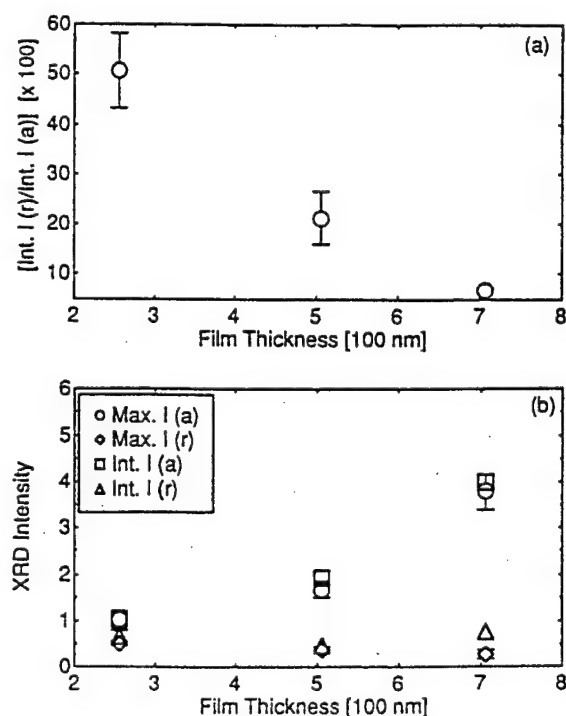

FIG. 2. (a) Ratio of the rutile {110} XRD integrated intensity to the sum of integrated intensity of all anatase reflections as a function of film thickness. (b) Corrected maximum and integrated XRD intensity of rutile {110} and anatase {101} reflections relative to the anatase {101} reflection in film A as a function of film thickness.
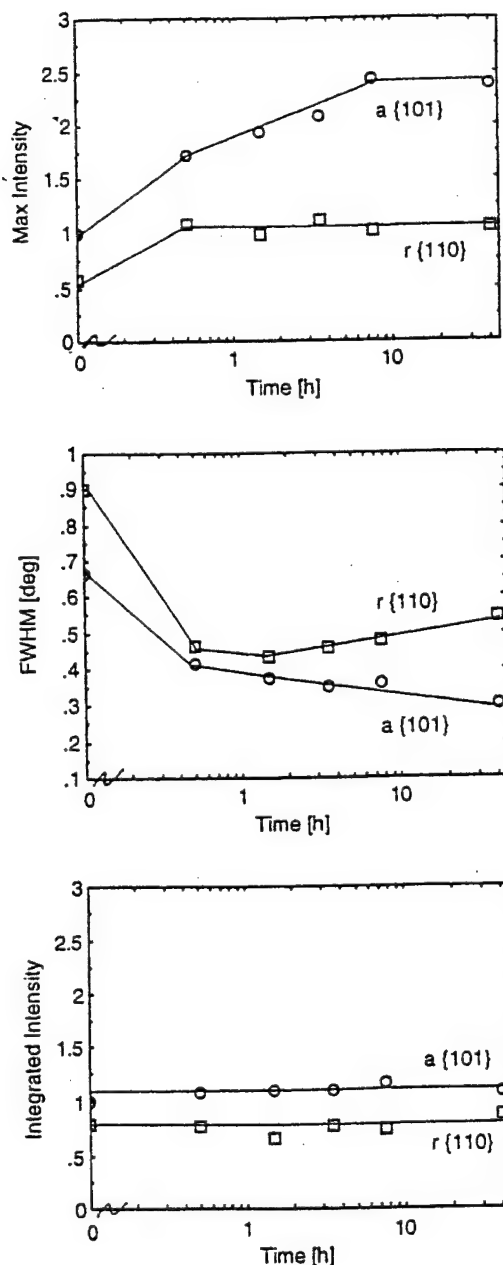
FIG. 4. Maximum intensity, FWHM, and integrated intensity of the anatase {101} and rutile {110} XRD reflections relative to the value of the anatase {101} reflection in as-grown film A as a function of cumulative annealing time at 500 °C.

FIG. 5. XRD spectra of titania film A upon annealing at 700 °C. Crystallographic parameters are: 0 h—a\{101\} at 25.26°, 174 cps; r\{110\} at 27.53°, 116 cps; 0.5 h- a\{101\} at 25.35°, 375 cps; r\{110\} at 27.42°, 1147 cps; 1 h- r\{110\} at 27.41°, 1606 cps.

graphic planes of either phase does not increase with annealing at 500 °C, but that crystallites of both phases become less imperfect.·

This behavior is analogous to metallurgical recovery; i.e., annealing at less than one-third of the melting temperature (1850 °C for TiO$_2$) causes point defect movement to crystallite boundaries and sufficient dislocation motion to annihilate low angle crystallite boundaries. However, the large angle crystallite boundary motion necessary for crystallite growth by diffusional processes does not occur.

Figure 5 shows high-resolution XRD spectra for the anatase {101} and rutile {110} reflections in film A annealed at 700 °C for cumulative time 0, 0.5, and 1 h. Figure 6 shows
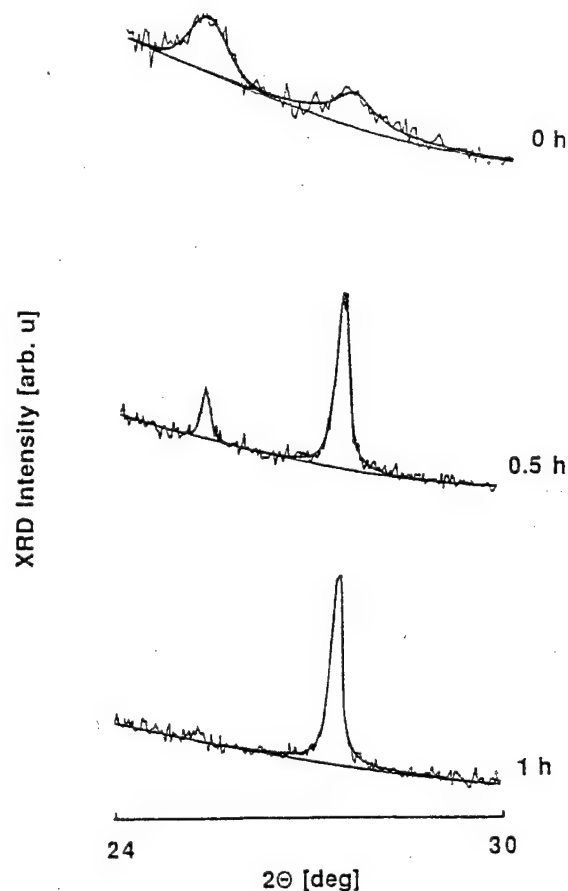
the maximum and integrated intensity for the anatase {101} and rutile {110} reflections as a function of cumulative annealing time. In contrast to the lower temperature anneals, both the maximum and integrated intensity for the anatase {101} reflection increase after 0.5 h at 700 °C, while for the rutile {110} reflection, the maximum intensity increases but the integrated intensity decreases. Considering the narrow FWHM of these peaks, shown in Fig. 5, we conclude that both anatase {101} and rutile {110} crystallites become more perfect after a 0.5 h anneal. However, there is an increase in the amount of rutile and a decrease in the amount of anatase. After a 1 h anneal, anatase has entirely disappeared from the film, and the amount and perfection of rutile crystallites has continued to increase. The anatase-to-rutile transformation in these films occurs at a temperature approximately 100 °C lower than in bulk titania.

V. THICKNESS-DEPENDENT VERSUS POST-DEPOSITION ANNEALING CRYSTALLOGRAPHIC CHANGES

The results in Sec. III show that the thickness-dependent crystallization of as-grown films is earmarked by the following behavior. As the film thickness increases, there is; (a) an increase in the amount of anatase per unit volume at the
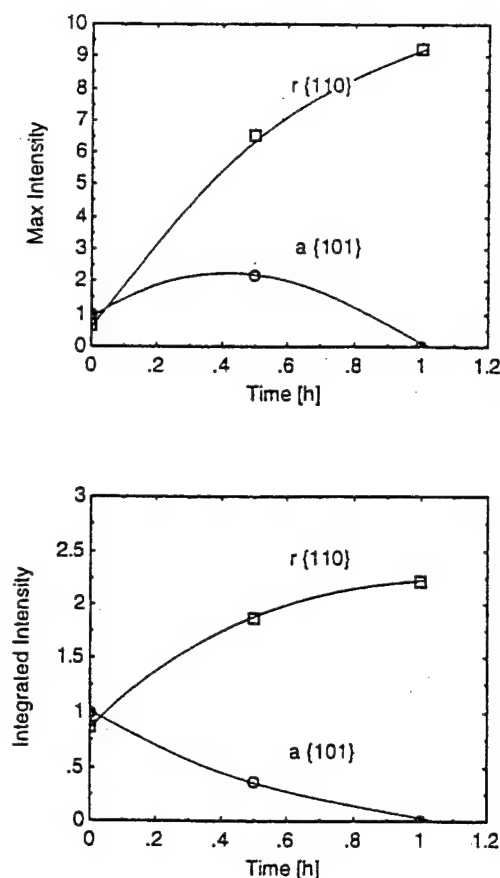
FIG. 6. Maximum and integrated intensity of anatase {101} and rutile {110} XRD reflection relative to the value of the anatase {101} reflection in as-grown film A as a function of cumulative annealing time at 700 °C.

expense of the amorphous phase, but no improvement in anatase crystallite perfection, and (b) the amount of rutile per unit volume and rutile crystallite perfection is unchanged. This marked bimodal behavior of anatase and rutile phases is not characteristic of recovery associated with low temperature post-deposition annealing (Fig. 4). Neither is this behavior characteristic of moderate temperature post-deposition annealing (Figs. 5 and 6) which results in rutile production and anatase elimination. We therefore conclude that *in situ* processes involving bulk diffusion through the film volume are not the primary cause of thickness-dependent crystallization, but that this phenomenon is controlled by surface diffusion of adsorbed species at the growth interface.

The literature shows that crystallization in thin film titania is very sensitive to slight variations of substrate temperature. For example, a transition from amorphous to anatase growth was reported for temperature $\leqslant 300$ °C. [14,37] On this basis, we suggest that the thickness-dependent amorphous-to-anatase crystallization observed here is concurrent with an increase in temperature at the film growth interface as the deposition proceeds.

There are several possible reasons for a temperature increase at the growth interface to occur. First, the black body temperature of the target may increase with increasing sputtering time, and this radiation heats the growth interface. Second, the film becomes more insulating as its thickness

increases, and the heat flow from the growth interface through the film to the Cu pallet is diminished. We will address detailed characterization of the growth environment in future work.

ACKNOWLEDGMENTS

APPENDIX

A correction factor that takes into account beam absorption as a function of path length, $x/\sin\theta$, and is given by the expression:[31]

$$G_x = [1 - \exp(-2\mu x/\sin\theta)], \tag{1}$$

where G_x is the fraction of the total diffracted intensity contributed by a surface layer of depth x (e.g., the film thickness), μ is the atomic scattering factor, and θ is the diffraction angle for a particular set of $\{hkl\}$ planes. In terms of tabulated[38] parameters for μ/ρ and ρ, where ρ is the density, Eq. (1) becomes

$$G_x = \{1 - \exp[-2(\mu/\rho)\rho x/\sin\theta]\}. \tag{2}$$

For titania, $\mu/\rho(TiO_2) = \mu/\rho(Ti) + 2\mu/\rho(O)$. Substituting values for $\mu/\rho(Ti) = 208$ cm^2/g and $\mu/\rho(O) = 11.5$ cm^2/g for the XRD conditions used here, and the appropriate values of ρ for rutile and anatase,[1] we obtain G_x for diffraction peak of each phase at a particular film thickness. Raw peak intensity data were divided by G_x to obtain a value for intensity independent of film thickness, i.e., for a film of infinite thickness.

[1]S.-D. Mo and W. Y. Ching, Phys. Rev. B **51**, 13 023 (1995).
[2]W. L. Bragg, *Atomic Structure of Minerals* (Cornell University, Ithaca, NY, 1937), pp. 102–106.
[3]J. G. Clark, *The Chemistry of Titanium and Vanadium* (Elsevier, New York, NY, 1968), pp. 266–277.
[4]F. P. Felner, *Low Temperature Oxidation* (Wiley-Interscience, New York, NY, 1981), pp. 31–49.
[5]A. Yeung, and K. W. Lam, Thin Solid Films **109**, 169 (1983).
[6]K. Jurek, M. Guglielni, G. Kuncova, O. Renner, F. Lukes, M. Navratil, E. Krousky, V. Vorlicek, and K. Kokesova, J. Mater. Sci. **27**, 2549 (1992).
[7]Y. H. Lee, K. K. Chan, and M. J. Brady, J. Vac. Sci. Technol. A **13**, 596 (1995).
[8]P. Alexandrov, J. Koprinarova, and D. Todorov, Vacuum **47**, 1333 (1996).
[9]J. M. Bennett, E. Pelletier, G. Albrand, J. P. Borgogno, B. Lazarides, C. K. Carniglia, R. A. Schmell, T. H. Allen, T. Tuttle-Hart, K. Guenther, and A. Saxer, Appl. Opt. **28**, 3303 (1988).
[10]E. Sirbegovic, M. Cevro, and I. Tucak, Vacuum **43**, 723 (1992).
[11]K. Balasubramanian, X. F. Han, and K. H. Guenther, Appl. Opt. **32**, 5594 (1993).
[12]B.-H. Jun, S.-S. Han, K.-S. Kim, J.-S. Lee, Z.-T. Jiang, B.-S. Bae, K. No, D.-W. Kim, H.-Y. Kang, and Y.-B. Koh, Appl. Opt. **36**, 1482 (1997).
[13]H. Kumagai, K. Toyoda, K. Kobayashi, M. Obara, and Y. Iimura, Appl. Phys. Lett. **70**, 2338 (1997).

[14]D. Wicaksana, A. Kobayashi, and A. Kinbara, J. Vac. Sci. Technol. A **10**, 1479 (1992).

[15]A. Kinbara, E. Kusano, and S. Baba, J. Vac. Sci. Technol. A **10**, 1483 (1992).

[16]E. Kusano, S. Baba, and A. Kinbara, J. Vac. Sci. Technol. A **10**, 1696 (1992).

[17]M. H. Suhail, G. Mohan Rao, and S. Mohan, J. Appl. Phys. **71**, 1421 (1992).

[18]L.-J. Meng and M. P. dos Santos, Thin Solid Films **226**, 22 (1993).

[19]S. M. Edlou, A. Smajkiewicz, and G. A. Al-Jumaily, Appl. Opt. **32**, 5601 (1993).

[20]D. Wicaksana, T. Tsujikawa, A. Kobayashi, K. Ono, and A. Kinbara, Mater. Res. Soc. Symp. Proc. **311**, 233 (1993).

[21]H. Tang, K. Prasad, R. Sanjines, P. E. Schmid, and F. Levy, J. Appl. Phys. **75**, 2042 (1994).

[22]R. Sanjines, H. Tang, H. Berger, F. Gosso, G. Margarditondo, and F. Levy, J. Appl. Phys. **75**, 2945 (1994).

[23]M. D. Wiggins, M. C. Nelson, and C. R. Aita, Proc. Mat. Res. Soc. **398**, 381 (1996).

[24]M. D. Wiggins, M. C. Nelson, and C. R. Aita, J. Vac. Sci. Technol. A **14**, 772 (1996).

[25]K. Okimura, N. Maeda, and A. Shibata, Thin Solid Films **281–282**, 427 (1996).

[26]D. Guerin and S. Ismat Shah, J. Vac. Sci. Technol. A **15**, 712 (1997).

[27]C. R. Aita, J. Vac. Sci. Technol. A **11**, 1540 (1993).

[28]Anatase: ASTM JCPDS File No. 21-1272 (1991).

[29]Rutile: ASTM JCPDS File No. 21-1276 (1991).

[30]Brookite: ASTM JCPDS File No. 29-1361 (1980).

[31]C. S. Barrett and T. B. Massalski, *Structure of Metals*, 3rd ed. (McGraw-Hill, New York, NY, 1966), p. 57.

[32]W. B. White, Mater. Res. Bull. **2**, 381 (1967).

[33]W. G. Lee, S. I. Woo, J. C. Kim, S. H. Choi, and K. H. Oh, Thin Solid Films **237**, 105 (1994).

[34]A. L. Calzada and L. Del Olma, J. Non-Cryst. Solids **121**, 413 (1990).

[35]T. Kamada, M. Kitagawa, M. Shibuya, and T. Hirao, Jpn. J. Appl. Phys., Part 1 **30**, 3594 (1991).

[36]G. V. Chertihin and L. Andrews, J. Phys. Chem. **98**, 5891 (1994).

[37]L. M. Williams and D. W. Hess, J. Vac. Sci. Technol. A **1**, 1810 (1983).

[38]C. S. Barrett and T. B. Massalski, *Structure of Metals*, 3rd ed. (McGraw-Hill, New York, NY, 1966), p. 621.

NANOSTRUCTURED CERAMIC COATINGS: ENGINEERING ON AN ATOMIC SCALE

C. R. Aita

In recent years, nanostructured coatings have emerged as technologically important materials. The production and analysis of nanostructured ceramic coatings bring new challenges to the materials science and engineering community. In this review, it is shown how two characteristic features of nanoscale morphology, large internal surface area and metastable phase formation owing to the finite crystal size effect, can be exploited to produce ceramic coatings with unique and useful properties.

The author is in the Materials Department, University of Wisconsin–Milwaukee, PO Box 784, Milwaukee, WI 53211, USA. Invited keynote contribution to the 12th International Conference on Surface Modification Technologies held in Rosemont, IL, USA on 12–15 October 1998.

INTRODUCTION

A nanostructured crystalline material is one in which the spacing between lattice defects approaches interatomic distances.[1] Nanometre scale morphology gives rise to two features that, either alone or in combination, can be exploited to develop ceramic coatings with unique behaviour. One feature is a large internal surface area, which has interesting physical and chemical consequences including low temperature ductility and superplasticity,[2–5] high electrical conductivity,[6,7] thermal shock resistance,[8] enhanced gas sensing,[9] enhanced diffusion barrier action,[10] and corrosion resistance.[11] A second feature is the formation of unusual phases in nanocrystallites as a result of the finite crystal size effect, i.e. a large surface energy contribution to the total Gibbs free energy of formation when the crystallite size is small.[12,13]

The recent emergence of nanostructured ceramic coatings as technologically important materials has brought new challenges regarding their production and characterisation. These challenges are addressed in this paper. First, atomic order in solids is briefly described. Next are discussed the chemical bonding conditions that predispose formation of a nanocrystalline rather than a vitreous structure in ceramic coatings grown at room temperature. Last, illustrative examples of room temperature production and characterisation of several technologically important nanoscale coatings are introduced: these coatings include single layer aluminium nitride and multilayer nanolaminates of zirconia–alumina and zirconia–yttria.

ATOMIC ORDER IN SOLIDS

Structural order in solids can be classified by the spatial extent of ordering units, as listed in Table 1. Of course, large scale order is ultimately determined by the structure within atomic scale building blocks. For example, the dissimilar macroscopic habits (appearance) of two carbon polymorphs, diamond and graphite, are a direct consequence of their very different long range order. Their respective cubic and hexagonal lattices in turn arise from different short range order, i.e. three-dimensional sp^3 bonds of nearest neighbour atoms in diamond, and two-dimensional sp^2 nearest neighbour bonds in graphite.

The spatial extent of atomic order gives rise to different microstructures, as shown in Table 2. In the absence of crystal defects (e.g. point defects, dislocations, voids, and domain, twin, and grain boundaries) the world would consist of nothing but perfect single crystals. Reduced spatial order from this state, however, first gives rise to a polycrystalline microstructure, and then to nanocrystallinity, with limited long range order. Long range order disappears entirely in a vitreous structure, which possesses chemical uniformity only in terms of nearest neighbour bonding. Even short range order is lost in an amorphous structure, which lacks chemical uniformity from one group of nearest neighbours to the next.

In this paper, a variety of ceramic materials will be discussed that have at least microstructural dimension in the range of 5 to 50 nm, or 1 to 10 unit cells. The common feature of these materials is that their technologically interesting functional properties are determined by their structure at the nanometre scale.

NANOCRYSTALLINITY IN CERAMICS

Nanocrystallinity is the extreme limit of a polycrystalline microstructure in some types of ceramic coatings. Under similar deposition conditions, however, other ceramics form vitreous microstructures. (Unlike an amorphous material, which technically has no consistent short range order, a vitreous material has short range atomic order that is often identical to that of a bulk oxide.) The best candidates for forming nanocrystalline rather than vitreous coatings are ceramics that do not have structural complexity in bulk, as described by Felner.[14] Ceramics with structural complexity have either bond flexibility giving rise to polymorphs with the same chemistry and very similar free energy of formation, or mixed valence compounds with vernier, block, or infinitely adaptive

Table 1   Classification of structural order in solids

Type of order	Basic ordering unit
Short range	Nearest neighbour atoms
Long range	Lattice
Microstructure	Grain
Macrostructure	Habit

physical structures that accommodate changes in stoichiometry.

In the case of oxides, Felner[14] discusses vitreous rather than nano- or polycrystalline growth on the basis of the energy of a single cation–oxygen bond, M–O. The M–O bond energy is defined as the heat of formation of the oxide divided by the O coordination number with the cationic (M) species. The results are summarised in Table 3. Three categories emerge. First, cations that have a high M–O bond energy are network formers in bulk oxides. Coatings of these oxides grown at room temperature are likely to have a vitreous structure: examples are niobia, tantala, alumina, silica, and germania. Second, at the other extreme, cations that have a low M–O bond energy are network modifiers when included in bulk oxides. Coatings of these oxides grown at room temperature are likely to be nanocrystalline, exemplified by the alkali metal oxides, and the oxides of the transition metals iron, manganese, cobalt, and nickel. Third, cations with an intermediate M–O bond strength can be either network formers or modifiers in bulk oxides. It is often possible to induce nanocrystallinity in coatings of these oxides grown at room temperature: examples are titania, zirconia, and yttria.

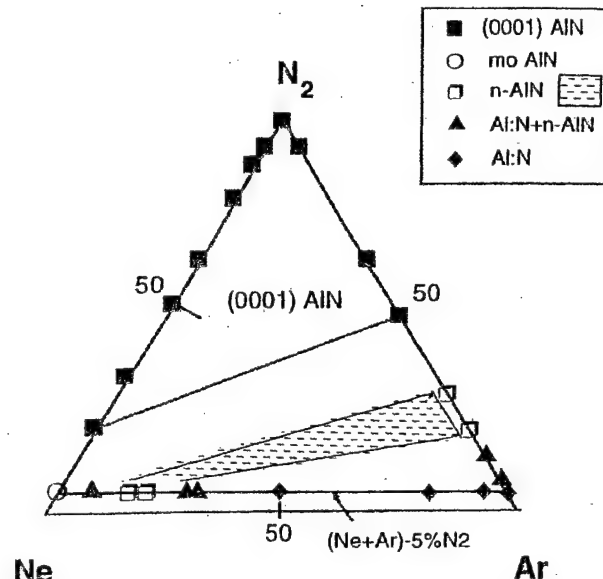## SPECIFIC CERAMIC NANOSTRUCTURES

In the Introduction, two unique features of nanoscale structure were mentioned: a large internal surface area for chemical reaction, and the formation of metastable phases as a result of the finite crystallite size effect. In the next section, it is shown how these features can be exploited to engineer single and multilayer coatings with unique and useful technological properties.

Nanostructured aluminium nitride

Aluminium nitride is a wide band gap, III–V semiconductor with a wurtzite type hexagonal close packed lattice structure that gives rise to piezoelectric behaviour. The wide range of electrical and optical thin film applications resulting from these properties are reviewed in Ref. 15. AlN is also a hard, refractory material with a high thermal conductivity, and is inert to many caustic substances, the last property being a mixed blessing because it means that AlN thin films are so difficult to pattern.[16] Most electrical and optical applications of AlN require single crystal films. In this section, however, films at the other extreme of the structural spectrum, nanocrystalline AlN, are examined and it is shown how this material can be used as a protective, self sealing, corrosion resistant coating for steel.


1   *Map of Al–N structures obtained by sputtering Al target in mixed Ar–Ne–N$_2$ discharges at fixed -1.7 kV cathode voltage and 10 mtorr total pressure*

Experimental

Films were grown by rf diode reactive sputter deposition using an Al target and rare gas (Ar, Ne, Ar + Ne)–N$_2$ discharges.[11,17–19] Two types of substrates were used: ⟨111⟩ Si from which the nascent oxide layer had not been removed, and fused silica. The substrate temperature was <300°C. Two presputters preceded each deposition, with shutters covering the substrates. The first presputter, carried out in Ar, removed the nascent oxide layer that had formed on the target surface upon air exposure. Glow discharge mass spectrometry (GDMS)[20] was used to monitor the decrease in AlO$^+$ ionic current at 43 amu and simultaneous increase in Al$^+$ ionic current at 27 amu.[17] This presputter step is critical to stoichiometric AlN production: if it is omitted, the film will be an aluminium oxynitride with irreproducible chemistry.[21] The second presputter, carried out in the gas composition used to grow the film, allowed aluminium target surface nitridation to reach dynamic equilibrium. Unfortunately, GDMS could not be used to monitor the second presputter because the AlN$^+$ ionic current at 41 amu is sufficiently close to the enormous Ar$^+$ ionic current at 40 amu, and the Al$^+$ ionic current at 27 amu is sufficiently close to the N$_2^+$ signal at 28 amu to make meaningful data impossible to obtain. Instead, optical emission spectrometry (OES)[22] was used to monitor this presputter step, as well as the subsequent deposition.[11,18,19]

Table 2   Variation of microstructure with atomic order: decreasing spatial order from top to bottom of table

Microstructure	Order
Single crystal	Long range
Polycrystalline	Long range
Nanocrystalline	Limited long range
Vitreous	Short range
Amorphous	No short range

Table 3   Effect of M–O bond energy on oxide coating structure: bond energy defined as (heat of formation)/(O coordination number of M ion in oxide)

M–O bond energy, eV	M ion type	Coating structure
>3·25	Network former	Vitreous
2·18–3·25	Intermediate	Vitreous or nanocrystalline
<2·18	Modifier	Nanocrystalline
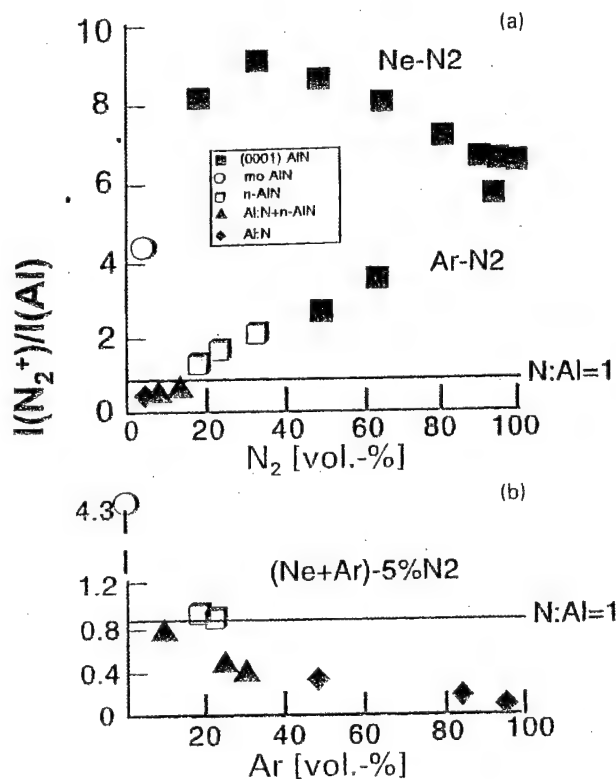
a N_2 content in Ar–N_2 and Ne–N_2; *b* Ar content in 5%N_2–Ne–Ar

2 *Variation with gas discharge composition of ratio of optical emission intensities from v_{00} band head of N_2^+ [$B \rightarrow X$] transition at 391·4 nm and Al^0[4s–3p] transition at 396·1 nm: cathode voltage −1·7 kV, total pressure 10 mtorr*

Phases and structures in sputter deposited Al–N system
Figure 1 maps the structures obtained by using Ar–Ne–N_2 discharges at a fixed cathode voltage,[11,19] and applies to growth on both fused silica and ⟨111⟩ Si substrates. The observed structures were aluminium doped with nitrogen (Al:N), nanocrystalline aluminium nitride (n-AlN), multiorientation aluminium nitride (mo-AlN), and basal orientation [(0001)] AlN. All of these structures involve one or both of the two equilibrium phases in the aluminium–nitrogen system at stp: fcc Al and hcp wurtzite type AlN. No metastable crystalline phases are formed.

Figure 1 shows that the type of rare gas used in conjunction with N_2 strongly influences phase formation for a given rare gas/N_2 ratio. Aluminium cannot be nitrided by ground state N_2, but requires an activated form of nitrogen such as N_2^+. One way in which N_2^+ is created in a Ne–N_2 discharge is by Penning ionisation, for which the energy requirement is that the metastable level of the rare gas atom should be greater than 15·58 eV, the ionisation potential of N_2. A metastable Ne atom is able to Penning ionise N_2 whereas metastable Ar cannot.[20,22]

Figure 2 shows an increase in the N_2^+/Al emission signal ratio with increasing Ne content of the sputtering gas up to 40%N_2.[11,19] Correlation with dual ion beam deposition data[23] showed that an arrival flux of one N_2^+ molecule for every two Al atoms, i.e. a unity or greater ratio N/Al, resulted in stoichiometric AlN growth. Furthermore, n-AlN formed when the N/Al ratio to the substrate was close to unity, i.e. the N_2^+ flux was entirely consumed
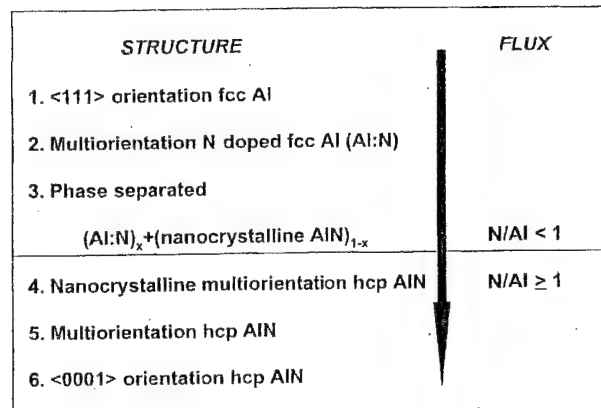

3 *Structure evolution in sputter deposited Al–N system*

by the growing film. Increasing the N/Al ratio shifted the phase formation sequence towards basal orientation AlN. These results are summarised in Fig. 3.

Structure, chemistry, and optical behaviour of nanostructured AlN
The double angle X-ray diffraction (XRD) patterns[18,19] of n-AlN coatings show broad, weak peaks corresponding to diffraction from (10−10), (0002), and (10−11) AlN planes, and there is also a featureless background that rises at lower angle. Long exposure, cylindrical camera XRD patterns of the same coatings[11,18] show arcs corresponding to weak reflections from the abovementioned AlN lattice planes. These XRD patterns are characteristic of a dual structure material consisting of small crystallites plus regions of poorly defined crystal structure.

Figure 4 is a transmission electron microscope (TEM) image of n-AlN film grown on carbon ribbon using a 95%(0·8Ne + 0·2Ar)–5%N_2 discharge.[11] The dual structure is clearly evident, showing nanocrystallites (dark regions) and an intercrystallite boundary network (light regions).
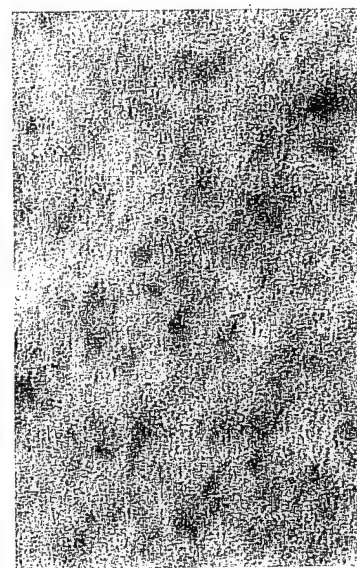
75 μm

4 *Transmission electron micrograph showing nanocrystallites (dark) and boundary network (light) of n-AlN film grown on carbon ribbon*
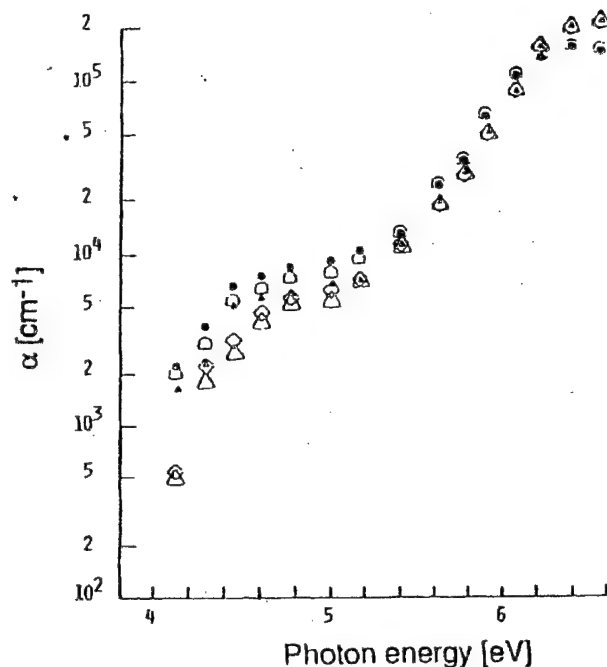
5 . *Variation of optical absorption coefficient α with incident photon energy for n-AlN grown on fused silica using Ar–N₂ discharges and Al target[11,19]*

X-ray photoelectron spectroscopy (XPS) of films on ⟨111⟩ Si and 1080 steel substrates, Auger electron spectroscopy of films on ⟨111⟩ Si, and Rutherford backscattering spectroscopy of films on carbon ribbon[24,25] showed that n-AlN is stoichiometric within the accuracy of the measurements, and that aluminium–nitrogen coordination is characteristic of the tetrahedral bonding in wurtzite type hcp AlN. However, these techniques give a spatial average and are not useful for probing bonding specifically in the crystallite boundary region.

Nanocrystalline AlN films are visually transparent and colourless in transmitted light. Near UV/visible/near IR optical transmittance and reflectance of films grown on fused silica was measured by spectrophotometery. The absorption coefficient α, calculated from these data, is shown in Fig. 5 as a function of incident photon energy E.[11,26,27] The onset of the fundamental optical absorption edge is at around 4 eV. Discrete intragap states associated with nanocrystallinity are responsible for the low energy shoulder that occurs between 4 and 5 eV. For values of energy above 5 eV, the coherent potential approximation[26,27] was used to determine the optical band gap of n-AlN. The band gap was found to range from 5·50 to 5·64 eV. This value is 0·6 to 0·7 eV lower than the optical band gap of a virtual AlN crystal (i.e. a structurally perfect crystal at absolute zero), for which $E_g = 6·18$ eV.[11,26,27]

Corrosion protection behaviour

The corrosion protection behaviour of n-AlN films on low carbon steel was measured under cathodic polarisation conditions. The average crystallite diameter in these films was 10 nm (*see* Fig. 4), and the crystallographic orientation was mixed (*see* previous section). For comparison, data were also obtained from related film materials, including mixed crystallographic orientation AlN with a 60 nm average crystallite diameter (mo-AlN), nitrogen doped aluminium (Al:N), and Al:N + n-AlN cermet. Electrochemical measurements were made using the film + steel sample as the test electrode in an equilibrated corrosion cell.[11,24,25] The electrolyte was O_2 purged 0·2M KCl. The Butler–Volmer equation[28] was used to calculate the corrosion current I_0. The relevant corrosion reaction is $Fe + 2H^+ \rightarrow Fe^{2+} + H_2$, and the cathodic half cell electrode reaction is H^+ ion reduction ($2H^+ + 2e^- \rightarrow H_2$), in which H^+ ions are formed by the dissociation of water in the electrolyte.

The corrosion current I_0, recorded in Table 4, is a measure of the steady state corrosion rate. From these data, it can be seen that the corrosion rate of n-AlN coated steel was about two orders of magnitude lower than that of bare steel and Al:N coated steel, and about an order of magnitude lower than that for Al:N + n-AlN cermet films. Furthermore, there is a strong relationship between electrical conductivity and corrosion current for non-insulating Al:N and cermet films. With respect to the effect of crystallite size in insulating AlN films, I_0 for n-AlN was about one-third of that for mo-AlN, implying advantage to the greater internal surface area in the n-AlN film.

The question now concerns the type of barrier to corrosion provided by the n-AlN coating. The three possibilities are: n-AlN is a chemically inert but physically tortuous barrier to diffusion which slows the corrosion process; n-AlN acts as a sacrificial coating, corroding at a greater rate than the underlying steel; or n-AlN chemically changes upon exposure to the electrolyte in a manner that protects the underlying steel against further corrosion, i.e. the coating 'self seals'.

Solution pH measurements and XPS provide an answer. Electrolyte pH values were determined as a function of exposure time of steel coated with n-AlN to KCl.[24,25] Measurements were taken at 24 h intervals for 7 days. Data showed that initially the OH^- concentration in the electrolyte increased, probably owing to formation of a surface hydroxide at the electrolyte/film interface by the reaction

$$AlN + 4H_2O \rightarrow Al(OH)_3 + NH_4^+ + OH^- \qquad (1)$$
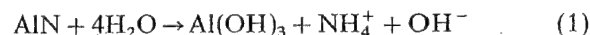
The electrolyte OH^- concentration increased by an order of magnitude from its initial value for 2 days,

Table 4   Electrical resistivity and corrosion current of n-AlN and related alloy coatings on steel: coating thickness 1·0–1·4 μm

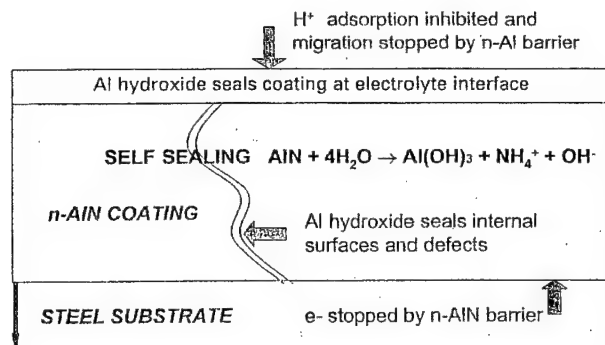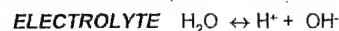| Material	Resistivity, μΩ cm	I_0, μA cm⁻²
Bulk Al	2·8	
1008 steel		4·1–5·5
Nanocrystalline AlN	Non-conductor	0·09 ± 0·03
Multiorientation AlN	Non-conductor	0·30 ± 0·10
(Al:N)ₓ + (nanocrystalline AlN)₁₋ₓ	84–219	2·1 ± 0·4 to 6·3 ± 1·6
N doped fcc Al (Al:N)	7	9·9 ± 1·9

after which it remained constant. The significance of this result is discussed below.

X-ray photoelectron spectroscopy was used to determine changes in film surface chemistry that accompanied corrosion.[24] The binding energies of N_{1s}, Al_{2p}, O_{1s}, $Fe_{2p1/2}$, and $Fe_{2p3/2}$ core photoelectron peaks from steel coated with n-AlN and Al:N were measured before and after exposure to electrolyte for 7 days. The data show that after KCl exposure, Fe bonded to O as a hydroxide was present on the surface of Al:N coated steel and absent from the n-AlN coated steel. A reaction that would produce Fe hydroxide from Fe^{2+}, a corrosion reaction product, is: $Fe^{2+} + 2OH^- \rightarrow Fe(OH)_2$. In addition, XPS data showed that the amount of N on the surface of the n-AlN coated steel was greatly reduced, and the amount of O was increased, indicating that oxidising changes occurred in the n-AlN film after exposure to the electrolyte.

The significance of these results can be seen by examining the corrosion process on an atomic level. The physical aspects of the corrosion process of bare steel in contact with an electrolytic solution can be summarised in five steps: first, H^+ arrives from solution and is adsorbed on the steel surface; second, adsorbed H^+ combines with an electron from the steel to form a neutral adsorbed H atom; third, two neutral H atoms combine to form an adsorbed H_2 molecule; fourth, many adsorbed H_2 molecules combine to form a bubble; and fifth, the bubble desorbs from the steel surface, i.e. corrosion has occurred. The fact that Fe was not present on the surface of n-AlN coated steel but was present on the surface of Al:N coated steel supports I_0 data showing that n-AlN inhibits the corrosion reaction. The n-AlN film specifically inhibits the second corrosion step by being a barrier to H ion diffusion to the underlying steel.

The n-AlN coating is not inert or sacrificial, but itself is changed in a self limiting manner by exposure to electrolyte to prevent further corrosion of the underlying steel. Solution pH measurements showed an initial increase in the amount of OH^- in the electrolyte as a result of contact with n-AlN, consistent with AlN reacting with water in the electrolyte via equation (1). The Al hydroxide that forms 'seals' the n-AlN film, after which no further change in solution pH is observed. XPS data show an increase in the amount of Al bonded to O and a decrease in the amount of Al bonded to N at the surface of the film after exposure to electrolyte, consistent with the conversion of AlN to $Al(OH)_3$. Any internal surface in the film such as a pore, fissure, or pinhole or nanocrystallite boundary exposed to electrolyte has also been experimentally observed to self seal.[24] This phenomenon is shown schematically in Fig. 6.

There are two essential ingredients in a galvanic reaction: a driving force and electromigration. The insulating behaviour of n-AlN plays an essential role in its corrosion protection ability by preventing electromigration from the film to the steel. For example, metals traditionally used as protective coatings for steel also self seal by forming a hydroxide. However, if internal surfaces exist in the metal film which enable the electrolyte to come into contact with the steel substrate, a galvanic action will be established and corrosion will occur. (In the case of

ELECTROLYTE $H_2O \leftrightarrow H^+ + OH^-$

H^+ adsorption inhibited and migration stopped by n-Al barrier

Al hydroxide seals coating at electrolyte interface

SELF SEALING $AlN + 4H_2O \rightarrow Al(OH)_3 + NH_4^+ + OH^-$

n-AlN COATING   Al hydroxide seals internal surfaces and defects

STEEL SUBSTRATE   e- stopped by n-AlN barrier

6 *Schematic diagram of nanocrystalline coating behaving as self sealing porous electrode*

Al:N and cermet films, supporting evidence comes from Table 4, showing the increase of I_0 with decreasing electrical resistivity.)

Using n-AlN as a model material, it is suggested that in order to behave as a self sealing, protective coating, a film must react with H_2O to form an insoluble sealing corrosion product and must be an electrical insulator. As a class of materials, insulating nanocrystalline ceramic coatings are especially attractive for corrosion protection because of the amount of active internal surface area on which a 'sealing' nanoscale corrosion product can form.

Phases and interfaces in zirconia–alumina and zirconia–yttria nanolaminates

This section addresses the ceramic nanolaminate coating, grown by the sequential deposition of ceramic layers. The resulting structure consists of different ceramics that are laminated together on a nanoscale. As the dimension of each constituent in the laminate decreases, the interface between components plays an increasingly important role in determining the overall properties of the coating. In turn, chemical reactivity between constituents plays an important role in determining the properties of the interface.

To illustrate this point, two pseudobinary oxide systems are examined that represent extremes in chemical reactivity between constituents. The model systems are zirconia–alumina and zirconia–yttria. The pseudobinary equilibrium phase diagram of zirconia and alumina shows very limited mutual solid solubility and no compounds.[12] On the other hand, the pseudobinary phase diagram of zirconia and yttria shows a series of solid solutions (alloys) covering the entire composition range from pure zirconia to pure yttria, and compounds are also formed.[29–33]

In addition to serving as models for diversity in chemical reactivity, these pseudobinary systems are technologically important by virtue of containing zirconia. For example, zirconia alloys with yttria to form 'stabilised cubic zirconia' (Y–CSZ), a hard, optically transparent, high refractive index material. Furthermore, zirconia is the essential component of all functional bulk transformation toughening ceramics.[12] The thermodynamic phase evolution of bulk zirconia as it is cooled from the liquidus (2680°C at atmospheric pressure) is as follows: cubic (2360°C) →
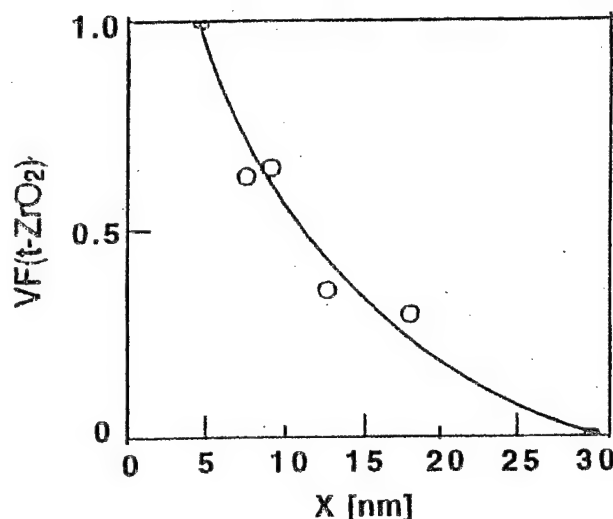
7 *Variation of tetragonal zirconia volume fraction in each bilayer with zirconia layer thickness in zirconia–alumina nanolaminates: alumina layer thickness in each bilayer 4 nm*

tetragonal (at around 1075°C) → monoclinic (stp phase). Transformation toughening depends on retention of the tetragonal phase at room temperature and the ability of this phase to transform locally to monoclinic in response to stress. The defect structure established within the daughter monoclinic phase and at the monoclinic/tetragonal phase boundary toughens the material.

Nanolaminate growth and architecture
Nanolaminates were grown by sequential sputtering of metal targets in 10^{-2} torr, rf excited O_2 discharges.[34–37] The chemical reaction at the substrate that produced the high valence oxides desired was between a metal monoxide (MO) species, sputtered intact from the oxidised surface of the metal target, and oxygen from the sputtering discharge. The growth temperature was 564 ± 10 K. Nanolaminates grown on $\langle 111 \rangle$ Si from which the nascent oxide had not been removed and on fused silica will be discussed here. In this series, the nominal zirconia thickness in the bilayer ranged from 4 to 30 nm and the nominal alumina or yttria thickness was 4 nm. Total film thickness ranged from 0·15 to 1·5 μm.

Zirconia–alumina nanolaminates
Double angle X-ray diffraction of films on fused silica and high resolution transmission electron microscopy (HREM) of films on $\langle 111 \rangle$ Si showed that the nanolaminates consisted of bilayers of polycrystalline zirconia and amorphous alumina. The phase composition of the zirconia layers changed from tetragonal to tetragonal + monoclinic to monoclinic with increasing zirconia layer thickness. The volume fraction of each zirconia phase in the bilayer was calculated using the polymorph method.[38] The volume fraction of tetragonal zirconia is shown in Fig. 7 as a function of zirconia layer thickness X.

With respect to orientation, monoclinic zirconia crystallites grew predominantly with {11–1} planes parallel to the substrate and tetragonal zirconia crystallites grew with {111} planes parallel to the substrate in all films. These orientations represent

closest packed planes aligned parallel to the substrate, and are energetically favourable when there is weak adsorbate–substrate interaction compared to the interaction among adsorbed species.[39]

The decrease in tetragonal zirconia volume fraction with increasing zirconia layer thickness seen in Fig. 7 can be understood in terms of the finite crystal size effect. Garvie[40,41] proposed an endpoint thermodynamics calculation to determine the critical size above which tetragonal zirconia crystallites spontaneously transform to monoclinic during unconstrained growth. With respect to the nanolaminates, this model assumes that all monoclinic crystallites originate from tetragonal crystallites that have grown beyond a critical size. The Gibbs free energy accompanying a tetragonal to monoclinic zirconia growth transformation is given by $\Delta G = Ar^3 \Delta g + Br^2 \Delta \gamma$, where Δg is the change in volume free energy, $\Delta \gamma$ is the change in surface free energy, r is a characteristic dimension of the crystallite (e.g. radius), and A and B are geometric factors describing the crystallite's shape, assumed to be approximately unaltered by the transformation. At the point of transformation $\Delta G = 0$, and the corresponding critical dimension can be calculated from a balance of the volume and surface energy terms.

Examination of nanolaminates by HREM with $X = 4\cdot5$ nm showed that zirconia crystallites were approximately rectangular in shape with a base $2r$ aligned parallel to the substrate plane and a height r in the growth direction.[37,42] For a rectangular crystallite

$$\Delta G = 4r^3 \Delta g + 12r^2 \Delta \gamma_{fv}$$

where $\Delta \gamma_{fv}$ is the change in surface energy of the film/vapour interface accompanying the transformation. At $\Delta G = 0$, the critical radius for a spontaneous tetragonal to monoclinic transformation during unconstrained crystallite growth is $r_c = -3\Delta \gamma_{fv}/\Delta g$. Values for the energy terms are

$$\Delta G = -2\cdot85 \times 10^8 (1 - T/1448) \text{ J m}^{-3}$$

where T is the growth temperature (in kelvin),[41] and

$$\Delta g_{fv} = g_{fv}(m) - g_{fv}(t) = (1\cdot13 - 0\cdot77) = 0\cdot36 \text{ J m}^{-2}$$

The expression for the critical radius (in nanometres) becomes

$$r_c = 3\cdot79(1 - T/1448)^{-1} \quad \ldots \ldots \ldots (2)$$

which is next applied to the experimental data. The zirconia crystallite size perpendicular to the substrate was determined from XRD line broadening using the Scherrer equation.[43] (It should be noted that the Scherrer equation gives the limiting case of broadening due to size effects with no contribution from random lattice strain or a distribution of interplanar spacing, i.e. it is the minimum possible value of the average crystallite size.)

Figure 8 shows the average tetragonal ($\langle r(t) \rangle$) and monoclinic ($\langle r(m) \rangle$) crystallite dimensions perpendicular to the substrate as a function of X. Tetragonal and monoclinic phases have different $\langle r \rangle$ versus X behaviour. Saturation of $\langle r(t) \rangle$ occurs at $6\cdot0 \pm 0\cdot2$ nm; the theoretical value obtained from equation (2) at the growth temperature (564 K) is $r_c = 6\cdot2$ nm. Based on the excellent agreement between the experimental data and theoretical calculations, it is concluded that,
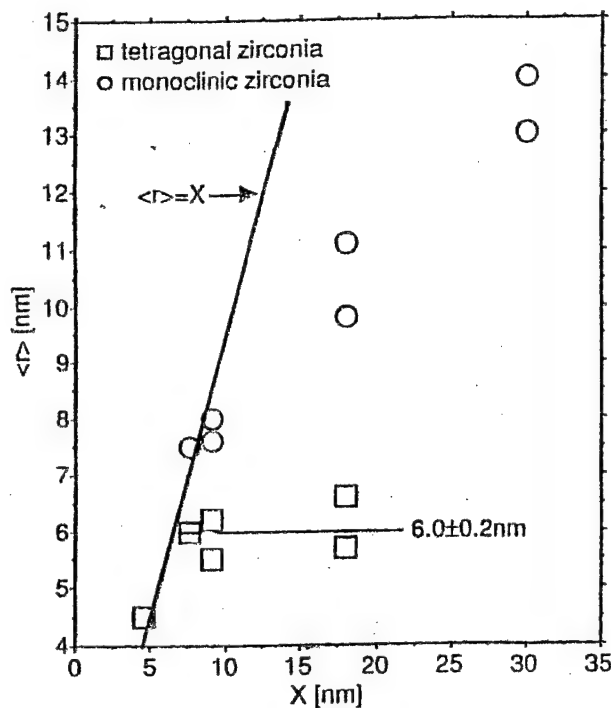
8 *Average monoclinic ($\langle r(m) \rangle$) and tetragonal ($\langle r(t) \rangle$) crystallite dimensions perpendicular to substrate as function of zirconia layer thickness X in each bilayer*[36]
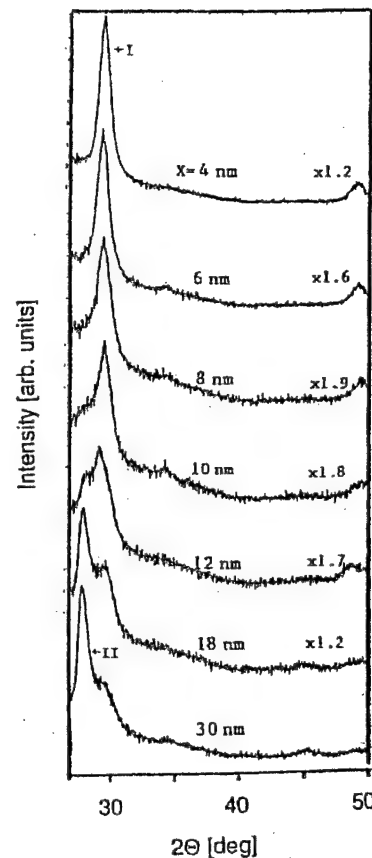

9 *X-ray diffraction patterns for zirconia–yttria nanolaminates on fused silica*

in general, nanolaminates with zirconia layer thickness less than r_c will contain zirconia in solely the tetragonal phase.

In contrast to tetragonal zirconia crystallite growth, Fig. 8 shows that $\langle r(m) \rangle$ increases linearly with zirconia layer thickness within the range $X = 7 \cdot 5{-}30$ nm. Hence, $\langle r(m) \rangle$ is a linear function of the time t to grow a layer of thickness X, and $\mathrm{d}\langle r(m) \rangle/\mathrm{d}t$ is constant. The Avrami equation[44] was therefore used to model the overall tetragonal to monoclinic zirconia growth transformation kinetics.[45] An Avrami exponent of $1 \cdot 4$ was obtained, consistent with a physical picture of the creation and subsequent growth of monoclinic crystallites from transformed tetragonal zirconia seeds of appreciable size.

Examination of nanolaminates by HREM on $\langle 111 \rangle$ Si showed a decrease of layer integrity (roughening) with increasing film thickness owing to the polycrystalline nature of zirconia, including renucleation events.[42] HREM evidence of renucleation is consistent with XRD results (Fig. 8), which show that $\langle r(m) \rangle$ for thicker layers is less than the zirconia layer thickness.

The $t \rightarrow m{-}ZrO_2$ toughening transformation in a nanolaminate with $X < r_c$ was studied using HREM.[37] The nanolaminate, consisting of 50 zirconia–alumina bilayers, was grown on the nascent oxide of a $\langle 111 \rangle$ Si surface. The nominal thickness of a zirconia layer was $4 \cdot 5$ nm. A cross-sectional specimen was produced by mechanical dimpling and polishing, followed by Ar^+ ion milling.

High resolution TEM lattice images and the corresponding diffractograms of individual crystallites showed that monoclinic crystallites were present even with $X < r_c$. However, these monoclinic crystallites were invariably adjacent to tetragonal crystallites in a definite orientation relationship, evidence for their origin as transformation products attributed

to mechanical stress during HREM specimen preparation. In contrast, there was no orientation relationship between adjacent tetragonal crystallites. Examination of many parent tetragonal/daughter monoclinic crystallite pairs shows: that (200) planes transversing tetragonal and monoclinic regions are invariant in spacing and angle and that the c axes of the parent and daughter phases are parallel to each other, which taken together mean that the plane and direction invariants of the $t \rightarrow m{-}ZrO_2$ stress induced transformation in the nanolaminates can be identified as $m(100) \parallel t(100)$ and $m[001] \parallel t[001]$; that the daughter $m(11{-}1)$ interplanar spacing is about 2% smaller than the bulk standard; that the $m(11{-}1){-}t,m(200)$ interplanar angle is distorted to around 64° compared to a standard value of $58 \cdot 4°$; that parent $t(11{-}1)$ planes are, in general, oriented parallel to the substrate, whereas daughter $m(11{-}1)$ planes are tilted at around 9° with respect to the substrate surface, a relationship which shows that the post-deposition $t \rightarrow m{-}ZrO_2$ transformation involves an out of plane rotation of $t(11{-}1)$ by about 9° to form $m(11{-}1)$; and, last, that the transformation is localised to nanosized regions within individual zirconia layers. The localised, distorted monoclinic transformation structure described in the last four of these observations is the likely source of the nanolaminate's toughness.

Zirconia–yttria nanolaminates
Double angle X-ray diffraction of films grown on fused silica and HREM of films on $\langle 111 \rangle$ Si showed that the nanolaminates consist of polycrystalline zirconia and an amorphous phase of indeterminate

21. J. A. KOVACICH, J. KASPERKIEWICZ, D. LICHTMAN, and C. R. AITA: *J. Appl. Phys.*, 1984, **55**, 2935–2939.
22. C. R. AITA: *J. Vac. Sci. Technol. A*, 1998, **16**, 1303–1310.
23. J. M. E. HARPER, J. CUOMO, and H. T. G. HENTZELL: *Appl. Phys. Lett.*, 1983, **43**, 547–549.
24. W. S. TAIT and C. R. AITA: *Corrosion*, 1990, **46**, 115–117.
25. W. S. TAIT and C. R. AITA: *Surf. Eng.*, 1991, **7**, 327–330.
26. C. R. AITA, C. J. G. KUBIAK, and F. Y. H. SHIH: *J. Appl. Phys.*, 1989, **66**, 4360–4363.
27. C. R. AITA: *Crit. Rev. Solid State Mater. Sci.*, 1998, **23**, 205–274.
28. A. J. BARD and L. R. FAULKNER: 'Electrochemical methods: fundamentals and applications', 103; 1980, New York, NY, Wiley.
29. R. RUH, K. S. MAZDIYASNI, P. G. VALENTINE, and H. O. BIELSTEIN: *J. Am. Ceram. Soc.*, 1984, **67**, C190–C192.
30. M. H. TUILIER, J. DEXPERT-GHYS, H. DEXPERT, and P. LAGARDE: *J. Solid State Chem.*, 1987, **69**, C153–C161.
31. C. PASCAUL and P. DURAN: *J. Am. Ceram. Soc.*, 1982, **66**, 23–27.
32. H. G. SCOTT: *J. Mater. Sci.*, 1977, **12**, 311–316.
33. H. G. SCOTT: *Acta Crystallogr. B*, 1977, **33**, 281–282.
34. C. R. AITA: US Patent 5472795, 1995.
35. C. M. SCANLAN, M. GAJDARDZISKA-JOSIFOVSKA, and C. R. AITA: *Appl. Phys. Lett.*, 1994, **64**, 3548–3550.
36. C. R. AITA, M. D. WIGGINS, R. WIIG, C. M. SCANLAN, and M. GAJDARDZISKA-JOSIFOVSKA: *J. Appl. Phys.*, 1996, **79**, 1176–1178.
37. M. GAJDARDZISKA-JOSIFOVSKA and C. R. AITA: *J. Appl. Phys.*, 1996, **79**, 1315–1319.
38. R. C. GARVIE and P. S. NICHOLSON: *J. Am. Ceram. Soc.*, 1972, **55**, 303–305.
39. E. BAUER: in 'Single crystal films', (ed. M. H. Francombe and H. Sato), 43–67; 1964, New York, NY, Macmillan.
40. R. C. GARVIE: *J. Phys. Chem.*, 1965, **69**, 1239–1243.
41. R. C. GARVIE and M. V. SWAIN: *J. Mater. Sci.*, 1985, **20**, 1193–1200.
42. M. A. SCHOFIELD, M. GAJDARDZISKA-JOSIFOVSKA, C. R. AITA, and P. M. RICE: *Thin Solid Films*, 1998, **326**, 106–116.
43. L. V. AZAROFF: 'Elements of X-ray crystallography', 193; 1968, New York, NY, McGraw-Hill.
44. J. W. CHRISTIAN: 'The theory of transformations in metals and alloys', 542; 1975, Oxford, Pergamon.
45. C. R. AITA: in 'Processing and fabrication of advanced materials V', (ed. T. S. Srivatsan and J. J. Moore), 459–469; 1997, Warrendale, PA, TMS.
46. ASTM Joint Commission on Powder Diffraction Standards, File 17–923.
47. ASTM Joint Commission on Powder Diffraction Standards, File 05–574.
48. ASTM Joint Commission on Powder Diffraction Standards, File 13–307.
49. A. S. EDELSTEIN, R. K. EVERETT, G. V. RICHARDSON, S. B. QADRI, E. L. ALTMAN, J. C. FOLEY, and J. J. PEREPEZKO: *J. Appl. Phys.*, 1994, **76**, 7850–7859.
50. K. BARMAK, C. MICHAELSEN, and G. LUCADAMO: *J. Mater. Res.*, 1997, **12**, 133–146.
51. N. HERBOTS, O. C. HELLMAN, P. YEH, Z. WANG, and O. VANCAUWENBERGHE: in 'Low energy surface interactions', (ed. J. W. Rabalais), Ch. 8; 1993, Cambridge, Wiley.
52. W. C. JOHNSON and G. MARTIN: *J. Appl. Phys.*, 1990, **69**, 1252–1264.

10   *Interplanar spacing as function of nominal zirconia layer thickness X for zirconia–yttria nanolaminates on fused silica*[27]

11   *Average cubic ($\langle r(c) \rangle$) and monoclinic ($\langle r(m) \rangle$) crystallite dimensions perpendicular to substrate as function of nominal zirconia layer thickness X for zirconia–yttria nanolaminates on fused silica*[27]

chemistry. XRD patterns from the crystalline component are shown in Fig. 9. The patterns in the range $2\Theta = 27$–$32°$ ($\lambda = 0.15418$ nm) show a single peak (I) at low values of X and an additional peak (II) as X increases. Interplanar spacing corresponding to peaks I and II was determined from the maximum intensity of high resolution scans and is shown in Fig. 10 as a function of nominal zirconia layer thickness.

Peak I was attributed to a series of cubic zirconia–yttria solid solutions with yttria mole fraction ranging from 0·26 to 0·81 (0·40 to 0·90 $YO_{1.5}$ mole fraction).[32] Specifically, peak I was assigned to the (111) planes of the fluorite structure for yttria mole fraction less than 0·48 (0·65 $YO_{1.5}$ mole fraction) and to the (222) planes of the bixbyite structure for yttria mole fraction greater than 0·48. The interplanar spacing of the (111) peak of tetragonal zirconia[46] and the (222) peak of cubic yttria[47] is also indicated in Fig. 9 to demonstrate why these assignments have been ruled out as primarily responsible for diffraction peak I. Peak II was assigned to the (11–1) planes of monoclinic zirconia.[48] A peak at $2\Theta = 49·1$–$49·4°$ was assigned to the (220) or (440) planes of the abovementioned cubic zirconia–yttria alloy structures.[32]

With respect to crystallite orientation, monoclinic zirconia crystallites grew predominantly with (11–1) planes parallel to the substructure and cubic zirconia crystallites grew predominantly with (111) or (222) planes parallel to the substrate. As in the case of zirconia–alumina nanolaminates, these preferred orientations are the closest packing structures parallel to the substrate, and therefore are energetically favoured.[39] However, unlike the case of zirconia–alumina, additional orientations in both the monoclinic zirconia and cubic zirconia–yttria phases were present.

Figure 11 shows the average cubic ($\langle r(c) \rangle$) and monoclinic ($\langle r(m) \rangle$) crystallite dimensions perpendicular to the substrate as a function of X. The most striking feature of this data is that $\langle r(c) \rangle$ is greater than the nominal zirconia layer thickness for $X = 4$
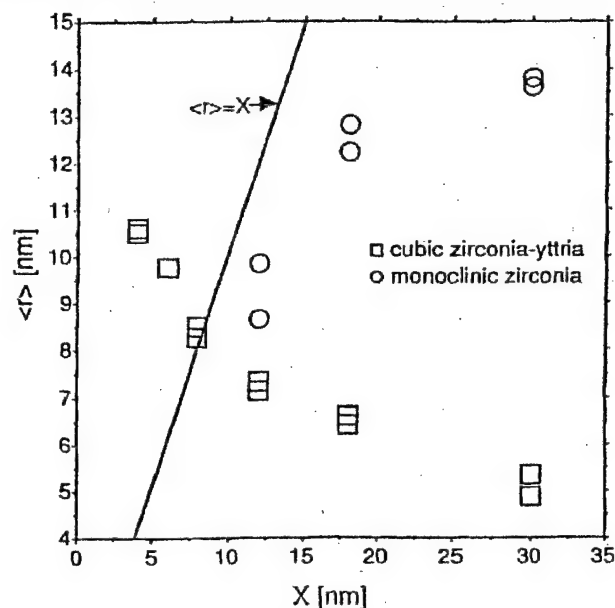
to 8 nm. (The Scherrer equation assumes that only a single value of interplanar spacing is responsible for peak broadening and so the average value obtained from the diffraction peak maximum has been used in the calculation. Since the cubic phase most likely contains a range of interplanar spacings corresponding to a range of yttria concentrations, the values obtained here for $\langle r(c) \rangle$ are most likely smaller than the actual physical size of the crystallites.) The result that $\langle r(c) \rangle$ was greater than X is consistent with atomic mixing of zirconia and yttria in a single bilayer to form the alloys described above. It is therefore concluded that these alloys are characteristic of the zirconia–yttria interface, even for nanolaminates with thick zirconia layers. It can also be seen from Fig. 11 that $\langle r(m) \rangle$ is never smaller than about 9 nm, and increases with increasing X. This result is consistent with that for zirconia–alumina nanolaminates discussed above, i.e. the monoclinic zirconia phase is not thermodynamically favoured in small crystallites.

Examination of nanolaminates grown on the nascent oxide of a $\langle 111 \rangle$ Si surface by HREM showed that the first zirconia layer ($X = 4$ nm) had a sharp interface with the substrate. However, the interface between this layer and the first yttria layer was virtually obliterated, as were all successive interfaces. Columnar crystallites extending tens of nanometres in the growth direction were the prevailing structures in films in which X was nominally 4 to 8 nm. This morphology is qualitatively consistent with the XRD measurements of cubic zirconia–yttria alloy crystallite size shown in Fig. 11. Furthermore, HREM measurements on these extended crystallites showed interplanar spacing within the range of the cubic zirconia–yttria alloys.[32]

From these data, it is concluded that zirconia–yttria nanolaminate morphology is roughened by an interfacial chemical reaction between zirconia and yttria during deposition. In addition, physical

roughening also occurs in thicker zirconia layers owing to their polycrystalline nature, as is the case for zirconia–alumina nanolaminates.

Effect of constituent reactivity on nanolaminate structure

Above, data were presented for phase formation in ceramic nanolaminates with the same nominal architecture but with different chemical constituents. In particular, two model systems, zirconia–alumina and zirconia–yttria, allowed comparison of the effects of chemical reactivity between constituents at their interface.

In zirconia–alumina nanolaminates, each binary oxide constituent is a separate entity and the interface is incoherent. Phase evolution in zirconia layers of decreasing thickness was consistent with the finite crystal size effect. Namely, solely tetragonal zirconia was formed in layers whose thickness was less than the critical thickness for stabilisation of monoclinic zirconia (the stp phase). The amorphous structure of the alumina constituent is a consequence of its structural flexibility.[14] Overall morphological roughness is a consequence of the polycrystalline nature of the zirconia.

In zirconia–yttria nanolaminates, an interfacial reaction between constituents completely obliterated yttria as a separate entity. The reaction product, cubic zirconia–yttria alloy, grew in the form of needlelike crystallites, accentuating the overall morphological roughness resulting from the polycrystalline nature of the deposit. As zirconia layer thickness increased, monoclinic zirconia was produced along with the interfacial cubic zirconia–yttria alloys.

Understanding the mechanism for interfacial reactions between oxide overlayers during deposition is an important factor for producing tailored ceramic nanolaminates. Yet this area has received virtually no attention. Looking into the literature of related areas, there are hints of what may prove to be important considerations. For example, studies of as grown and post-deposition annealed intermetallic diffusion couple films show that phase formation is governed by the kinetics of the dominant migrating species rather than by thermodynamic driving forces.[49,50] In the case of the films examined here, diffusion may be assisted by athermal means, namely the low energy ion bombardment (ion 'irradiation') that is an integral part of rf sputter deposition.[27] (Implantation of energetic particles, however, was eliminated as being the chief method of delivery of reactants to the subsurface on the basis of energy considerations, and furthermore, because no evidence of mixing[51] was found in zirconia–alumina grown under identical conditions.) In addition, compositional inhomogeneity at or near the growth interface may cause elastic stress that enhances interdiffusion.[52]

These considerations have only to be applied to the zirconia–yttria system to see the complexity of the problem at hand. For example, consider compound formation at the interface in the first bilayer adjacent to the substrate. Gaseous YO, possibly Y, and several forms of oxygen species arrive at the solid zirconia overlayer and are adsorbed.[22,27] They must undergo surface and subsurface diffusion to arrive at a reaction site. The location of the site and the manner by which adsorbed species migrate to it

are unknown and must be determined. Producing a quantitative model from this elementary starting point remains a challenge for future research.

The ability to form interfacial oxide solid solutions at low temperature in a system in which the bulk equilibrium phase diagram predicts reaction between oxide components has been clearly demonstrated. The technological importance of this result is enormous: thin films consisting entirely of interface reaction products can be fabricated at room temperature if the bilayer spacing is small enough.

SUMMARY

In summary, the low temperature fabrication of representative single and multilayer nanostructured ceramic coatings has been discussed, and their potential shown as technologically interesting materials. It is the author's hope that readers will use the information given here as a springboard for engineering new nanostructured coatings.

ACKNOWLEDGEMENTS

REFERENCES

1. H. GLEITER: *Nanostructured Mater.*, 1992, **1**, 1–19.
2. G. S. WAS and T. FOECKE: *Thin Solid Films*, 1996, **286**, 1–31.
3. R. LAPPALAINEN and R. RAJ: in 'Microcomposites and nanophase materials', (ed. D. C. Van Allen *et al.*), 41–51; 1991, Warrendale, PA, TMS.
4. H. HAHN: *Nanostructural Mater.*, 1993, **2**, 251–265.
5. H. HAHN and R. S. AVERBACK: *Nanostructured Mater.*, 1992, **1**, 95–100.
6. F. A. MODINE, D. LUBBEN, and J. B. BATES: *J. Appl. Phys.*, 1993, **74**, 2658–2664.
7. A. H. M. ZAHIRUL ALAM, Y. TAKASHIMA, K. SASAKI, and T. HATA: *Thin Solid Films*, 1996, **279**, 131–134.
8. T. HIRANO, K. IZAKI, and K. NIIHARA: *Nanostructured Mater.*, 1995, **5**, 809–818.
9. Z. PENG, Z. LI, M. ZHAO, H. CAI, S. ZHAO, G. HU, and B. XU: *Thin Solid Films*, 1996, **286**, 270–273.
10. M. UEKUBO, T. OKU, K. NII, M. MURAKAMI, K. TAKAHIRO, S. YAMAGUCHI, T. NAKANO, and T. OHTA: *Thin Solid Films*, 1996, **286**, 170–175.
11. C. R. AITA and W. S. TAIT: *Nanostructured Mater.*, 1992, **1**, 269–280.
12. D. F. GREEN, R. H. J. HANNINK, and M. V. SWAIN: 'Transformation toughening of ceramics', 1–15; 1989, Boca Raton, FL, CRC Press.
13. G. SKANDAN, C. M. FOSTER, H. FRASE, M. N. ALI, J. C. PARKER, and H. HAHN: *Nanostructured Mater.*, 1992, **1**, 313–322.
14. F. F. FELNER: 'Low temperature oxidation', 31–53; 1981, New York, NY, Wiley-Interscience.
15. S. STRITE and H. MORKOC: *J. Vac. Sci. Technol. B*, 1992, **10**, 1237–1266.
16. J. R. MILEHAM, S. J. PEARTON, C. R. ABERNATHY, J. D. MACKENZIE, R. J. SHUL, and S. P. KILCOYNE: *Appl. Phys. Lett.*, 1995, **67**, 1119–1121.
17. C. R. AITA: *J. Appl. Phys.*, 1982, **53**, 1807–1808.
18. C. R. AITA and C. J. GAWLAK: *J. Vac. Sci. Technol. A*, 1983, **1**, 403–406.
19. J. R. SIETTMANN and C. R. AITA: *J. Vac. Sci. Technol. A*, 1988, **6**, 1712–1716.
20. C. R. AITA: *J. Vac. Sci. Technol. A*, 1985, **3**, 625–630.

Correlation between titania film structure and near ultraviolet optical absorption

J. D. DeLoach

Department of Electrical Engineering and Computer Science, College of Engineering and Applied Science and the Laboratory for Surface Studies, University of Wisconsin-Milwaukee, P.O. Box 784, Milwaukee, Wisconsin 53201

G. Scarel

Materials Department, College of Engineering and Applied Science and the Laboratory for Surface Studies, University of Wisconsin-Milwaukee, P.O. Box 784, Milwaukee, Wisconsin 53201

C. R. Aita

Department of Electrical Engineering and Computer Science and Materials Department, College of Engineering and Applied Science and the Laboratory for Surface Studies, University of Wisconsin-Milwaukee, P.O. Box 784, Milwaukee, Wisconsin 53201

Titania is a material with structural flexibility, and as a result, readily forms both crystalline polymorphs and an amorphous structure in thin films grown near room temperature. The goal of this study is to correlate fundamental optical absorption edge characteristics with the phase constituency of titania films. To that end, films with coexistent rutile, anatase, and amorphous constituents were sputter deposited onto fused silica and $\langle 111 \rangle$-Si substrates. The films were then subjected to cyclic annealing in air at moderate temperature (700 and 1000 °C) to affect phase changes. Bragg–Brentano x-ray diffraction was used for phase identification and near ultraviolet-visible transmission and reflection spectrophotometry was used to determine the optical absorption coefficient at the onset of interband transitions. The optical absorption coefficient was modeled within the framework of the coherent potential approximation (CPA), with Gaussian site disorder introduced into the valence and conduction bands of a perfect virtual crystal. Two parameters of the disordered crystal were defined: the optical band gap, E_x, and the slope of absorption edge, E_o. The results are discussed in terms of two extreme cases: (1) film states containing a large rutile volume fraction (0.70–1) share a rutile virtual crystal, with $E_g = 3.22$ eV. Data for these states was combined with single crystal data to develop an expression interrelating E_g, E_x, and E_o. This expression is applicable to *any* structure with a rutile virtual crystal. The relationship between structural disorder (i.e., the volume fraction of amorphous material) and electronic disorder (i.e., E_o), is quantitatively consistent with the CPA model. (2) Film states containing a small rutile volume fraction (0.02–0.17), and hence a large anatase+amorphous component, share a nonrutile virtual crystal, with $E_g = 3.41$ eV. The effect of increasing the structural disorder (i.e., the rutile volume fraction), in these states is to shift E_x to lower values, which is qualitatively consistent with the CPA model. Furthermore, anatase and amorphous components can be modeled using the same nonrutile virtual crystal, indicating these structures have a common short-range order in the sputter deposited films of this study. © *1999 American Institute of Physics.* [S0021-8979(99)05904-6]

I. INTRODUCTION

Thin film titania (TiO_2) is a versatile material and therefore has been the subject of sustained research interest. Its diverse applications include high dielectric capacitors in dynamic-random-access-memory[1] and electroluminescent devices,[2] transparent protective coatings on silica optical fibers,[3] antireflective single layer coatings for Si solar cells[4] and deep ultraviolet (UV) lithography,[5] and as the high refractive index component of multilayers for optical antireflectors[6,7] and soft x-ray reflectors.[8] All of these optical and electrical applications depend upon the electronic structure of the material, which in turn, depends upon its atomic structure.

Bulk crystalline titania at atmospheric pressure and room temperature has three polymorphs, rutile, anatase, and brookite.[9,10] Rutile is the thermodynamically stable phase at all temperatures, while anatase and brookite exist as metastable phases below ~800 °C.[11] Titanium is in octahedral coordination with O as TiO_6 units in all polymorphs. However, the polymorphs have different Ti–O bond length and angle, i.e., short-range order, and consequently, different arrangements of the TiO_6 octahedra to form a lattice, i.e., long-range order. Rutile and anatase are tetragonal with $P4_2/mnm$ and $I4_1/amd$ space groups, respectively, and brookite is orthorhombic with $Pbca$ symmetry.[12] In addition to the stoichiometric polymorphs, nonstoichiometric titania forms a series of daughter structures derived from shear operations on a rutile mother structure with the general formula Ti_nO_{2n-1} where $4 \leqslant n \leqslant 10$.[13]

Bulk oxides with structural complexity are likely to form vitreous or amorphous structures in thin films. Structural complexity means (a) bond flexibility giving rise to polymorphs with the same chemistry and/or (b) similar free energy of formation and mixed valence compounds with vernier, block, or infinitely adaptive physical structures that accommodate changes in stoichiometry.[14] Titania meets both criteria, and it is not surprising that films grown at low temperature by diverse processes are marked by the presence of an amorphous phase, either alone or coexisting with an anatase and/or rutile crystalline phase.[15-31] Furthermore, Eastman[32] reported an amorphous structure coexistent with crystalline material in freestanding nanostructured titania, and astutely pointed out that this phase is likely to be overlooked because its detection is difficult. Two studies of amorphous titania suggest that both anatase[16] and rutile[33] short-range order are possible.

Based on the above information, we see that a titania film grown at room temperature can consist of up to three structural entities: crystalline anatase and rutile phases and an amorphous constituent. Predicting film properties at elevated temperature depends upon understanding the stability of each of these components. To this end, several investigators have studied the kinetics of amorphous→anatase, amorphous→rutile, and anatase→rutile transformations in thin films, induced by postdeposition annealing. For example, Howitt and Harker,[18] based on transmission electron microscopy data, modeled the amorphous→anatase transformation in terms of the crystallization of a supercooled liquid. Hsu *et al.*,[19] using Raman spectroscopy, and Wiggins *et al.*,[24,25] using x-ray diffraction, found that both the amorphous→anatase and amorphous→rutile transformations were strongly dependent upon the existence of crystalline "seeds" of the appropriate phase within the amorphous matrix. Their results explicitly prove the hypothesis of Shiojiri[15] proposed in an early *in situ* transmission electron microscopy investigation of electron beam-irradiated amorphous titania films: different crystal structures produced by annealing have their origins in the intrinsic properties of the as-deposited amorphous films.

The goal of the present study is to correlate atomic structure and fundamental optical absorption edge characteristics in titania films containing anatase, rutile, and amorphous constituents. Experimental and theoretical studies of the electronic properties of bulk single crystal titania[12,34-41] show that the stoichiometric polymorphs give rise to different joint density of electronic states, and therefore to different interband transition behavior in the vicinity of the fundamental absorption edge. This information can be used to analyze even the most disordered (e.g., amorphous) film if we consider a general rule stated by Tauc:[42] interband optical transitions that can be described by wave functions localized over distances on the order of the lattice constant are relatively unchanged by disorder. Restated in a manner directly relevant to our experiment, ceramics with similar short range order have similar gross features in their fundamental optical absorption edge.

The experimental program in the present study included film growth by reactive sputter deposition, characterization

TABLE I. Growth time and film thickness of titania films.

Film	Time [min]	Thickness [nm]
A	135	256
B	360	705 ± 30

by x-ray diffraction and near ultraviolet-visible spectrophotometry, and postdeposition cyclic annealing to successively modify atomic structure. In this manner, coevolution of atomic structure and the fundamental optical absorption edge was determined. Optical absorption edge data were analyzed in terms of the coherent potential approximation (CPA).[43-45] This formalism is an alternative to the Tauc[42] and Cody[46] models for the optical edge of disordered semiconductors. An advantage of the CPA model is that it defines three key optical edge parameters: the optical band gap, E_x, and the slope of absorption edge, E_o, of the disordered crystal, and the band gap, E_g, of the perfect virtual crystal. Furthermore, the CPA model provides a mechanism for relating electronic and structural disorder.

II. EXPERIMENTAL PROCEDURE

A. Film growth

Titania films were grown in a diffusion-pumped, planar diode, radio frequency-excited sputtering system. The target was a 13 cm diameter, 99.995% pure Ti disk bonded to a Cu backing plate attached to the cathode. The substrates, Suprasil fused silica rounds and $\langle 111 \rangle$ Si wafers, were placed on an unheated Cu pallet covering the anode. The cathode-to-anode spacing was 9 cm. The chamber was evacuated to a base pressure of $< 7 \times 10^{-7}$ Torr and backfilled with 1×10^{-2} Torr O_2 at a flow rate of 10 sccm. A plasma was established at a voltage of -1.2 ± 0.1 kV (peak-to-peak) corresponding to a forward power level of 300 W. The target was presputtered for 15 min before the movable shutter covering the substrates was opened and films were deposited for the time recorded in Table I.

B. Film characterization

A portion of the $\langle 111 \rangle$ Si substrate was masked during deposition to produce a step from which film thickness was measured using profilometry. Film thickness is recorded in Table I. The growth rate was determined by dividing thickness by deposition time and found to be 1.9 ± 0.2 nm/min.

Double-angle x-ray diffraction (XRD) of films on fused silica substrates was carried out using unresolved 0.154 18 nm wavelength Cu $K\alpha$. The diffractometer was calibrated using an unstressed Si standard with a {111} peak at $2\theta = 28.44° \pm 0.01°$ and a full width at one-half maximum intensity full width at half maximum (FWHM) of 0.2°. Data was acquired over the $2\theta = 20° - 70°$ range because reference diffraction patterns for the titania polymorphs show that all first order peaks occur within this interval.[47-49] Peak position ($2\theta_{hkl}$), maximum intensity, and FWHM were measured from high resolution scans of individual peaks. Integrated intensity (I) was calculated by taking the product of the

maximum intensity and the FWHM. Phase identification and preferred orientation were determined from these data.

Near ultraviolet-visible spectrophotometry was carried out on films on fused silica substrates. Transmittance, T, and reflectance, R, measurements of near-normal incident radiation were made in laboratory air at room temperature as a function of incident photon energy, E. An Al mirror was used for apparatus calibration in reflection mode. The absorption coefficient, α, in the spectral region of high absorption ($\alpha > 10^3 \text{ cm}^{-1}$) was calculated from the expression[50]

$$T = [(1-R)^2 \exp(-\alpha x)]/[1 - R^2 \exp(-2\alpha x)], \qquad (1)$$

where x is the film thickness.

In addition to the films, a 0.5-mm-thick, (110)-orientation rutile single crystal was analyzed. These data provided small values of α needed for the CPA analysis of the optical absorption edge described in Sec. IV.

C. Postdeposition annealing

Cyclic annealing in laboratory air was carried out on films grown on fused silica. The purpose of annealing was to produce film states with different phase composition. Films were introduced into a furnace at 700 °C and annealed for a sequence of 0.5 h+0.5 h+4.0 h (5 h total time), and then given a final anneal at 1000 °C for 1 h. Films were air cooled after each annealing step and analyzed using the methods described in Sec. II B.

III. RESULTS

A. X-ray diffraction

Figure 1 shows the XRD patterns of films A and B on fused silica after each annealing step. The magnification given in Fig. 1 refers to the final state of each film. A broad peak centered at $2\theta = \sim 22°$ on all patterns is due to diffraction from nanocrystallites in the fused silica substrate. This peak provided an internal intensity calibration; its average intensity based on data from all film states was 1004±7 counts, an error of 7%.

The XRD spectra of as-deposited films have the following common features: (a) Rutile and anatase phases are present. (b) The dominant reflection is from anatase {101} planes at $2\theta = 25.4°$, with additional reflections from {004} planes at $2\theta = \sim 38°$ and {200} planes at $2\theta = \sim 48°$. (c) Only rutile {110} reflections are present. (d) All peaks are broad, indicating small crystallite size and/or random lattice strain. (e) All peaks have low intensity, suggesting that amorphous titania coexists along with the crystalline phases.

The changes in crystallinity produced by annealing can be described as follows. Annealing the as-grown films at 700 °C for 0.5 h (2nd state) increased the intensity and narrowed the width of all peaks. Further annealing at 700 °C for a cumulative time of 1 h (3rd state) caused the anatase reflections to disappear from film A and strongly decreased their intensity in film B. The rutile peak intensity increased in film A by 22% and decreased in film B by 21% compared to its 2nd state values. (The reason for the anomalous behavior in film B is unknown.) Anatase reflections vanished from film B after a cumulative annealing time of 5 h at 700 °C (4th
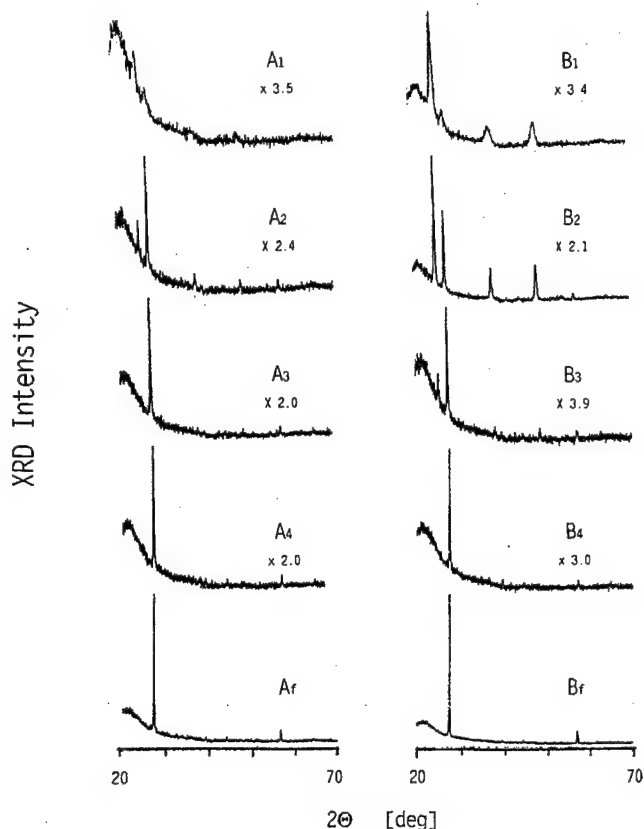

FIG. 1. XRD spectra of titania films A and B. The designated magnification refers to the final state of each film which has a magnification of unity.

state). The rutile peak intensity decreased in film A by 6% (within experimental error of its 3rd state value) and increased in film B by 21% compared to its 3rd state value. Further annealing for 1 h at 1000 °C (final state) produced a 135% increase in the rutile {110} reflection in film A and a 300% increase of this reflection in film B above its 4th state values.

Addressing the question of preferred orientation, the data show that the rutile constituent exists with solely a {110} orientation in all annealed states. Preferred orientation growth of the anatase constituent was determined by comparing the relative intensities of each film state to those of a randomly oriented powder standard.[47] The results, given in Table II, show that in all cases, the relative peak intensities are different from those of the powder standard. This finding is significant because it prevents us from quantifying the

TABLE II. Relative XRD intensity of anatase reflections in titania, as-grown and annealed at 700 °C.

Film state	Cumulative annealing time [h]	Rel. Intensity (101)/(200)/(004)
A_1	0	100/23/18
A_2	0.5	100/16/14
B_1	0	100/25/19
B_2	0.5	100/26/23
B_3	1.0	100/9/8
Powder standard (Ref. 47)		100/33/22

FIG. 2. The optical absorption coefficient as a function of incident photon energy for states of film A grown on fused silica. Included is a theoretical curve for rutile from Ref. 34.

volume fraction of anatase in the films, as discussed in Sec. IV A.

B. Spectrophotometry

All films grown on fused silica were colorless and transparent in transmitted light. The optical absorption coefficient, calculated using Eq. (1), is shown as a function of incident photon energy in Fig. 2 for states of film A and in Fig. 3 for states of film B. For comparison, a theoretical calculation by Eagles[34] is included in these figures. Eagles' calculation is in excellent agreement with experimental data for rutile films[34,40] and thin plates.[34]

A comparison of Figs. 2 and 3 shows that the fundamental optical absorption edge (FOAE) evolves differently in films A and B upon annealing. Specifically, the FOAE of as-grown film A is shifted to lower energy after a cumulative
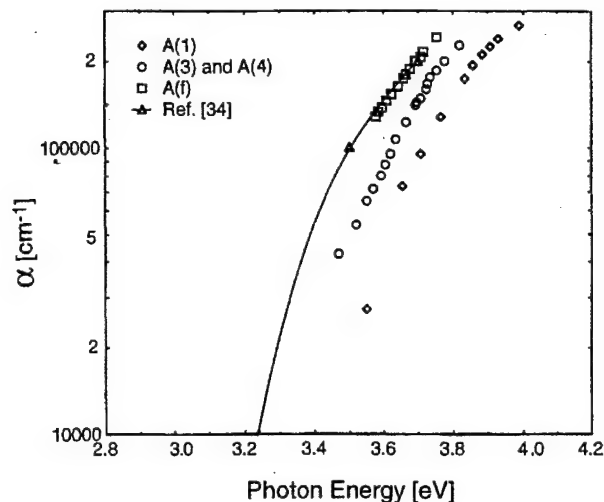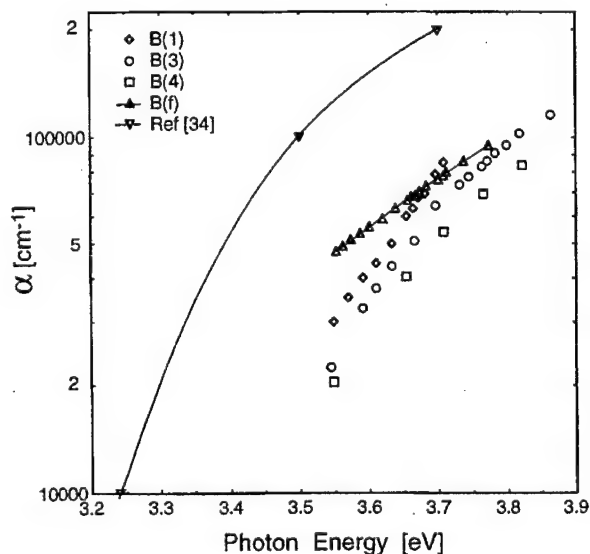

FIG. 3. The optical absorption coefficient as a function of incident photon energy for states of film B grown on fused silica. Included is a theoretical curve for rutile from Ref. 34.

1 h anneal at 700 °C. Annealing for cumulative time of 5 h at 700 °C produces no change in the FOAE. A final anneal for 1 h at 1000 °C further shifts the FOAE to lower energy, bringing it into coincidence with published data for rutile.[34,40] The high-α region of the FOAE of as-grown film B is shifted to higher energy after cumulative annealing times of 1 and 5 h at 700 °C. A final anneal of 1 h at 1000 °C shifts the FOAE to lower energy, and in addition, drastically changes its slope. Unlike film A, a high temperature anneal of film B does not bring its FOAE into coincidence with published data for rutile.

IV. DISCUSSION

A. Phase composition

The rutile volume fraction in each film state was determined using the external standard method.[51] In general, the volume fraction of the ith component of a uniform multiphase mixture, f_i, is related to the integrated intensity of a specific reflection, $I_{hkl}^{(i)}$, as

$$I_{hkl}^{(i)} = K f_i / \mu, \qquad (2)$$

where K is a composition-independent constant but specific to each reflection and apparatus geometry, and μ_{mix} is the mass absorption coefficient of the mixture. A similar equation can be written for a standard consisting entirely of the ith component, in which case $f_i = 1$,

$$I_{hkl} = K / \mu_{pure}, \qquad (3)$$

where μ_{pure} is the mass absorption coefficient of the pure material. Dividing Eq. (3) by Eq. (2), we obtain $I_{hkl}^{(i)}/I_{hkl} = (f_i/\mu_{mix})/\mu_{pure}$. In the case of a mixture of polymorphs, as we have here, $\mu_{mix} = \mu_{pure}$ and,

$$I_{hkl}^{(i)}/I_{hkl} = f_i. \qquad (4)$$

In order to apply Eq. (4) to our films, we must identify a standard film that does not contain amorphous or anatase constituents *and* has the same preferred orientation as the film state to be analyzed. After a final 1 h anneal at 1000 °C, film A yields a rutile XRD pattern with two orders of a single {110} orientation, and critically important, its fundamental optical absorption edge agrees with published data for rutile.[34,40] On this basis, film state A_f was chosen as the standard for a fully crystallized film with $f_R = 1$. Thus, $f_R = I_{110}(A_{1-4})/I_{110}(A_f)$ for film states A_{1-4}. A similar procedure was followed to calculate the rutile volume fraction in all states of film B, with the added stipulation that the thickness difference between film B and film A must be taken into account (see the Appendix A). Thus, $f_R = 0.43[I_{110}(B_{1-f})/I_{110}(A_f)]$ for all states of film B. The volume fraction of rutile in all film states is recorded in Table III.

We have assumed that all film states with the exception of A_f contain an amorphous component. Consequently, the straightforward calculation $f_A = 1 - f_R$, where f_A is the anatase volume fraction, is not valid. Furthermore, f_A cannot be calculated by comparing a specific anatase peak to that of an external standard, which would require a standard with the same anatase preferred orientation as in each film state. In addition, the preferred orientation of both the anatase and

TABLE III. Phase composition of titania films.

| Film state	Cumulative time [h]/temp. [°C]	f_R	$f_A + f_{amorph}$	f_{amorph}
A_1	0	0.05	0.95	⋯
A_2	0.5/700	0.37	0.63	⋯
A_3	1.0/700	0.45	⋯	0.55
A_4	5.0/700	0.42	⋯	0.58
A_f	5.0/700+1.0/1000	1.00	⋯	0
B_1	0	0.02	0.98	⋯
B_2	0.5/700	0.17	0.83	⋯
B_3	1.0/700	0.14	0.86	⋯
B_4	5.0/700	0.17	⋯	0.83
B_f	5.0/700+1.0/1000	0.70	⋯	0.30

FIG. 4. $\alpha^{1/2}$ vs photon energy for film states A_f, and B_f that are predominantly rutile. The intersection of these lines defines $E_g = 3.22$ eV for a rutile virtual crystal. The intersection of these lines with the abscissa defines $E_x = 3.11$ eV for A_f and 3.02 eV for B_f (see Table IV).

rutile phases precludes using the direct comparison method of Averbach and Cohen[52] or any of the other standardless methods discussed by Zervin and Kimmel[53] to obtain meaningful values of f_A. Therefore, in the case of states containing anatase, the nonrutile volume fraction is recorded as $f_A + f_{amorph}$ in Table III.

B. Formalism for fundamental optical absorption edge analysis

In general, experimental data show that the optical absorption edge of a disordered semiconductor consists of a low energy region (denoted "I" in the following text) in which α varies as $\exp(E)$, and a high energy region (denoted "II") in which α varies as E^2. Several models[42–44,46] have been proposed to explain this behavior. Historically, region II has received the most attention because it predominates in amorphous Si and tetrahedral-bonded narrow band gap semiconductors. The widely used Tauc model[42] is based on region II behavior, with region I treated as an adjunct through modification of the density of states at the band edges to include states with localized wave functions. However, a desire to integrate optical behavior in both regions through interrelated energy parameters led us to use an alternative model to analyze the FOAE of titania. This formalism is described next.

Following Abe and Toyozawa,[43] Cody,[44] and Yonezawa and Morigaki[54] α versus E data were treated within the framework of the coherent potential approximation. Gaussian site disorder, originating from both structural and thermal sources, is introduced into the valence and conduction bands of a virtual crystal with an electronic band gap, E_g. The virtual crystal has the same average nearest and next-nearest neighbor bonding in the amorphous state as a perfect crystal of the material at 0 K.[44,45] Three interrelated energy parameters are defined: (1) the virtual crystal's energy gap, E_g, (2) the energy gap of the disordered crystal, E_x, and (3) the inverse slope of the exponential region, E_o, (the Urbach tail)[55] where:

$$E_x(W,T) = E_g - D E_o(W,T). \tag{5}$$

In Eq. (5), T is the absolute temperature, W is an energy term that increases with structural and compositional disorder, and D is a constant for all structures with the same virtual crystal. The quantity E_o is proportional to W^2/B, where B is the sum of the valence and conduction band half-widths. Equation (5)
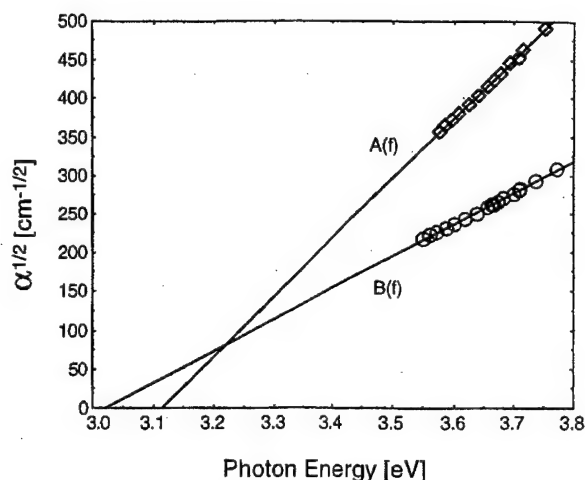
is important because it intimately connects the degree of physical disorder with the electronic disorder that causes the optical absorption edge to broaden.

Using the parameters defined above, a general expression for the absorption coefficient in region I is given by,

$$\alpha^I = C \exp[(E - E_g)/E_o], \tag{6}$$

where $C = \alpha^I(E = E_g)$. The absorption coefficient in region II is given by

$$\alpha^{II} \propto (E - E_x)^2. \tag{7}$$

We previously used the CPA formalism to analyze the FOAE of two other wide band gap semiconductors, BN[56,57] and AlN.[58]

C. The fundamental optical absorption edge of rutile films

Table III shows that only the film states A_f and B_f are entirely or predominantly rutile. Figure 4 graphs $\alpha^{1/2}$ versus E data for these states. Regression analysis was used to determine the linear best fit through the data, with a correlation coefficient of 0.999 for A_f and 0.998 for B_f. The crossing point of these lines at $E_g = 3.22$ eV defines the band gap of a rutile virtual crystal. Extrapolation of the curves in Fig. 4 to $\alpha^{1/2} = 0$ yields $E_x(A_f) = 3.11$ eV and $E_x(B_f) = 3.02$ eV. The standard estimate of error on E_x is <0.01 eV.

If we recall that α^{II} data from state A_f, and Eagles' theoretical curve[34] should lie on a continuous curve with α^I data obtained from a rutile single crystal, we can solve Eq. (5) for *any* rutile sample. Figure 5 shows these combined data. Extrapolation of α^I versus E data to E_g, shown by a solid line, determines the value of $C = 2.75 \times 10^4$ cm^{-1} in Eq. (6). Any point ($\alpha^I < C$, $E < E_g$) can be used in Eq. (6) to obtain $E_o(A_f) = 3.5 \times 10^{-2}$ eV. Note that this value is on the order of $-1/kT$, as predicted by Urbach[55] for edge broadening due to thermal vibrations in the absence of structural disorder. Placing $E_o = 3.5 \times 10^{-2}$ eV and $E_x(A_f) = 3.11$ eV
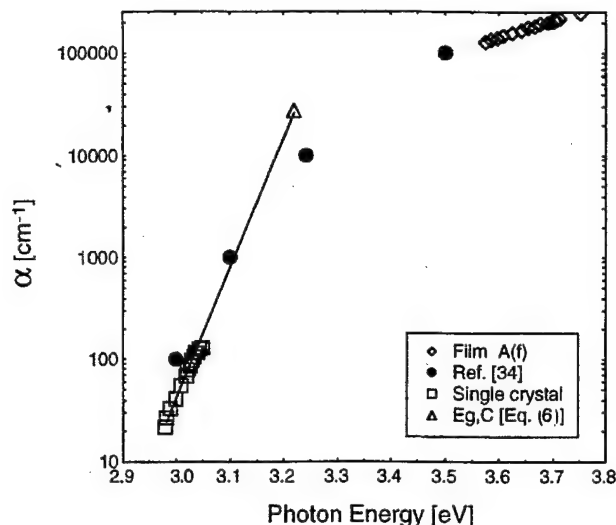
FIG. 5. α^I data obtained from a rutile single crystal (this study) and α^{II} data from film state A_f, and Eagles' theoretical curve (Ref. 34) as a function of incident photon energy. A single point indicates the values of $E_g = 3.22$ eV and $C = 2.75 \times 10^4$ cm^{-1} in Eq. (6) for any sample with a rutile virtual crystal.
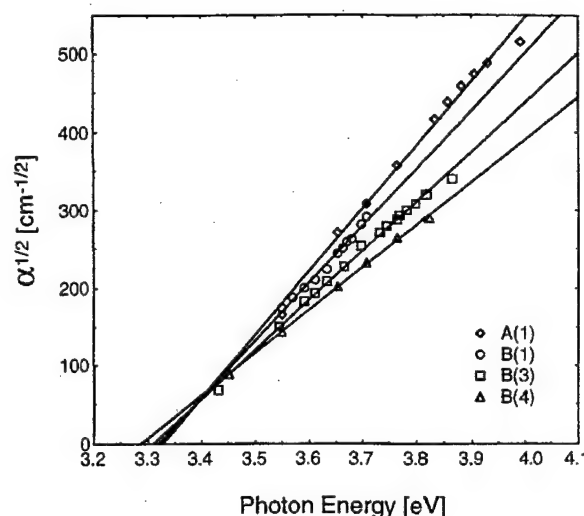

FIG. 6. $\alpha^{1/2}$ vs photon energy for film states A_1, B_1, B_3, and B_4 that are predominantly anatase+amorphous. The intersection of these lines defines $E_g = 3.41$ eV for a nonrutile virtual crystal. The intersection of these lines with the abscissa defines $E_x = 3.33$ eV for A_1, 3.32 eV for B_1, 3.31 eV for B_3, and 3.29 eV for B_4 (see Table V).

into Eq. (5) yields the constant $D = 3.14$. Equation (5) can now be generalized for any sample that has a rutile virtual crystal as

$$E_x(W,T) = 3.22 \text{ eV} - 3.14 E_o(W,T). \tag{8}$$

Substituting $E_x(B_f) = 3.02$ eV into Eq. (5) yields $E_o = 6.4 \times 10^{-2}$ eV. Table IV summarizes the optical parameters for A_f and B_f.

For materials with the same valence and conduction band half-width and at constant temperature, structural and electronic disorder are connected through the relationship: $E_o \propto W^2$. Table III shows that film state B_f contains 30% amorphous material in addition to rutile. In other words, the physical structure of film B_f is 1.3 times more disordered than pure rutile film A_f, or $W(B_f)/W(A_f) = 1.3$ If electronic disorder results from amorphous material coexistent with rutile, then $[E_o(B_f)/E_o(A_f)]^{1/2}$ should equal 1.3, as well. Substitution of the appropriate values shows $[E_o(B_f)/E_o(A_f)]^{1/2} = [6.5 \times 10^{-2}/3.5 \times 10^{-2}]^{1/2} = 1.35 \approx 1.3$, in support of this hypothesis.

D. The fundamental optical absorption edge of nonrutile films

Table III shows that film states A_1, B_1, B_3, and B_4 are predominantly nonrutile. Figure 6 graphs $\alpha^{1/2}$ versus E for these states. Regression analysis was used to determine the linear best fit through the data for each film state, with cor-

relation coefficients recorded in Table V. Extrapolation of the lines in Fig. 6 to $\alpha^{1/2} = 0$ yields the values for E_x recorded in Table V. The crossing point of these lines at $E_g = 3.41 \pm 0.02$ eV defines the band gap of a nonrutile virtual crystal. (To obtain this value, we averaged the intersection point of all six pairwise combinations of lines in Fig. 6, and corrected this data set for small sampling size.) This value of E_g is identical to that obtained by extrapolation of α versus temperature data for an anatase single crystal.[59]

Unlike the case of rutile films, CPA analysis of nonrutile films cannot be extended to the $\alpha^I(E<E_G)$ region governed by Eq. (6). The complex nature of film states A_1, and B_{1-4} precludes using single crystal anatase data for low α.[59] Therefore, we cannot solve Eq. (6) for $C(\alpha^I = 0)$ or Eq. (5) for D, and therefore cannot determine E_o.

In spite of this incomplete picture for nonrutile films, the following conclusions can be drawn. (1) Film states A_1, B_1, B_3, and B_4 have the same, albeit nonrutile, virtual crystal. Recalling Tauc's rule (see the Introduction), this result indicates that anatase and amorphous material share a common short range order in the films. (2) The effect of increasing the rutile content in film states that are predominantly anatase+amorphous produces electronic disorder, and hence shifts the values of E_x to lower energy.

TABLE IV. Optical parameters of titania films with a rutile virtual crystal structure.

Film state	E_x [eV][a]	E_o [eV]
A_f	3.11	3.5×10^{-2}
B_f	3.02	6.5×10^{-2}

[a]Standard estimate of error is <0.01 eV.

TABLE V. Optical band gap of titania films with a nonrutile virtual crystal structure.

Film state	E_x [eV][a]	Correlation coefficient
A_1	3.33	0.994
B_1	3.32	0.991
B_3	3.31	0.996
B_4	3.29	0.999

[a]Standard estimate of error is <0.01 eV.

V. SUMMARY

In this study, titania films with three coexistent constituents, rutile, anatase, and an amorphous structure, were sputter deposited onto fused silica and $\langle 111 \rangle$-Si substrates. The films were cyclically annealed in air at moderate temperature (700 and 1000 °C) to affect phase changes. Bragg–Brentano x-ray diffraction was used for phase identification, and near ultraviolet-visible transmission and reflection spectrophotometry was used to determine the optical absorption coefficient as a function of incident photon energy. The goal was to correlate fundamental optical absorption edge characteristics with the phase constituency of titania films.

In order to quantify optical behavior, the absorption coefficient was modeled within the framework of the coherent potential approximation. A virtual crystal with a band gap of E_g was defined as having the same average nearest and next-nearest neighbor bonding in the amorphous state as a perfect crystal of the material at 0 K. Disorder was introduced into the virtual crystal, and two parameters of the disordered crystal were defined: the optical band gap, E_x, and the slope of absorption edge, E_o.

The following conclusions were drawn from this study:

(1) Film states containing a large rutile volume fraction (0.70–1) share a rutile virtual crystal, with $E_g = 3.22$ eV.

(2) Data for film states with a large rutile volume fraction was combined with single crystal data to develop a general expression (Eq. 8) interrelating E_g, E_x, and E_o that is applicable to *any* structure with a rutile virtual crystal.

(3) The relationship of structural disorder (i.e., the volume fraction of amorphous material), and electronic disorder (i.e., E_o), in film states with a large rutile volume fraction is quantitatively consistent with the CPA model.

(4) Film states containing a small rutile volume fraction (0.02–0.17), and hence a large anatase+amorphous component, share a nonrutile virtual crystal, with $E_g = 3.41$ eV. Increasing structural disorder (i.e., increasing rutile volume fraction) has the effect of decreasing the value E_x (Table V). This shift is qualitatively consistent with the CPA model.

(5) Anatase and amorphous components can be modeled using the same nonrutile virtual crystal, indicating these structures have a common short-range order in the sputter deposited films of this study.

ACKNOWLEDGMENTS

APPENDIX

The correction factor that takes into account x-ray beam absorption as a function of path length, $x/\sin \theta$, is given by the expression[60]

$$G_x = 1 - \exp(-2\mu x/\sin \theta), \tag{A1}$$

where G_x is the fraction of the total diffracted intensity from a surface layer of depth x (e.g., the film thickness), μ is the atomic scattering factor, and θ is the diffraction angle for a particular set of {hkl} planes. The quantity μ/ρ, not μ, is tabulated[60] for the chemical elements, where ρ is the density. Equation (A1) is then rewritten

$$G_{(x)} = 1 - \exp[-2(\mu/\rho)(\rho x/\sin \theta)]. \tag{A2}$$

In the case of a compound material, μ/ρ can be estimated from the quantity for each element multiplied by the number of atoms of the element in the compound. Therefore, for titania, $\mu/\rho(TiO_2) = \mu/\rho(Ti) + 2\mu/\rho(O)$. Substituting values for $\mu/\rho(Ti) = 208$ cm^2/g and $\mu/\rho(O) = 11.5$ cm^2/g for the XRD conditions used here,[61] and $\rho = 4.27$ g/cm^3 for rutile,[10] we obtain G_x for the rutile {110} diffraction peak to be 0.18 for film A and 0.42 for film B. Raw peak intensity data are divided by G_x to obtain an effective value for intensity that is independent of film thickness. Therefore, we can write, $I_{110}(A)/G(x_A) = I_{110}(B)/G(x_B)$, and see that $I_{110}(B)$ must be multiplied by the factor $0.18/0.42 = 0.43$ to correct for thickness difference effects before comparison to $I_{110}(A)$.

[1] Y. H. Lee, K. K. Chan, and M. J. Brady, J. Vac. Sci. Technol. A **13**, 596 (1995).

[2] T. Nakayama, K. Onisawa, M. Fuyama, and M. Hanazono, J. Electrochem. Soc. **139**, 1204 (1992).

[3] K. Jurek, M. Guglielni, G. Kuncova, O. Renner, F. Lukes, M. Navratil, E. Krousky, V. Vorlicek, and K. Kokesova, J. Mater. Sci. **27**, 2549 (1992).

[4] K. S. Yeung and Y. W. Lam, Thin Solid Films **109**, 169 (1983).

[5] B.-H. Jun, S.-S. Han, K.-S. Kim, J.-S. Lee, Z.-T. Jiang, B.-S. Bae, K. No, D.-W. Kim, H.-Y. Kang, and Y.-B. Koh, Appl. Opt. **36**, 1482 (1997).

[6] E. Sirbegovic, M. Cevro, and I. Tucak, Vacuum **43**, 723 (1992).

[7] K. H. Guenther, Appl. Opt. **23**, 3612 (1984); **23**, 3806 (1984).

[8] H. Kumagai, K. Toyoda, K. Kobayashi, M. Obara, and Y. Iimura, Appl. Phys. Lett. **70**, 2338 (1997).

[9] W. L. Bragg, *Atomic Structure of Minerals* (Cornell University, Ithaca, 1937), pp. 102–106.

[10] J. G. Clark, *The Chemistry of Titanium and Vanadium* (Elsevier, New York, 1968), pp. 266–277.

[11] F. Dachille, P. Y. Simons, and R. Roy, Am. Mineral. **53**, 1929 (1968).

[12] S.-D. Mo and W. Y. Ching, Phys. Rev. B **51**, 13023 (1995).

[13] K. Kosuge, *Chemistry of Nonstoichiometric Compounds* (Oxford University Press, Oxford, 1994), pp. 121–128.

[14] F. P. Felner, *Low Temperature Oxidation* (Wiley–Interscience, New York, 1981), pp. 31–49.

[15] M. Shiojiri, J. Phys. Soc. Jpn. **21**, 335 (1966).

[16] T. M. Salama, T. Tanaka, T. Yamaguchi, and K. Tanabe, Surf. Sci. Lett. **227**, L100 (1990).

[17] W. G. Lee, S. I. Woo, J. C. Kim, S. H. Choi, and K. H. Oh, Thin Solid Films **237**, 105 (1994).

[18] D. G. Howitt and A. B. Harker, J. Mater. Sci. **2**, 201 (1987).

[19] L. S. Hsu, R. Rujkorakarn, J. R. Sites, and C. Y. She, J. Appl. Phys. **59**, 3475 (1986).

[20] T. Nakayama, J. Electrochem. Soc. **141**, 237 (1994).

[21] R.-Y. Tsai and M.-Y. Hua, Appl. Opt. **35**, 5073 (1996).

[22] H. Nozoye and N. Nishimiya, Appl. Phys. Lett. **54**, 231 (1989).

[23] J. D. DeLoach and C. R. Aita, J. Vac. Sci. Technol. **16**, 1963 (1998).

[24] M. D. Wiggins, M. C. Nelson, and C. R. Aita, J. Vac. Sci. Technol. A **14**, 772 (1996).

[25] M. D. Wiggins, M. C. Nelson, and C. R. Aita, Mater. Res. Soc. Symp. Proc. **398**, 381 (1996).

[26] P. Alexandrov, J. Koprinarova, and D. Todorov, Vacuum **47**, 1333 (1996).

[27] D. Wicaksana, A. Kobayashi, and A. Kinbara, J. Vac. Sci. Technol. A **10**, 1479 (1992).

[28] D. Guerin and S. Ismat Shah, J. Vac. Sci. Technol. A **15**, 712 (1997).

[29] M. G. Krisha, N. Rao, and S. Mohan, J. Appl. Phys. **73**, 434 (1993).

[30] L. M. Williams and D. W. Hess, J. Vac. Sci. Technol. A **1**, 1810 (1983).

[31] N. Martin, C. Rousselot, D. Rondot, F. Palmiro, and R. Mercier, Thin Solid Films **300**, 113 (1997).

[32] J. A. Eastman, J. Appl. Phys. **75**, 770 (1994).

[33] M. Jobin, M. Taborelli, and P. Descouts, J. Appl. Phys. **77**, 5149 (1995).

[34] D. M. Eagles, J. Phys. Chem. Solids **25**, 1243 (1964).

[35] M. Glassford and J. R. Chelikowsky, Phys. Rev. B **46**, 1284 (1992).

[36] P. I. Sorantin and K. Schwarz, Inorg. Chem. **31**, 567 (1992).

[37] K. C. Mishra, K. H. Johnson, and P. C. Schmidt, J. Phys. Chem. Solids **54**, 237 (1993).

[38] J. Pascaul, J. Camassel, and M. Mathieu, Phys. Rev. B **18**, 5606 (1978).

[39] N. Daude, C. Gout, and C. Jouanin, Phys. Rev. B **15**, 3229 (1977).

[40] H. Tang, H. Berger, P. E. Schmid, F. Levy, and G. Burri, Solid State Commun. **87**, 847 (1993).

[41] R. Sanjines, H. Tang, H. Berger, F. Gozzo, G. Margaritondo, and F. Levy, J. Appl. Phys. **75**, 2945 (1994).

[42] J. Tauc, in *Amorphous and Liquid Semiconductors*, edited by J. Tauc (Plenum, London, 1974), Chap. 4.

[43] S. Abe and Y Toyozawa, J. Phys. Soc. Jpn. **50**, 2185 (1981).

[44] G. D. Cody, in *Semiconductors and Semimetals*, Vol. 21, Part B, edited by J. I. Pankove (Academic, Orlando, 1984), Chap. 2.

[45] J. M. Ziman, *Models of Disorder* (Cambridge University Press, Cambridge, 1979), pp. 332–345.

[46] G. D. Cody, B. G. Brooks, and B. Abeles, Sol. Energy Mater. **4**, 231 (1982).

[47] Anatase: ASTM JCPDS File No. 21-1272 (1991).

[48] Rutile: ASTM JCPDS File No. 21-1276 (1991).

[49] Brookite: ASTM JCPDS File No. 29-1361 (1980).

[50] See, for example, J. I. Pankove, *Optical Processes in Semiconductors* (Prentice–Hall, Englewood Cliffs, NJ, 1971), pp. 93 and 94.

[51] H. P. Klug and L. E. Alexander, *X-ray Diffraction Processes* (Wiley, New York, 1974), pp. 532–538.

[52] B. L. Averbach and M. Cohen, Trans. AIME **176**, 401 (1948).

[53] L. S. Zevin and G. Kimmel, *Quantitative X-ray Diffractometry* (Springer, New York, 1995), pp. 188–204.

[54] F. Yonezawa and K. Morigaki, Prog. Theor. Phys. **53**, 1 (1973).

[55] F. Urbach, Phys. Rev. **92**, 1324 (1953).

[56] C. R. Aita, J. Appl. Phys. **66**, 3750 (1989); **67**, 3906 (1990).

[57] R. B. Heil and C. R. Aita, J. Vac. Sci. Technol. A **15**, 93 (1997).

[58] C. R. Aita, C. J. G. Kubiak, and F. Y. H. Shih, J. Appl. Phys. **66**, 4360 (1989).

[59] H. Tang, F. Lévy, H. Berger, and P. E. Schmid, Phys. Rev. B **52**, 7771 (1995).

[60] H. P. Klug and L. E. Alexander, op. cit (unpublished), p. 215.

[61] H. P. Klug and L. E. Alexander, op. cit (unpublished), pp. 875–877.

High refractive index ⟨100⟩-textured cubic zirconia formed in nanolaminates using titania interruption layers

J. D. DELOACH, C. R. AITA
Department of Electrical Engineering and Computer Science, Materials Department, and the Laboratory for Surface Studies, University of Wisconsin-Milwaukee, Milwaukee, WI 53211, USA

Thin film cubic zirconia is a versatile technological material, evidenced by its many applications, including thermal barrier and shock resistance coatings [1–5], intermediate buffer layers for high temperature yttrium-barium-copper oxide superconductors [6–8], mixed electronic-ionic conductors [9, 10], hard coatings [11], wear resistant coatings [12], and high refractive index films [13]. Thermodynamic phase evolution of bulk zirconia cooled from the liquidus (2680 °C at atmospheric pressure) is as follows: cubic (2360 °C) → tetragonal (~1075 °C) → monoclinic (STP phase) [14]. However, the pseudobinary zirconia-yttria phase diagram shows that the cubic phase is stabilized at room temperature by ≈10 mol% yttria [15–17]. Therefore, most reports of cubic zirconia formation in thin films involve yttria-doped zirconia. Exceptions include Moulzolf and Lad [12, 18, 19], who stabilized cubic zirconia without dopants on both crystalline and amorphous substrates using electron cyclotron resonance plasma-assisted electron beam deposition and Martin *et al.* [13], who stabilized cubic zirconia on borosilicate crown glass using ion-assisted electron beam evaporation. However, in both cases, undoped cubic ziconia grown near room temperature was in the form of nanocrystallites.

The single layer film studies also report the transformation from cubic to monoclinic zirconia with increasing crystallite size, suggesting that a finite crystal size effect is in operation. For this reason, zirconia phase control is easier in a multilayer scheme, by the introduction of growth interruption layers. This approach was taken by Yashar *et al.* [11] and Aita [20] who grew cubic zirconia in zirconia/yttria nanolaminates. In these cases, cubic zirconia was formed by heteroepitaxy with either ⟨111⟩-texture cubic yttria [11] or a ⟨111⟩-texture interfacial cubic zirconia-yttria alloy [12].

The drawbacks of using yttria for growth interruption layers are: (1) the refractive index of the nanolaminate is considerably lowered by the presence of yttria, which has a lower refractive index than cubic zirconia, and (2) the ⟨111⟩-texture of cubic zirconia is stabilized by heteroepitaxy, precluding a ⟨100⟩-texture desirable for certain applications [6–8]. To overcome both problems, we report the use of vitreous titania for interruption layers. The refractive index of vitreous titania is >2.0 in the visible spectrum [21, 22]. Furthermore, cubic zirconia has a fluorite lattice structure, in which room-temperature slip occurs on {200} planes [23]. We therefore reasoned that the {200} planes are the low energy growth surfaces, and therefore will lie parallel to an amorphous substrate [24], resulting in ⟨100⟩-textured film.

Film growth and architecture. Nanolaminates of zirconia-titania bilayer stacks were grown by reactive radio-frequency excited sputter deposition. The anode was covered with a rotating substrate table. The substrates, Suprasil II fused silica disks, were sequentially positioned under 99.5% pure zirconium and 99.995% pure titanium metal targets. The 20 mtorr, 80% Ar–20% O_2 sputtering discharge was operated at −1.5 kV (p-p), resulting in forward power levels of 470 W and 320 W for the Zr and Ti targets, respectively. The zirconia layer growth rate was 1.9 nm min^{-1} and the titania layer growth rate was 0.7 nm min^{-1}. The titania layer thickness was 1.5 nm in all nanolaminates. The number of bilayers, zirconia layer thickness, and total film thickness is recorded in Table I.

Film characterization. Double angle X-ray diffraction (XRD) was carried out using unresolved Cu K_α radiation of $\lambda = 0.1542$ nm. Low resolution "scout" scans were taken from $2\theta = 20$–90°. In addition, high resolution scans of selected peaks were used to determine peak position (2θ), maximum intensity (I), and full width of the peak at half of the maximum intensity (FWHM). The average crystallite dimension, D, perpendicular to the substrate plane was calculated using the Scherrer equation [25]: $D = 0.94\lambda/B\cos\theta$, where B is the FWHM after correction for instrumental broadening.

Near UV-visible-near IR spectrophotometry was used to measure transmittance and reflectance of 0.19–1.10 μm wavelength, near-normal incidence radiation at room temperature in laboratory air. The real part of the refractive index was calculated from the position of interference fringes in the region of high optical transparency [26].

Fig. 1 shows XRD scout scans. A broad peak centered at $2\theta = \sim22°$ is due to diffraction from

TABLE I Structural parameters for zirconia–titania nanolaminates grown on fused silica

Film	A	B	C
Number of bilayers	20	17	13
Nominal zirconia layer thickness[a] (nm)	16.2	22.0	32.0
Total film thickness (nm)	354 ± 3.5	400 ± 4.0	436 ± 4.4

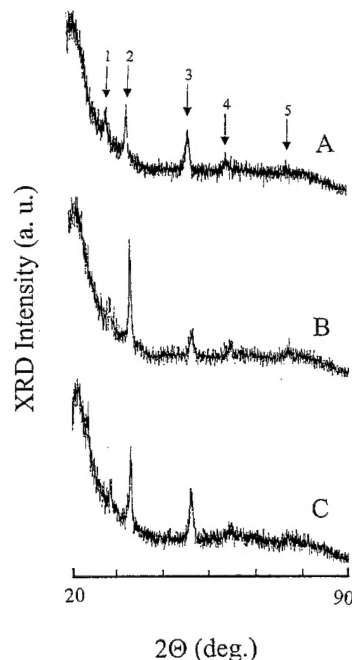[a] Nominal titania layer thickness = 1.5 nm.

2Θ (deg.)

Figure 1 Low resolution X-ray diffraction patterns of zirconia–titania nanolaminates on fused silica substrates. Numbers refer to peak assignment in Table II.

nanocrystallites in the fused silica substrate. All other peaks are attributable to polycrystalline zirconia. No XRD peaks from titania were found, consistent with previous results showing that thin single layer titania films grown under the same conditions used here have a vitreous structure [27, 28].

Films A and B show XRD peaks solely attributable to different orientations of cubic zirconia [29]. In film C, a small peak at ~25° is caused by diffraction from the (011)-(110) planes of monoclinic zirconia [30], and a low angle shoulder on peak 2 is attributable to (002) planes of tetragonal zirconia [31] and/or the (200)-(020)-(020) planes of monoclinic zirconia [30].

Table II gives cubic diffraction peak assignments, interplanar spacing, $d_{(hkl)}$, and cubic lattice constant values, calculated from the relationship: $a_o = d_{(hkl)}[h^2 + k^2 + l^2]^{1/2}$. The average value of a_o calculated from all crystallite orientations in all films is 0.5106 ± 0.0001 nm. This value is in excellent agreement with yttria-stabilized zirconia bulk powder data extrapolated to zero percent dopant: $a_o = 0.5110$ nm reported by Pascual and Duran [16], and $a_o = 0.5104$ nm reported by Green *et al.* [32]. Furthermore, there is no tetragonality [33] in the data, i.e., a systematic divergence of a_o values calculated from different lattice planes caused by a difference in unit cell dimensions along *a* and *c* lattice directions characteristic of tetragonal, not cubic, zirconia.

The relative intensities of cubic zirconia planes in a bulk powder standard are $I_{111} = 100$; $I_{220} = 50$; $I_{200} = 25$; $I_{311} = 20$ [29]. A comparison of these intensities with data in Fig. 1 shows that cubic zirconia has a strong ⟨100⟩ texture in the nanolaminates.

The average size of (200) cubic zirconia crystallites along the growth direction is 20 nm in films B and C, about the same size as zirconia layer thickness (22 nm) in film B and less than zirconia layer thickness in film

TABLE II Cubic zirconia crystallographic data for zirconia–titania nanolaminates grown on fused silica

Designation	hkl	Film	2θ (deg)[a]	d (nm)	a_o (nm)
1.	111[b]				
2.	200	A	35.30	0.254	0.509
		B	35.20	0.255	0.510
		C	35.10	0.256	0.512
3.	220	A	50.50	0.181	0.512
		B	50.65	0.180	0.510
		C	50.40	0.181	0.512
4.	311[b]				
5.	400	A[c]			
		B	74.42	0.127	0.510
		C	74.58	0.127	0.510

[a] $\pm 0.05°$.

[b] High resolution scan was not taken.

[c] Intensity of high resolution scan was too low for meaningful quantification.
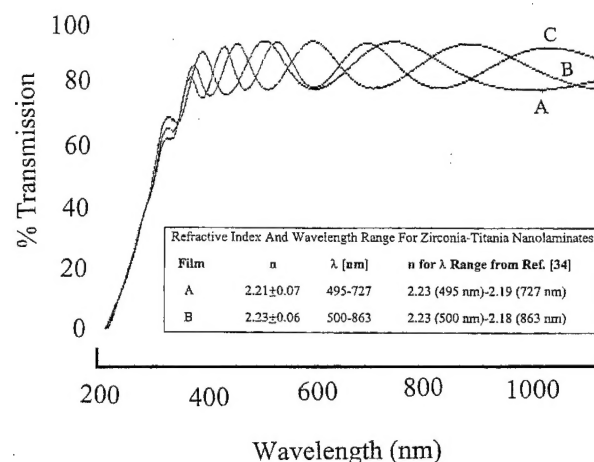

Wavelength (nm)

Figure 2 Optical transmission as a function of wavelength in zirconia–titania nanolaminates on fused silica. Insert tabulates the refractive index of films A and B.

C (32 nm). These data, combined with XRD evidence of other zirconia polymorphs in film C, show that either renucleation events occur with increasing zirconia layer thickness resulting in the formation of undesirable tetragonal zirconia, and/or there is a transformation from cubic to monoclinic zirconia with increasing crystallite size. Either process quenches cubic zirconia growth.

Fig. 2 shows that the films are optically transparent throughout the visible spectrum. The refractive index of single-phase cubic zirconia films A and B and the range over which the measurements were made are recorded in the insert in Fig. 2. For comparison, data from a definitive study by Wood *et al.* [34] of the refractive index of a series of yttria-stabilized cubic zirconias over a wide wavelength range was extrapolated to 0 mol% yttria and included in this insert.

In summary, we have demonstrated that high refractive index, undoped cubic zirconia films with a ⟨100⟩ crystallographic texture can be fabricated using vitreous titania growth interruption layers in a nanolaminate structure.

Acknowledgments

References

1. R. C. BILL, J. SOVEY and G. P. ALLEN, *Thin Solid Films* **84** (1981) 95.
2. J. R. BRANDON and R. TAYLOR, *Surf. Coating Technol.* **46** (1991) 91.
3. A. H. BARTLETT and R. D. MASCHIO, *J. Am. Ceram. Soc.* **78** (1995) 1018.
4. R. TAYLOR, J. R. BRANDON and P. MORRELL, *Surf. Coating Technol.* **50** (1992) 141.
5. R. E. BENNER and A. S. NAGELBERG, *Thin Solid Films* **84** (1981) 89.
6. R. P. READE, X. L. MAO and R. E. RUSSO, *Appl. Phys. Lett.* **59** (1991) 739.
7. H. SCHMIDT, K. HRADIL, W. HOSLER and W. WERSING, *ibid.* **59** (1991) 222.
8. J. H. KROSE, A. J. DREHMAN and J. A. HORRIGAN, *J. Mater. Res.* **10** (1995) 1086.
9. H. NAITO and H. ARASHI, *Solid State Ionics* **67** (1994) 197.
10. M. T. COLOMER, L. S. M. TRAQUEIA, J. R. JURADO and F. M. B. MARQUES, *Mater. Res. Bull.* **30** (1995) 515.
11. P. YASHAR, S. A. BARNETT, L. HULTMAN and W. D. SPROUL, *J. Mater. Res.*, in review.
12. S. C. MOULZOLF, R. J. LAD and R. J. BLAU, *Thin Solid Films*, in press.
13. P. J. MARTIN, R. P. NETTERFIELD and W. G. SAINTY, *J. Appl. Phys.* **55** (1984) 235.
14. D. J. GREEN, R. H. J. HANNINK and M. V. SWAIN, "Transformation toughening of ceramics" (CRC, Boca Raton, FL, 1989) p. 17.
15. R. RUH, K. S. MAZDIYASNI, P. G. VALENTINE and H. O. BIELSTEIN, *J. Am. Ceram. Soc.* **87** (1984) C190.
16. C. PASCAUL and P. DURAN, *ibid.* **66** (1983) 23.
17. H. G. SCOTT, *J. Mater. Sci.* **10** (1975) 1527.
18. S. C. MOULZOLF, Y. YU, D. J. FRANKEL and R. J. LAD, *J. Vac. Sci. Technol.* **A15** (1997) 1211.
19. R. J. LAD, Personal communication.
20. C. R. AITA, *Surface Engineering* **14** (1998) 421.
21. W. G. LEE, S. I. WOO, J. C. KIM, S. H. CHOI and K. H. OH, *Thin Solid Films* **237** (1994) 105.
22. L. S. HSU, R. RUJKORAKARN, J. R. SITES and C. U. SHE, *J. Appl. Phys.* **59** (1986) 3475.
23. W. D. KINGERY, H. K. BOWEN and D. R. UHLMANN, "Introduction to ceramics" (Wiley-Interscience, New York, NY, 1976) p. 714 and 727.
24. E. BAUER, in "Single crystal films", edited by M. H. Francombe and H. Sato (Macmillan, NY, 1963) p. 43.
25. L. AZAROFF, "Elements of X-Ray crystallography" (McGraw-Hill, New York, NY, 1968) p. 551.
26. A. H. CLARK, in "Polycrystalline and amorphous thin films and devices", edited by L. L. Kazmerski (Academic, New York, NY, 1980) p. 138.
27. J. D. DELOACH and C. R. AITA, *J. Vac. Sci. Technol.* **A16** (1998) 1963.
28. J. D. DELOACH, G. SCAREL and C. R. AITA, *J. Appl. Phys.* **85** (1999) 237.
29. ASTM Joint Committee on Powder Diffraction Standards, 1987, File No. 27-997.
30. ASTM Joint Committee on Powder Diffraction Standards, 1974, File No. 13-307.
31. *Ibid.*, File No. 17-923.
32. D. J. GREEN, R. H. J. HANNINK and M. V. SWAIN, *op. cit.*, p. 221.
33. Y. ZHOU and T.-C. LEI, *J. Am. Ceram. Soc.* **74** (1991) 633.
34. D. L. WOOD, K. NASSAU and T. Y. KOMETANI, *Appl. Opt.* **29** (1990) 2485.